UCLA
UCLA Electronic Theses and Dissertations

Title

Quantification of Systolic and Diastolic Left Ventricular Twist Using Fourier Analysis of STimulated Echoes (FAST) Magnetic Resonance Imaging

Permalink

https://escholarship.org/uc/item/9sh183z4

Author

Reyhan, Meral Leigh

Publication Date

2012

Peer reviewed|Thesis/dissertation

eScholarship.org Powered by the California Digital Library
University of California

UNIVERSITY OF CALIFORNIA

Los Angeles

Quantification of Systolic and Diastolic Left Ventricular Twist Using Fourier Analysis of STimulated Echoes (FAST) Magnetic Resonance Imaging

A dissertation submitted in partial satisfaction of the requirements for the degree Doctor of Philosophy in Biomedical Physics

by

Meral Leigh Reyhan

2012

© Copyright by

Meral Leigh Reyhan

2012

ABSTRACT OF THE DISSERTATION

Quantification of Systolic and Diastolic

Left Ventricular Twist Using

Fourier Analysis of STimulated Echoes (FAST)

Magnetic Resonance Imaging

by

Meral Leigh Reyhan

Doctor of Philosophy in Biomedical Physics

University of California, Los Angeles, 2012

Professor Daniel B. Ennis, Chair

In this dissertation a novel method for rapid quantification of left ventricular (LV) twist was developed, validated, and clinically evaluated. LV twist is defined as the difference in rotation of the apex relative to the base of the heart. Alteration in LV twist has been shown the correlate with LV dysfunction. Rotation was measured using Fourier Analysis of STimulated echoes (FAST), an image acquisition and rapid processing method. FAST can be applied to cardiovascular magnetic resonance (CMR) images with myocardial tagging, which imparts a sinusoidal pattern on the myocardial tissue that deforms with the LV during contraction and relaxation. First, FAST estimates of LV twist were validated using intra- and inter-observer comparison, intra- and inter-scan comparison, and comparison to values derived from a 'gold-standard' technique. Second, FAST was used in conjunction with a CMR imaging technique designed to lengthen the duration of myocardial tag detection to acquire diastolic twist information. Third, FAST was applied to an imaging technique developed to minimize chemical shift induced myocardial tagging pattern artifacts, which produces more accurate measurements

of LV twist. Fourth, FAST was used in combination with two free-breathing techniques to determine the impact of free-breathing on FAST estimates of LV twist. Fifth, FAST was used to characterize differences in LV twist in patients with moderate and severe mitral regurgitation. LV twist measurements derived from FAST showed good agreement for the intra- and inter-observer study and the intra- and inter-scan study. Additionally, systolic LV twist values matched well with the 'gold-standard'. When used in combination with the improved myocardial tag duration, FAST estimates of diastolic LV twist matched well with literature values. LV twist derived from the normal imaging technique compared with the artifact minimizing technique did not detect any significant differences, however this study was performed in healthy subjects, specific patient populations may provide different results. The free-breathing study detected a significant decrease peak LV twist due to free-breathing compared with breath-held imaging derived values. A significant decrease in peak LV twist was detected in patients with moderate and severe mitral regurgitation. Overall, the FAST method for quantitative LV twist measurement has been validated and shown to produce accurate measurements of twist with limited user interaction.

The dissertation of Meral Leigh Reyhan is approved.

Danny Jiong Jiong Wang

Matthew S. Brown

Peng Hu

Stefan Ruehm

Daniel B. Ennis, Committee Chair

University of California, Los Angeles

2012

DEDICATION

This dissertation is dedicated to my family Joyce, Mehmet, Erin, Lenora, Richard, Elise, Eric, Tomasz, Maria, Marek, Przemek, Şakir, Gülten, Gülşen, Okan, and Cassie for their support through my graduate studies.

TABLE OF CONTENTS

Acknowledgements…… vii

Vita…… viii

Chapter 1: Introduction to Cardiovascular Magnetic Resonance Imaging…….. 1

Chapter 2: Introduction to Left Ventricular Anatomy and Physiology…….. 18

Chapter 3: Fourier Analysis of STimulated Echoes (FAST) for the Quantitative Analysis of Left Ventricular Twist…….. 29

Chapter 4: Quantitative Assessment of Systolic and Diastolic Left Ventricular Twist Using Fourier Analysis of STimulated Echoes (FAST) and CSPAMM…….. 47

Chapter 5: Off-Resonance Insensitive Complementary SPAtial Modulation of Magnetization (ORI-CSPAMM) for Quantification of Left Ventricular Twist…….. 60

Chapter 6: Intra- and Inter-scan Reproducibility using Fourier Analysis of STimulated Echoes (FAST) for the Rapid and Robust Quantification of Left Ventricular Twist…….. 77

Chapter 7: Quantification of Left Ventricular Twist during Free-breathing with SPatial Modulation of Magnetization (SPAMM) and Fourier Analysis of STimulated Echoes (FAST)…… 90

Chapter 8: Left Ventricular Twist and Shear-Angle in Patients with Mitral Regurgitation……. 105

Chapter 9: Conclusion…….. 123

References…… 131

ACKNOWLEDGEMENTS

This dissertation was funded in part by the American Heart Association Western States Affiliate Predoctoral Fellowship, the NIH, the Department of Radiological Sciences, and the University of California Dissertation Year Fellowship.

VITA

2005 BS Physics and Mathematics, Rensselaer Polytechnic Institute, Troy, NY

2007 MS Physics, Rutgers University, Piscataway, NJ

2010 MS Biomedical Physics, University of California, Los Angeles, CA

PRESENTATIONS AND PUBLICATIONS

Reyhan M, Derbyshire JA, Ennis DB. Strain measurements with displacement encoded stimulated echoes are insensitive to off-resonance. ISMRM Conf. Proc. Honolulu, Hawaii, USA, 2009.

Reyhan M, Natsuaki, Y, Ennis DB. Fourier Analysis of STimulated echoes (FAST) for quantitative analysis of left ventricular torsion. SCMR Conf. Proc. Phoenix, Arizona, USA, 2010.

Reyhan M, Natsuaki, Y, Ennis DB. Fourier Analysis of STimulated echoes (FAST) for quantitative analysis of left ventricular torsion. ISMRM Conf. Proc. Stockholm, Sweden, 2010.

Reyhan M, Ennis DB. Quantification of Left Ventricular Torsion by Off-Resonance Insensitive CSPAMM (ORI-CSPAMM). ISMRM Conf. Proc. Montreal, Canada, 2011.

Reyhan M. Ennis DB. Quantitative Assessment of Systolic and Diastolic Left Ventricular Twisting Using Fourier Analysis of STimulated Echoes (FAST) and CSPAMM. SCMR Conf. Proc. Orlando, Florida, USA 2012.

Reyhan, M, Natsuaki Y, and Ennis DB. “Fourier Analysis of Stimulated Echoes”. Journal of Magnetic Resonance Imaging. 2011 Nov 8. Doi: 10.1002/jmri.22863.

Reyhan, M, Ennis DB. “Quantitative assessment of systolic and diastolic left ventricular twist using Fourier Analysis of STimulated echoes (FAST) and CSPAMM”. Journal of Magnetic Resonance Imaging. Accepted.

CHAPTER 1

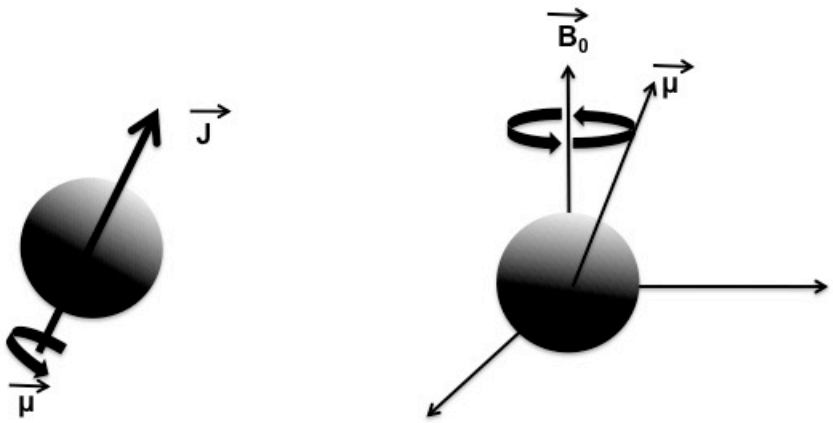
Introduction to Cardiovascular Magnetic Resonance Imaging

Nuclear Magnetic Resonance

The body is composed of about 70 percent of water, which contains hydrogen. A hydrogen atom can be described as an electron (negatively charged particle) encircling a nucleus, which also rotates, composed of one proton (positively charged particle). The rotation of the nucleus is known as angular momentum. The rotation of a positively charged particle induces a magnetic field, known as nuclear magnetism. This field is represented by a nuclear magnetic dipole moment. Angular momentum, **μ**, is related to magnetic moment, **J**, by the following equation(1):

$$\vec{\mu} = \gamma \vec{J} \qquad [1]$$

where γ is known as the gyromagnetic ratio, Figure 1A.



A. B.

Figure 1. A. Illustration of a magnetic dipole. B. Depiction of magnetic dipole in an external field, B_0.

In MRI gyromagnetic ratio for hydrogen is measured as(1, 2):

$$\frac{\gamma}{2\pi} = 42.58 MHz/T \qquad [2]$$

The magnetic resonance imaging (MRI) signal is generated from an ensemble of nuclei. These spins are normally oriented randomly, but when in the presences of an external magnetic field (B_0), the spins align parallel or anti-parallel with the field. The different orientations of the spins are associated with different energy states, the difference between the energy levels is known as Zeeman splitting and is characterized by the Boltzmann relationship.

When placed in an external magnetic field, the magnetic dipoles experience a torque, Figure 1B, which causes them to precess about the main axis of the external magnetic field. The angular frequency of the precession can be described by(1-3):

$$\omega_0 = \gamma B_0 \qquad [3]$$

This frequency is called the Larmor frequency and it describes a clock-wise rotation about the magnetic field. An ensemble of spins that have the same resonance frequency is called an isochromat. Shielding of the nucleus due to the electrons of the different chemical compositions of tissue in the body and inhomogeneities in the main field can lead to different resonance frequencies, and thus different isochromats(3).

RF Excitation

Often the observable bulk magnetization from an ensemble of spins is described as a vector, **M**, which will initially point along the direction of the main magnetic field $\mathbf{B_0}$, longitudinally, assuming no external forces. In order to obtain a signal from the bulk magnetization, the magnetization must be tipped down into the transverse plane. The external forces that tip the magnetization come from oscillating magnetic fields, denoted as

$\mathbf{B_1}$(t). These fields are short lived and much weaker than the main static magnetic field $\mathbf{B_0}$. The rotating $\mathbf{B_1}$ field propagates in the transverse plane and is generated by an RF pulse. RF coil is located between the plastic outer shell of the MRI system and the gradient coils(2).

Additionally, in order to exact an effect on the bulk magnetization, the B_1 carrier frequency of the rotation must match the Larmor frequency. The behavior of the bulk magnetization, **M**, in the presences of the $\mathbf{B_0}$ and $\mathbf{B_1}$ fields is defined by the Bloch equation(2):

$$\frac{d\vec{M}}{dt} = \gamma\vec{M} \times \vec{B} - \frac{M_x\hat{i} + M_y\hat{j}}{T_2} - \frac{(M_z - M_z^0)\hat{k}}{T_1} \qquad [4]$$

where M^0_Z is the thermal equilibrium value for **M**, T_1 is the spin-lattice time constant of relaxation of the bulk magnetization after it is disturbed from equilibrium, and T_2 is the spin-spin relaxation time constant of the bulk magnetization after it is disturbed from equilibrium. After the bulk magnetization is perturbed from thermal equilibrium, it attempts return to its initial state and orientation by longitudinal recovery and transverse decay. Since RF pulses are short in duration compared to T_1 and T_2, for the case of RF excitation the Bloch equation can be simplified to(2):

$$\frac{d\vec{M}}{dt} = \gamma\vec{M} \times \vec{B} \qquad [5]$$

At this point it is helpful to introduce a rotating frame of reference, which is a rotating coordinate system, in which the transverse plane rotates with angular frequency ω. In this frame of reference precession about B_1 is more clear and the equation 5 can be rewritten as(2):

$$\frac{\partial\vec{M}_{rot}}{\partial t} = \gamma\vec{M}_{rot} \times \vec{B}_{eff} \qquad [6]$$

such that

$$\vec{B}_{eff} = \vec{B}_{rot} + \vec{\omega}/\gamma$$

where the subscript 'rot' denotes the value as seen in the rotating frame and the B_{eff} denotes the effective field the nuclear spins see in the rotating frame. The effective B-field can be written as(2):

$$\vec{B}_{eff} = \vec{B}_1(t)\hat{i} \qquad [7]$$

A solution to the Bloch equation after the application of an RF pulse, assuming the initial bulk magnetization exists only in the longitudinal plane and is equal to M^0_z, results in precession of the bulk magnetization about the x-axis in the rotating frame of reference. This precession is called a forced precession and effectively tips the bulk magnetization away from the z-axis and into the transverse plane, where signal can be detected, Figure 2.

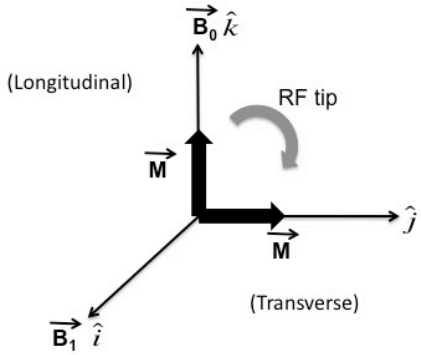


Figure 2. Illustration of RF tipping the bulk magnetization into the transverse plane, in the rotating frame.

The flip angle, α, is defined as the angle between the bulk magnetization and the z-axis. For a rectangular RF pulse, alpha is defined as:

$$\alpha = \gamma B_1 t \qquad [8]$$

where B_1 is the amplitude of the RF pulse and t is the duration of the RF pulse. The phase of an RF pulse, φ, define is defined within the transverse plane and defines the axis of rotation.

Gradient Fields and Spatial Localization

Linear magnetic field gradients are an important part of MR imaging. These gradient fields vary linearly along a specific direction and are key to spatial encoding of the MR signal. There are three separate gradient coils located within the main magnetic field. These gradients produce loud acoustic noise due to vibrations produced in the coil assembly by Lorenz interaction between the main magnetic field and the current within the gradient.

The exact center of the main magnetic field is called isocenter and corresponds to the position (0,0,0). The z-direction (**k**) follows the length of the bore, the y-direction is the vertical direction with respect to the bore, and the x-direction is the horizontal direction with respect to the bore, Figure 4.

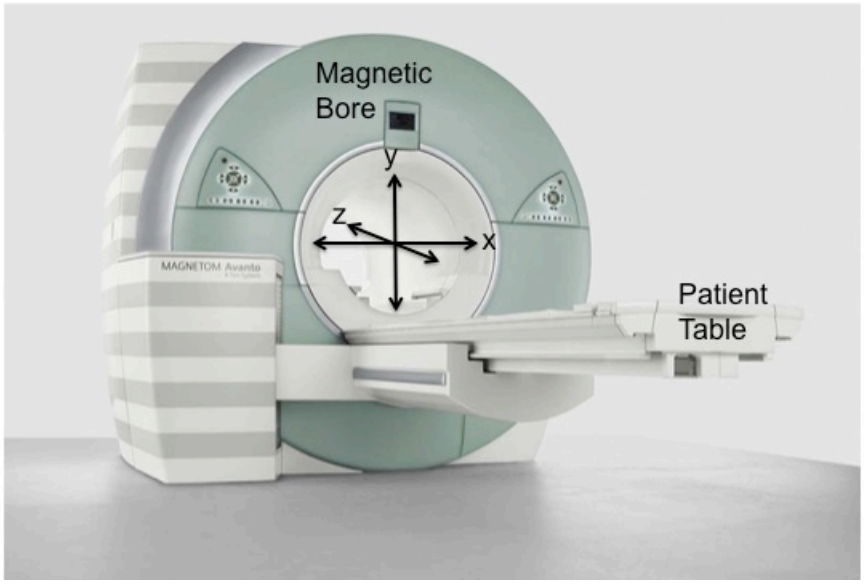


Figure 4. Illustration of the magnetic bore and different gradient directions.

The gradient field can be expressed as:

$$\vec{G} = \frac{\partial B_z}{\partial x}\hat{i} + \frac{\partial B_z}{\partial y}\hat{j} + \frac{\partial B_z}{\partial z}\hat{k} \qquad [9]$$

where B_z is the z component of main magnetic field. An applied gradient [G/cm] increases/decreases the magnetic field strength imparted on a spin, and this in turn increases/decreases its precessional frequency. The changes in precessional frequency change the phase of the spins and allow spins to be identified by their location with respect to the gradient, in this way the spins are spatially encoded(2).

The maximum time rate of change associated with the gradient field is called the slew rate [G/cm s]. The typical gradient shape with respect to time is design as a trapezoid. The gradient amplitude starts at 0 T/m and slews up to a peak gradient amplitude and then slews back down to 0 T/m. The time it takes to reach the maximum gradient amplitude is called the ramp up time and the time to return to 0 m/T is called the ramp down time(3).

Frequency Encoding Gradients

A two dimensional image is often formed by collecting different rows of pixel information. In the case of MRI, these rows of information are collected in a subspace of Fourier space, called k-space. After the rows of information are collected and the image data subjected to an inverse Fourier transformation, anatomical images are formed.

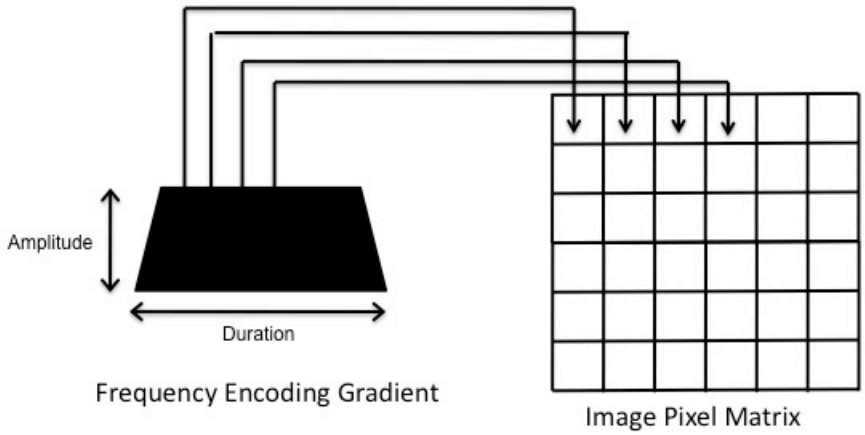


Figure 5. Depiction of frequency encoding gradient reading out single lines of k-space image data.

Frequency encoding gradients are often used to readout single lines of MR signal on a pixel by pixel basis in k-space, often thought of as different spatial frequencies, Figure 5. SIn the case of typical Cartesian Fourier encoded imaging, the direction of the frequency encoding gradient is fixed and the gradient is repeated while a phase encoding gradient is incremented. The actual waveform of the gradient usually includes a prephasing gradient lobe and a readout gradient lobe. The prephasing lobe is played before the readout lobe and is used to prepare the transverse magnetization to generate an echo signal. The readout lobe is used to impart a spatially varied precessional change to the spins across the object with a linear relationship to the position of the spin(3).

Phase Encoding Gradients

The phase encoding gradient is used to spatially encode the spins in the direction perpendicular to the frequency encoding direction in k-space. It spatially encodes the spins for collection of different rows of data for the k-space image, often thought of as different spatial frequency data, Figure 6. For traditional Cartesian encoding, the phase encoding gradient is played temporally before the frequency encoding gradient. The amplitude of the

phase encoding gradient is then decreased or increased to select different rows. The change of area under the phase encoding gradient lobe imparts different amounts of linear phase to the spins(3).

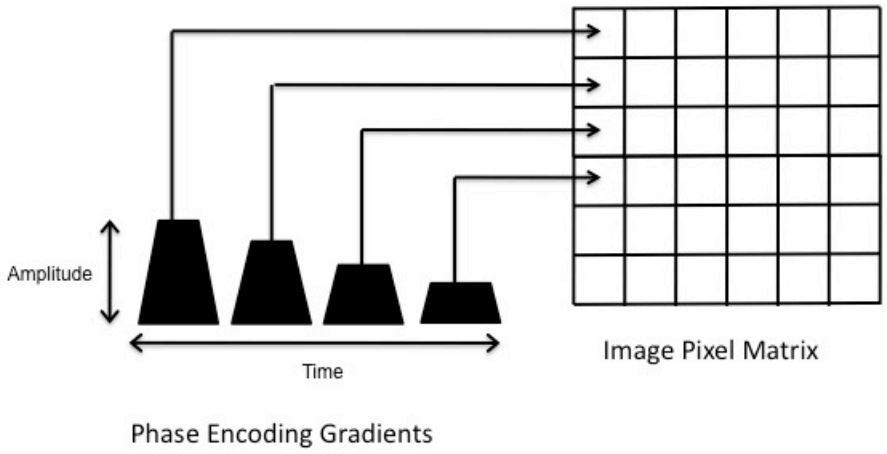


Figure 6. Depiction of phase encoding gradients spatially encoding image data in k-space.

Slice Selection Gradients

To select a slice of tissue for imaging within the body, both a spatially selective RF pulse and a slice-selection gradient are needed. The RF pulse is commonly a windowed sinc shaped pulse, which is used to spatially excite a band of frequencies within the body. The Fourier transform of a sinc function is a box-function, which will create the desired profile for the slice. The RF pulse and the slice selection gradient are played at the same time. Typically a constant gradient is used for slice selection and often has a slice-rephasing lobe. The gradient linearly relates the band of frequencies excited by the RF pulse to position. Additionally, the gradient creates a linear phase shift across the slice thickness, which can lead to signal loss. To correct for the phase shift a rephasing lobe of the gradient can be applied(3).

MR Signal and Signal Detection

MR signal detection is based on Faraday's law of induction, which states that an induced electromotive force in a closed circuit is equal to the negative of the temporal rate of change of the magnetic flux through the circuit. In the case of MRI, the circuit is a receiver coil, often the same coil used to transmit the RF pulse, and the induced electromotive force is a voltage signal that is used to produce the MR images. The voltage signal is a high frequency signal that can create problems in electronic circuits. For this reason the signal is demodulated and moved to a low frequency band(3).

After RF pulse excitation an MR signal can be generated in three main ways: free induction decays, RF echoes, and gradient echoes. A free-induction decay (FID) occurs after a single RF pulse is played on a spin system. The 'free' precession of the bulk magnetization vector generates the FID signal after the application of the RF pulse. The FID signal decays with time due to transverse relaxation and main field inhomogeneities. This decay is an effect of spin dephasing, which causes a loss of phase coherence in the bulk magnetization(2).

RF echoes are generated by playing multiple RF pulses, with a minimum of two RF pulses needed to produce an RF echo. The classic example of an RF echo is derived from the application of a 90° RF pulse followed by a 180° RF pulse, Figure 7. After the application of the 90° RF pulse an FID is formed, with time this FID decays as a result of the loss of phase coherence of the bulk magnetization. Next, the 180° RF pulse is played on the dephased spins. This pulse flips the spins to the opposite side of the transverse plane and with time the dephased spins rephase and the bulk magnetization regains its phase coherence. As the spins start to resynchronize their phases, an RF echo begins to form. The peak of the echo occurs when the spins have maximum phase coherence. After this point, the decay processes begins again. This example with two RF pulses can be expanded to multiple RF pulses, which interact to form echo trains(2).

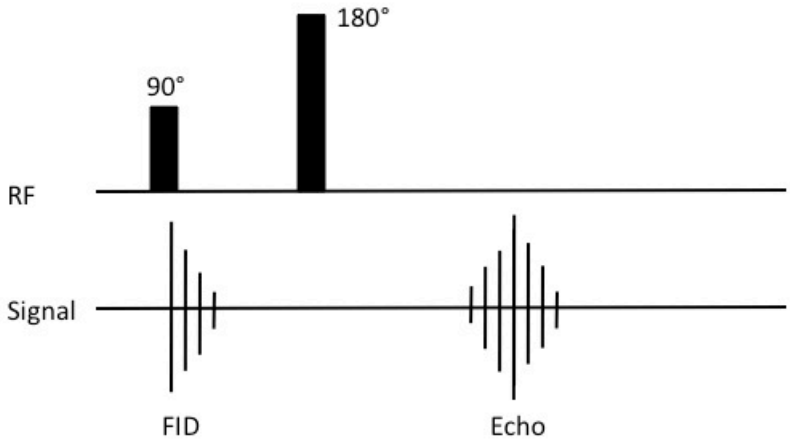


Figure 7. Depiction of FID and echo formed by 90° and 180° RF pulses.

Gradient echoes are often generated by the application of a RF pulse with a small flip angle followed by two gradients. The RF pulse is used to transfer the bulk magnetization into the transverse plane. When the gradient is played the spins acquire different phases, which leads to a loss of spin phase coherence with time. If another gradient of equal and opposite amplitude is played, the spins will slowly rephase, resulting in a gradient echo. The peak of the echo will correspond to twice the area of a gradient, where area is equal to the time integral of the gradient. This example can also be extended to form gradient echo trains(2).

Gradient Readout Echo Imaging

There are many ways to form images using MRI; one of the most common practices is called Gradient Readout Echo (GRE) imaging. The sequence in which the RF and gradient pulses are played is known as a pulse sequence, Figure 8.

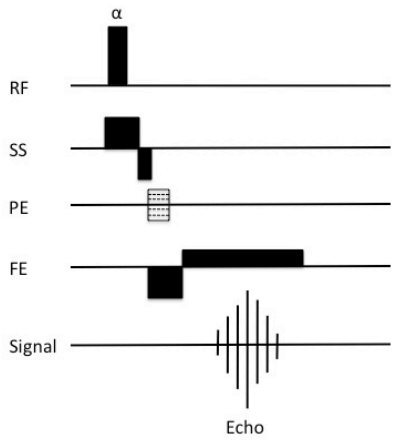


Figure 8. Pulse sequence diagram of gradient readout echo imaging depicting the slice select encoding gradient (SS), the phase encoding gradient (PE), and the frequency encoding gradient (FE).

To start, an RF alpha pulse is generated by the transmit coil and played concurrently with slice select gradient. This combination selects a slice of the body for imaging, as described above. Next, a phase encoding gradient creates a linear spatial variation in the phase of the magnetization. The overall effect is to encode spatial information orthogonal to the frequency encoding direction allowing the encoding of different lines of k-space. A frequency encoding gradient prephasing lobe is played with opposite polarity to the readout lobe of the gradient. The prephasing lobe prepares the transverse magnetization by making the magnetization accumulate phase, so that an echo signal can be created later. The polarity change between the prephaser and the readout reverses the direction of phase accumulation. The echo peak is formed when the area below the prephaser is equal to the area below the readout gradient lobe(2, 3).

The echo induces an electromotive force in the receive coil which is sampled by an analog to digital convert (ADC) at regular time intervals, Δt, which is also called the dwell time and is the inverse of the readout bandwidth. The signal undergoes further digital

filtering and is eventually stored on a computer. The duration of the readout lobe of the frequency encoding gradient corresponds to the number of samples collected by the ADC(3).

The amplitude of the phase encoding gradient is varied until all desired lines of k-space are acquired. At this point an image in k-space has been captured. The center of the k-space image corresponds to the maximum amplitude of the signal, while the outer edges of k-space correspond to lower amplitude signal; these edges correspond to i the fineness or clarity at sharp interfaces in the final anatomical image. Both portions of k-space must be collected to create a diagnostic quality image. After an inverse Fourier transformation, the frequency image in k-space is transformed to an anatomical image.

A three-dimensional image is composed of voxels, which are three-dimensional pixels. Each voxel has a bit-depth associated with it, which is an indicator of the available grayscale steps displayed as color on a monitor. In MRI, the depth of the voxel is associated with the thickness of the imaged slice. The number of voxels in an image is associated with the number of rows in the y direction of the image (generally dependent on the phase-encoding gradient parameters) and the number of columns in the x-direction (generally dependent on the frequency-encoding gradient parameters). The size of the image is called the field of view, FOV, and corresponds to the inverse of the distance in k-space between the image space voxels. The signal to noise ratio (SNR) of the image is often described by the following equation and describes the quality of the image(2):

$$SNR \propto \left(\frac{FOV_x}{N_x} \cdot \frac{FOV_y}{N_y} \cdot \Delta z \right) \cdot \sqrt{\frac{N_x \cdot N_y \cdot N_{Avg}}{BW}} \qquad [10]$$

where FOV indicates the field of view in different directions, N_x and N_y represent the number of frequency and phase encoding steps, Δz is the slice thickness, N_{Avg} is the average number of times imaging has been performed, and BW is the receive bandwidth.

Chemical Shift

Often imaging artifacts are visible in MRI images, among the most common is chemical shift. Chemical shift refers to the Larmor frequency difference between chemical materials in the body. Atomic nuclei are surrounded by electrons, which shield the nucleus from the main magnetic field, reducing its effects on the nucleus. The amount of spatial displacement due to chemical shift is easily calculable. For the case of fat, the Larmor frequency is shift lower than water by 3.5 parts per million. For example for a 1.5T MR scanner, the frequency shift, $\Delta\omega_c$, between water and fat is given by(2):

$$\Delta\omega_c = 2.675 \times 10^8 rad/s/T \times 3.5 \times 10^{-6} \times 1.5T = 1.4 \times 10^3 rad/s$$

or in more familiar units

$$\Delta f_c = \frac{1.4 \times 10^3}{2\pi} = 222Hz.$$

The bandwidth of a gradient corresponds to a measure of the range of frequencies across the field of view of the image. Typically during the readout processes the bandwidth of the frequency encoding gradient, the gradient in the direction chemical shift occurs, is specified in units of Hz/pixel. For a typical frequency encoding gradient bandwidth of 250Hz/px, the displacement caused by chemical shift would be ~0.9 pixels in the anatomical image.

Cardiac Triggering

MRI is a slow imaging modality. This means imaging the motion of the heart requires different techniques to ensure good temporal resolution. Often the cardiac cycle is broken into phases with equal temporal spacing. Electrocardiography, ECG, interprets the electrical activity of the heart over a period of time. The prominent waves of an ECG are called the QRS complex. The R- wave in particular represents when the ventricles of the heart depolarize and is typically the tallest peak on the waveform. Detection of the R-wave is

used to synchronize MRI image collection with the cardiac cycle ; this process is called cardiac triggering(4).

Segmentation

In the case of prospective triggering several heartbeats are divided up into different segments for imaging, each segment is used to acquire 1/Nth of the image data in a single heartbeat, where N is the total number of heart beats needed to make a movie of a 'single' heartbeat. Each temporal frame in the movie is called a phase and corresponds to a certain percent of the cardiac cycle. During each segment, specific lines of k-spaces are acquired corresponding to the different phases of the cardiac cycle are acquired. As the number of imaged segments increases, more lines of k-space are collected helping complete the total image acquisition for each phase. After N heart beats enough information has been collected to complete each temporal frame, cardiac phase, and form the movie, Figure 9. The data is combined such that each image is composed of multiple lines collected during each segment. In this way each separate image corresponds to a different temporal component of the cardiac cycle. Temporal resolution is defined by the repetition time of the pulse sequence times the number of k_y lines collected per segment (3, 4).

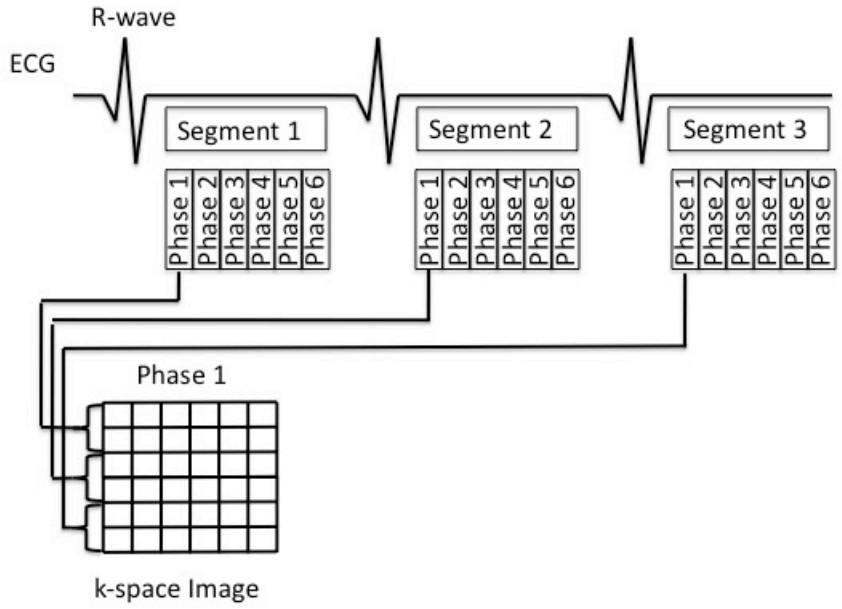


Figure 9. Depiction of the segmentation process and image formation.

Respiratory Triggering

Respiratory motion in images caused by breathing is often an unwanted artifact found in MR images. A common respiratory triggering technique is called navigator triggering. A navigator RF pulse is used to excite a ~2 cm column of spins in the superior-inferior direction through the diaphragm. The position of the diaphragm is quantified with this pulse and used to determine respiratory phase. Image acquisition is performed during the same respiratory phase over multiple respiratory cycles, thus providing a consistent heart position and allowing free-breathing during the scan(3).

The respiratory bellows is another device often used for respiratory triggering. The bellows are a tube filled with air and placed over the chest and abdomen. The change in pressure of the air in the bellows corresponds to inspiration and expiration and is converted into a respiratory waveform used for image acquisition triggering. The bellows allow image

acquisition during a specific time point of the respiratory cycle helping minimize motion artifacts in images from free breathing(3).

SPAMM Tagging

Magnetization preparation pulses are often triggered immediately after each R-wave prior to the imaging portion of the pulse sequence. One common type of preparation pulse is RF tagging. This type of prep pulse is characterized by spatial labeling of an image with a repeating stripe pattern. SPAtial Modulation of Magnetization (SPAMM) (5) tagging is generated by a sequence of at least two RF pulses with gradients played between the pulses and a spoiling gradient played at the end of the preparation. For example the combination of playing a 90° RF pulse, followed by a gradient, followed by another 90° RF pulse, followed by a spoiling gradient will create a stripped tagging pattern, Figure 10.

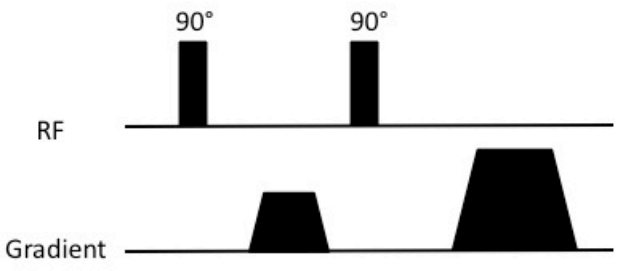


Figure 10. Pulse sequence diagram of the preparation pulse for Spatial Modulation of Magnetization (SPAMM).

The first RF pulse tips the bulk magnetization into the transverse plane. Next, the gradient produces the desired spatial pattern by dephasing the bulk magnetization vector. The second RF pulse rotates the dephased spins into the longitudinal plane. The spoiling gradient crushes the remaining transverse components of these spins. This has the effect of storing the spatially encoded spins along the longitudinal axis and preventing further dephasing due to transverse relaxation before imaging. The imaging RF pulse tips the spins

back into the transverse plane, where the stored stripe pattern is imaged. In k-space this pattern is distinguished as a stimulated echo and stimulated anti-echo, which are visible as two peaks on either side of the low spatial-frequency information in the center of the k-space image.

Complimentary spatial modulation of magnetization(6) (CSPAMM) is an alternate tagging pulse sequence, which improves tag contrast late in the cardiac cycle thereby enabling the quantitative evaluation of both systolic and diastolic function. Contrast is improved with CSPAMM due to the separation of the component of magnetization with the tagging information from the relaxed component, which is facilitated by subtraction of two measurements, made with phase shifted tagging patterns(6).

Additionally, using a variable flip angle technique in conjunction with CSPAMM can enhance contrast. This technique involves varying the imaging flip angle with the following recursive formula(7):

$$\alpha_{k-1} = a\tan(\sin(\alpha_k)\cdot e^{-\Delta t/T_1}) \qquad [11]$$

where α represents the flip angle, k represents the phase, Δt indicates the duration of time between the RF imaging pulses, and T_1 indicates the relaxation time of myocardium (~850 ms at 1.5T). It has been shown that for short repetition times, a_k =21° produces the best contrast (7).

In this dissertation gradient echo imaging techniques are combined with either SPAMM or CSPAMM tagging to evaluate left ventricular function under a range of experimental conditions.

CHAPTER 2

Introduction to Left Ventricular Anatomy and Physiology

The heart is composed of four chambers, the left ventricle is the chamber which pumps blood out of the heart and into the aorta and then to the rest of the body. Normal left ventricular function is based on coordinated electrical activation and mechanical contractions. The myofiber geometry of the left ventricle is helical in nature, gradually changing from a right-handed helix in the sub-endocardium to a left-handed helix in the sub-epicardium. The electromechanical performance of the heart depends largely on the structural properties of the myocardium. Understanding normal left ventricular structure, electrical activation, and motion sequences are important for bettering diagnostic cardiovascular measurements and may ultimately help to evaluate new therapies for treating heart disease (8). Current research is particularly interested in the left ventricle and its anatomical arrangement of myofibers in the adult heart, the sequence of depolarization and repolarization, the mechanics of isovolumic contraction, ejection, isovolumic relaxation, postsystolic shortening and twist, as well as, the relationship of prolonged strenuous exercise to left ventricular function.

The normal left ventricle has an ellipsoidal shape. It is thicker than the right ventricle because it pumps blood at a higher pressure. The long-axis of the left ventricle is directed from the apex to base of the heart. The geometry of the short axis is approximately circular. However, non-uniformities exist in the thickness of the left ventricular wall. The posterolateral wall is thicker than the septal wall and a gradual thinning of the walls is observed in apical segments (8).

Development of the Left Ventricle

Many developmental changes occur from the primitive embryonic heart to the mature adult heart. At early stages of cardiac development the arrangement of myofibers is helical. The primitive embryonic heart develops from two layers of epithelial cells and a middle layer of cardiac jelly (extracellular matrix) (9). The inner layer grows toward the ventricular cavity as sheets and chords that develop into trabeculae, which are nourished from the blood flowing in the intertrabecular spaces. In humans this occurs at the end of the fourth week of gestation. The trabeculations in the luminal layers of the ventricles allow the myocardium to increase its mass in the absences of discrete coronary circulation. The cells in the outer layer undergo compaction, as a result of the functional needs of the growing embryo and are covered by epicardium. At approximately 8 weeks in humans, part of the trabecular layer becomes solid and increases the compact component of the ventricular myocardium. The early embryonic heart responds to mechanical changes; for example, increased pressure load is met by thickening and spiraling of the trabeculae (10).

An initial isotropic electrical activation sequence spreads from the caudal portion of the tubular heart toward the cranially located outflow (8). The wave of contraction drives the blood forward in a peristaltic manner. After a few days, flow becomes pulsatile as the lumen expands and the endocardial wall thickenings begin to function as primitive valves. Next, the cardiac tube develops external constrictions. After the initial contractions, cardiac looping begins. Looping consists of two components: bending and twisting. “The primitive heart bends outward from the body of the embryo and normally twists to the right (9).” Development of the torsional component of looping helps progress the change from propulsive movements of the tubular heart to the twisting motion of the adult heart. Continued maturation of the left ventricular wall occurs in conjunction with the development of the His-Purkinje conduction system, which alters the base to apex pattern of electromechanical activation into the mature one (8).

Myocardium

The myocardium is made up of millions of myocytes within a matrix of connective tissue. The myocyte itself is a long and thin cell; it connects to its neighboring cells by intercalated discs. The myocytes are supported by a continuous matrix of fibrous tissue, and wrapped in endomysium, which supports the intercalated discs in binding to adjacent myocytes and forming a 'weave' around them. Clusters of myocytes are surrounded by condensations of the endomysial weave which forms the perimysium, which collects the clusters into 'myofibers'. The perimysial partitions are anchored within the epimysium, which surrounds the ventricular mass and protects against superfluous stretch. The perimysial fibrous sheets inside the global fibrous matrix of the ventricular mass permit the collections of myocytes to slide alongside one another during systole and diastole (11).

The mechanical performance of the heart depends largely on the structural properties of the myocardium. Geometric models of the left ventricle generally use an ellipsoidal coordinate system. The left ventricle is depicted as having two helical fiber geometries; one in the subendocardium and the other in the subepicardium. The fiber geometries have a counter directional arrangement, which helps equally distribute stress and strain in the heart. Fiber orientation is quantified by both the helix fiber angle and the transverse fiber angle. The helix angle is described as the angle between the circumferential axis and the projection of the myofiber onto the longitudinal-circumferential plane (12). This angle changes continuously from the subepicardium to subendocardium from -50° to 47° respectively during end diastole, -60° to 48° during isovolumic contraction, and -66° to 65° during end systole (13). The transverse angle is defined as the angle between the circumferential axis and the projection of the myofiber orientation onto the radial-circumferential plane (12). This angle changes from -20° to 20° with no significant differences during end diastole, isovolumic contraction, or end systole (13).

Collagen binds neighboring myocytes and this forms layers called lamina or sheets. These sheets are typically four cells thick and separated by cleavage planes (8). The sheet also has an angle associated with it, the angle with respect to the circumferential radial plane. Sheet angles oriented toward the base from endocardium to epicardium are considered positive. The sheet angles transition from positive at the base to negative at the apex. Reorientation of the sheet toward the radial direction occurs during isovolumic contraction and end systole. Diffusion tensor magnetic resonance imaging was presented as a non-invasive way to measure sheet angle and compared to histological staining for sheet angle measurement in a study presented by Chen (13). However, one limitation of diffusion tensor magnetic resonance imaging noted was limited spatial resolution which made measured sheet angle an average of approximately twenty sheets (13). Additionally, it has been shown that two local myocardial sheet populations exist with mean sheet angles derived from diffusion tensor MRI of 36°± 24° and -55°± 28° (14).

Electrical Activity

The depolarization of the left ventricle, which contains the electrical gradients that produce the QRS complex on an ECG has been well studied. In 1969, a study was performed by Durrer to demonstrate the time course and instantaneous distribution of the excitatory process of the normal human heart. In this study cadaver hearts were harvested and perfused with a mixture of Na, K, Ca, Mg, CL, HCO_3, H_2PO_4, hemoglobin and glucose. Most of the harvested hearts began beating in a spontaneous sinus rhythm for a period of 4 to 6.5 hours. The electrical activity was recorded using approximately 660 epicardial or intramural electrodes. It was demonstrated that in the left ventricle, three endocardial areas were synchronously excited 0 to 5 ms after the start of the left ventricular cavity potential. The first area was high on the anterior paraseptal wall, within the tissue parallel to septal wall surface, just below the attachment of the mitral valve. The second area was central on

the left surface of the interventricular septum. The third area was in posterior paraseptal area at about one third the distance from apex to base. The areas increased rapidly in size for the next 5 to 10 ms and merged together between 15 to 20 ms after the start of excitation. By this point in time, the activation front covered most of the ventricular cavity except for a posterobasal area, a middle lateral area, and an apical anterior area. The movement around the cavity was shown to be more rapid than the spread toward the epicardium. After 30 ms the activation front is nearly completely closed and the excitation reached the epicardial surface over the site originally activated. The activation continued to move around the epicardial surface with the posterobasal area activated last (15).

The gradients underlying repolarization of the left ventricle, the T wave on an ECG, are not as well understood as those that cause depolarization of the ventricle. There are three types of inhomogeneities that seem to play a role in dispersion and configuration of the repolarization wave: the differences between the apex-base and anterior-posterior, transmural differences, and the differences between the right and left ventricle (16). It has been shown, in in-situ porcine hearts with implanted bipolar electrodes and sonomicrometry that the repolarization gradients travel in reverse compared to depolarization; that is the base repolarizes before the apex. Compared to the base, the subendocardial and subepicardial repolarization of the apex is delayed. The longest time for repolarization occurred for the left ventricular apical subepicardium, which is the last region to repolarize. This delay in repolarization suggests that there may be transmural heterogeneity in the repolarization process in different regions of the left ventricle (17). The transmural sequence of repolarization varies in different species. In mice, there exists a repolarization gradient between the subepicardium and subendocardium. However, in canines both areas repolarize at approximately the same time. Transmural differences in repolarization at the base of the left ventricle were not seen in beating canine or porcine hearts. Therefore, the

repolarization wave may be primarily due to the base to apex gradient with nominal contributions from the transmural gradient (17).

Cardiac Cycle

The cardiac cycle is composed of several phases. The first is atrial contraction, denoted by the p-wave on an ECG, which represents the depolarization of the atria, which causes the contraction. The second phase is isovolumic contraction (IVC), which begins with the QRS signal on the ECG. IVC represents the ventricular depolarization, which is denoted by myocyte contraction. Isovolumic contraction is the period that follows the closing of the mitral valve and is denoted by a rapid increase in left ventricular pressure before the opening of the aortic valve (18). The isovolumic phase is distinguished by transient changes in left ventricular shape that produce rapid variations in regional velocities (8). During isovolumic contraction shortening of the left ventricular subendocardial fibers (right-handed helical fibers), is accompanied by stretching of the nearly orthogonal subepicardial fibers (left-handed helical fibers). Subsequent to isovolumic contraction is the ejection phase, which represents the ejection of blood into the aorta and pulmonary artery from the respective ventricles. During this time, the atrial pressures begin to rise as a result of systemic circulation and the venous return from the lungs. Next, isovolumic relaxation occurs. In this case, the intraventricular pressure falls and the aortic and pulmonary valves close. After isovolumic relaxation, the filling phase begins. The onset of filling begins when the intraventricular pressures fall below the respective atrial pressures. This leads to the opening of the atrioventricular valves and the filling of the ventricles (19).

Strain

Measurements of strain quantify the shortening and thickening of the left ventricular wall. Normal strain is defined as, " the difference between an end systolic and an end diastolic

dimension divided by a reference end-diastolic dimension and are, as such, dimensionless and presented as a percent values. Two adjacent node points can be projected on a coordinate axis and the length of this projection can be measured. The length of this projection can change during the cardiac cycle and the difference of these lengths divided by the total length at end diastole defines the normal strains (20)." Shear strain utilizes the same definition with the exception of a difference of projected length and end-diastolic distance being defined on different axes. Strains are expressed in the local cardiac coordinate system and the local fiber system: radial, circumferential, and longitudinal and the radial axis, the fiber axis which is tangent to the surface and parallel to the local fiber orientation and the cross-fiber axis which is tangent to the surface and perpendicular to the fiber (20)". Normal human circumferential and longitudinal shortening (indicated by negative sign) strains have been shown to be greater at the apex in both the epicardium and endocardium when compared to the base (normal circumferential strain: -15.6 +/- 0.4, -42.9 +/-0.5 versus -13.2+/-0.3, -31.9+/-0.4; normal longitudinal strain: -17.6+/-0.3, -19.3+/-0.3 versus -16.9+/-0.3, -18.5+/-0.3) (20). This further demonstrates the mechanical shortening corresponding to apex to base electrical activation.

LV Twist

Left ventricular twist (sometimes referred to as torsion or rotation) is the mean longitudinal gradient of the net difference between the clockwise rotation of the apex and the counterclockwise rotation of the base (when viewed from the apex) in a short axis view, Figure 1. During isovolumic contraction, the left ventricular apex has a brief clockwise rotation that reverses and becomes counterclockwise during ejection. The counterclockwise twist during ejection at the apex is followed by a clockwise rotation during isovolumic relaxation and the beginning of diastole filling. The left ventricular base has a short counterclockwise rotation during isovolumic contraction, followed by a clockwise rotation

during ejection, and then a counterclockwise rotation during isovolumic relaxation and early diastole (21).

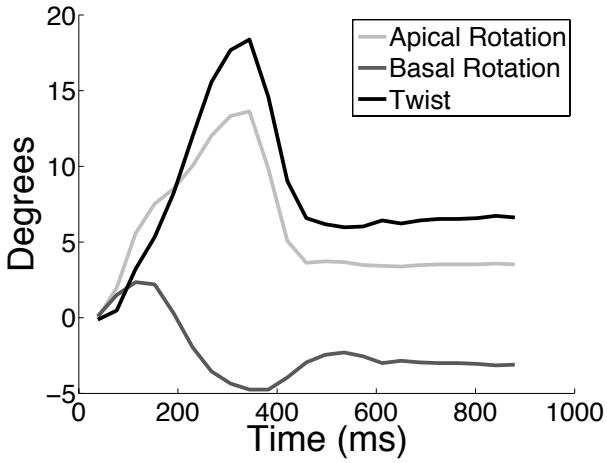


Figure 1. Temporal Sequences of left ventricular twist during the cardiac cycle. The units of the y-axis are degrees and the x-axis are ms. The light gray line depicts apical rotation, the dark gray line depicts basal rotation and the black line is the difference between apex and base.

It is believed that contraction of epicardial fibers rotates the apex in the counterclockwise direction and the base in a clockwise direction. Contraction of the subendocardial region results in rotation of the apex in a clockwise direction and the base in a counterclockwise direction. When the epicardium and endocardium contract together the epicardial fibers have a mechanical advantage since they have a larger radius of rotation (21).

The apex to base sequence of electromechanical activation leads to a subendocardial shortening sequence accompanied by subepicardial fiber stretching. Both the shortening and stretching contribute to the short clockwise rotation of the apex. The transmural spread of electrical activation leads to subendocardial to subepicardial shortening. The larger radius of the subepicardium results in greater torque, thus dominating the direction of rotation (22). This results in a global counterclockwise rotation near the apex and clockwise rotation near the base at the time of ejection. The resulting twist adds to contraction in the

principle fiber direction in the subepicardium. This in turn enhances shortening in the circumferential direction (23). In the subendocardium, the torque induces fiber rearrangement which deforms the matrix and results in stored potential energy that is used for diastolic recoil (21).

Torsional recoil at the time of isovolumic relaxation and early diastole allows for the release of the potential energy stored in the subendocardium. Subendocardial fibers lengthen near the apex and recoil in a clockwise direction, while shortening of the subendocardial fiber occurs at the base (17). The shortening and lengthening vectors in the left ventricle start diastolic restoration without volume changes (21). Torsion aids in distribution of fiber stress and fiber shortening across the left ventricular wall (24).

LV Twist and Disease

LV twist has been shown to change under different loading conditions. Increasing preload, a measure of the distending force, stretch, of the ventricular wall at end diastole, leads to an increase in twist. Increasing afterload, a measure of the resisting force of the ventricle during systolic ejection, contraction, leads to a decrease in twist. The effect of preload is about two-thirds as great as that of afterload on twist (25). It has also been shown that twist increases with increasing age. This increase is thought to be caused by an attenuation in subendocardial function and an unopposed increase in LV apical rotation (26).

Twist has been a proposed imaging biomarker for LV dysfunction for a number of cardiac diseases. Aortic stenosis, a condition in which the aortic valve does not fully open, has been shown to significantly increase peak LV twist (27, 28). Chronic mitral regurgitation, a condition in which the mitral valve does not close properly, has been shown to decrease peak LV twist. It is believed that this decrease occurs because of a decreased leverage of the epicardial fibers relative to the endocardial muscle fibers (29, 30). Dilated cardiomyopathy, a condition in which the heart is weakened and enlarged, has been shown

to lead to a decrease peak LV twist. It is believed that a marked attenuation of LV apical rotation occurs and basal rotation may be spared (31). However, in hypertrophic cardiomyopathy, a condition in which the heart muscle thickens, peak LV twist has been shown to increase. It is thought that the apex to base progression of the rotation sequence is altered, such that the midlevel of the LV rotates in a clockwise direction, similar to that of the base (32, 33).

Dissertation Motivation

The currently available open-source software for MR tag analysis from which measurements of displacement and rotation of the LV can be made is FindTags(34). FindTags is the gold-standard software for LV twist measurement and was also used to validate HARP(35) for MRI tag analysis. FindTags semi-automatically tracks the position of tag intersections in image space over time. It requires a user to draw an accurate line over every tag (horizontal and vertical) in every frame for every slice location in order to track all tag intersections and provide displacement and rotation information. Even with the use of the semi-automated tag detection algorithm, this process can take over a minute per image of user interaction. Depending on the number of images in a series, it can take up to an hour per patient.

HARmonic Phase (HARP) (35) MRI tag analysis is a more recent method for quantifying LV twist from tagged MRI. HARP uses the harmonic phase from a peak (i.e. stimulated echo) found in Fourier space to track phases over time. A harmonic peak is filtered and then transformed back to image space. The angle derived from the arctangent of the real and imaginary parts of the image is called the HARP angle and is used to track deforming tag lines on the image with respect to time. The HARP software provides access to cardiac displacement from which estimates of LV rotation (e.g. twist and torsion) can be determined with only two to three minutes of user interaction (35). The software is readily available for

purchase from the Diagnosoft company, but open source versions are not in widespread use.

The purpose of this dissertation was to develop, validate, and apply a novel method (Fourier Analysis of STimulated Echoes) for the rapid and accurate quantification of LV twist from tagged MR images requiring limited user interaction. Expensive software or an hour of user interaction per patient make the currently available methods for measuring LV twist from MR tagging unrealistic for use in many clinical settings. FAST requires users to contour the epicardial boundary of the LV in each of the tagged image series in one end-systolic frame. This short user interaction time has a clear advantage over the FindTags approach. The contoured images are transformed to Fourier space and the rotation of the stimulated echo and anti-echo are determined using cross-correlation. The novelty of the method is based on the fact that rotation in image space directly corresponds with rotation in Fourier space.

FAST estimates of LV twist were validated using intra- and inter-observer comparison, intra- and inter-scan comparison, and comparison to values derived from a 'gold-standard' technique, FindTags. FAST was used in conjunction with a CMR imaging technique, CSPAMM, designed to lengthen the duration of myocardial tag detection to acquire diastolic twist information. FAST was then applied to an imaging technique, ORI-CSPAMM, developed to minimize chemical shift induced myocardial tagging pattern artifacts, which produces more accurate measurements of LV twist. Next, FAST was used in combination with two free-breathing techniques to determine the impact of free-breathing on FAST estimates of LV twist and allow access to twist in patients with limited breath-holding capabilities. Finally, FAST was used to characterize differences in LV twist in patients with moderate and severe mitral regurgitation.

CHAPTER 3

Fourier Analysis of STimulated Echoes (FAST) for the Quantitative Analysis of LV Twist[1]

INTRODUCTION

Alterations in left ventricular (LV) twist are important in many pathophysiologies including myocardial infarction (36), dilated cardiomyopathy (37), mitral regurgitation (38), diastolic dysfunction (39) and aging (40). LV twist is a measure of the rotation of the apex relative to the base of the heart. Herein, we exploit the fact that object rotation in image space directly corresponds to a rotation in Fourier space. When spatial modulation of magnetization (SPAMM) tagging is employed, stimulated echoes form dominant features in magnitude Fourier space. With appropriate image processing, quantitation of the rotation of the stimulated echoes about the center of Fourier space corresponds to a rotation of the LV SPAMM tags. We have developed and validated a quantitative method termed Fourier Analysis of STimulated echoes (FAST) that requires limited user interaction for the quantitative analysis of LV twist**.** This study validates a novel method for the rapid quantification of left ventricular twist from tagged magnetic resonance images, evaluates the intra- and interobserver variability in the assessment of twist in six canine studies and eight healthy human subjects. We also demonstrate the utility of the FAST method in a series of twelve additional healthy human subjects.

MATERIALS AND METHODS

Animal Protocol

The animal protocol was approved by the institution's animal care and use committee and adhered to guidelines set forth by the National Institutes of Health. Six beagles were anesthetized with a 0.1ml intramuscular injection of Acepromazine and then 2.5% solution of

[1] This work has previously been published in the Journal of Magnetic Resonance Imaging.

Sodium Pentothal at 1ml/2.3kg intravenously. The animals were then placed on positive pressure ventilation with 1.5% isoflurane for the duration of the scan. Animals were fitted with a right atrial-pacing electrode using fluoroscopic guidance. The pacing electrode was used for both sensing cardiac rhythm or for pacing.

Canine MRI Protocol

Imaging was performed using a General Electric 1.5T CV/i scanner (GE Healthcare, Waukesha, WI, US) and a 4 element phased array knee coil. Short axis stripe tagged images were acquired using a modified 3D fast gradient echo pulse sequence with the following parameters: 180mmx180mmx128-160mm field of view, 384x128x32 acquisition matrix, 12° imaging flip angle, ±62.5kHz bandwidth, TE/TR=3.4/8.0ms, 5 pixel (2.3mm) tag spacing, and 4 or 5mm slice thickness. The sequence was also modified to include segmented multiphase imaging, combined respiratory and cardiac gating, and 1-3-3-1 spatial modulation of magnetization (SPAMM) tagging. Further modifications implemented a spatial frequency dependent number of views per segment (VPS) in order to reduce the acquisition time by a factor of 3.2 (41). Briefly, the highest phase-encoded spatial frequencies were acquired using VPS=8 and lower spatial frequencies were acquired with VPS=4 and VPS=2. The lowest spatial frequencies were acquired with VPS=1. Fifty-eight to sixty cardiac phases were reconstructed per slice, depending upon the heart rate.

In order to image for extended durations a reliable and robust respiratory gating technique was implemented. The respiratory pressure waveform was sampled at the proximal end of the endotracheal tube using the scanner's bellows transducer. The respiratory signal from the bellows transducer was then sampled by the pulse sequence throughout the scan to determine periods of minimal respiratory induced cardiac motion during end-expiration. The use of right atrial pacing provided the ability to phase lock the respiratory and cardiac motion to further minimize motion artifacts and also provided the

ability to start the imaging sequence prior to systolic contraction in order to image the complete extent of systolic contraction.

The canine data was also incorporated, in part, because of its availability and relevance to basic science research for which tagging techniques have broad applicability. The canine data was used in this study as part of the validation of the FAST method and to perform inter- and intra-observer analysis.

Healthy Subjects MRI Protocol

The local institutional review board approved this study and all subjects provided written informed consent. Eight (5 male, mean age of 37.0 years +/-17.0 years, weight 68.4+/-16.9 kg, height 1.7+/-0.2 m, heart rate 58.2+/-10.8 beats/min) healthy human subjects with no history of cardiovascular or respiratory disease were studied for comparison with FindTags. Additionally, twelve (10 male, 2 female, mean age of 26.4 years +/-4.3 years, weight 80.8+/-20.3 kg, height 1.8+/-0.1 m, heart rate 74.5+/-11.8 beats/min) healthy human subjects with no history of cardiovascular or respiratory disease were studied using only FAST.

An Avanto 1.5T scanner (Siemens Healthcare, Erlangen, Germany) and a six element body matrix coil in combination with a six element spine matrix coil were used, while the subjects rested in a head first supine position. All image were acquired with ECG triggering while the volunteer held his or her breath at end-expiration. Scout images were obtained in the axial, coronal, and sagittal orientations, which were then used to plan the study. A steady-state free precession cine sequence in parallel short-axis planes was used to select slices for acquisition of tagged images and subsequent twist measurements. The two short axis slices consisted of an apical slice and a basal slice selected based on the following criteria respectively: the most apical slice containing the presence of the blood pool throughout the entire cardiac cycle and the most basal slice in which the LV myocardium maintained a continuous annular shape during the entire cardiac cycle. Twist was calculated

as the difference in the angle of rotation for matching frames between the apical and basal slices.

The same modified 1-1 SPAMM line tag sequence and the unmodified Siemens 1-3-5-3-1 SPAMM line tag sequence were used to acquire short-axis images in healthy volunteers (n=8) at the base and apex of the LV with the following parameters: 360-300x300-280mm FOV, 5-6mm slice thickness, 192x144 acquisition matrix, 15° imaging flip angle, 501 Hz/pixel receiver bandwidth, TE/TR = 3.5-3.7/4.7-6.5 ms, 7-8 VPS, 2 averages, and 14-16 cardiac phases. Cine images were acquired for both horizontally and vertically tagged images with a 10mm tag spacing for both apical and basal slices. The average breath hold time was 23.8 seconds.

A cardiac spoiled gradient echo MRI pulse sequence was modified to support 1-1 SPAMM line tags and used to acquire short-axis images in healthy volunteers (n=12) at the base and apex of the LV with the following parameters: 300x300mm FOV, 5mm slice thickness, 192x96 acquisition matrix, 15° imaging flip angle, 250 Hz/pixel receiver bandwidth, TE/TR = 5.2-5.4/9.15ms, 4 VPS, and 18-24 cardiac phases. Cine images were acquired for both horizontally and vertically tagged images with an 8mm tag spacing for both apical and basal slices. The average breath hold time was 28.7 seconds.

Tag Tracking

Tissue tags in two short axis slices were tracked semi-automatically using the FindTags (42) software, which we define as “gold standard” results. FindTags was used as our gold standard because the software was readily available. Harmonic phase (HARP) imaging analysis is an alternative commercially available FDA approved software package (Diagnosoft, Cary, North Carolina, USA) that is commonly used to calculate twist (43). The “gold standard” estimates of LV rotation at basal and apical slice levels for the duration of

trackable tag persistence were obtained from the rotation of horizontal and vertical tag intersections about the LV centroid determined using FindTags.

FindTags requires binomially weighted (e.g. 1-3-3-1 or 1-3-5-3-1) tagged images to accurately track tag intersections. Note, these 1-3-5-3-1 SPAMM tagged images were not available for the second healthy subjects (n=12) population. The data from this second group of healthy subjects was used as further evidence of the capabilities of the FAST method. 1-3-3-1 SPAMM data was used during the FindTags analysis of canine twist and 1-3-5-3-1 SPAMM was used during the analysis of twist in normal subjects due to the availability of data. This subtle difference in tag generation is not expected to impact the results.

Fourier Analysis of STimulated echoes (FAST)

The only user interaction required for FAST LV twist analysis is contouring of the LV epicardium in an end-systolic frame at the basal and apical slice level (Figure 1). The epicardial contour was used for least squares fitting of an ellipse to the LV epicardial boundary. The long and short axes of the ellipse were used to define the location of 90% attenuation of the 2D fourth-order Butterworth mask and the orientation (rotation) of the fit ellipse was used to rotate the 2D Butterworth mask. Masking was necessary to define the region of interest (i.e. LV myocardium), thereby eliminating tissues that did not rotate from further analysis. Butterworth filters also reduce ringing subsequent to 2D Fourier transformation, Figure 1C. The same mask is applied to each subsequent frame in the same dataset. The epicardial contour displaces <1 pixel throughout the cardiac cycle, therefore the individual epicardial contours on each frame are largely the same. The endocardial border displaces much more, but due to the lack of tag coherence in the blood pool a mask is not needed. Subsequent to masking, the image was 2D Fourier transformed and the center peak (free induction decay, FID) in the Fourier image was nulled with a circular mask

to reduce the interference of the high FID signal intensities (low spatial frequency) during the detection of object rotation Figure 1D. Next, the image was cropped (depending on the direction of phase encoding) so that only the central 64 lines of k-space (-32 to +32) remained, which reduced the matrix size and subsequent processing time, Figure 1E.

The Fourier magnitude data for each frame was 2D cross-correlated with a bi-cubic interpolated, rotated (step-size of 0.1°) version of the frame immediately after it within the same slice. The maximum of the two-dimensional cross-correlation from all tested rotations defined the angle of rotation between those frames. The cumulative angle of rotation for each frame is equal to the sum of the angles of rotation from the frames before it plus the current cross correlation angle of rotation for the frame. This process was repeated for all frames in the basal and apical slices. The angle of rotation computed from the horizontal and vertical tags was averaged within matching time frames for both the apical and basal slices. Twist was calculated as the difference in the angle of rotation for matching frames between the apical and basal slices. Peak twist was defined as the maximum twist value for each subject. Matlab R2007a (The MathWorks, Inc., Natick, MA, USA) was used for all processing on a MacBook Pro (Apple, Cupertino, CA, USA) with a 2.4 GHz Intel Core 2 Duo processor. 1-1 SPAMM was used during the FAST analysis of twist in normal subjects and 1-3-3-1 SPAMM data was used during the FAST analysis of canine twist due to the availability of data. 1-1 SPAMM images were used for FAST analysis because it was expected that the image intensity and distribution of the dominant Fourier space features (stimulated echoes) would be more accurately detected by cross correlation (see Discussion).

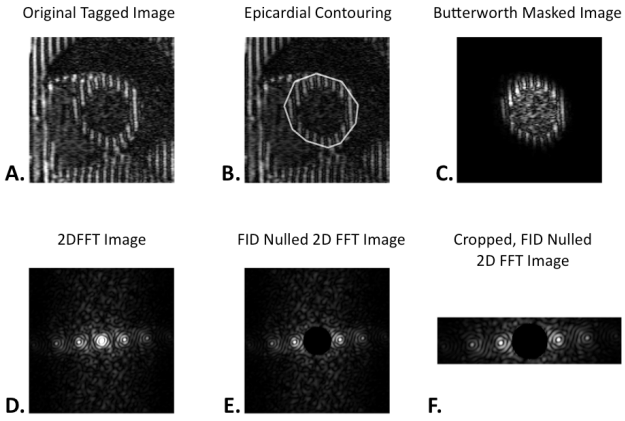


Figure 1: The FAST method is used to estimate left ventricular (LV) rotations from conventional SPAMM tagged images (A). The image is first manually contoured (B) and segmented with a two-dimensional Butterworth filter matched to the contours (C) to isolate the LV myocardium. The segmented image is then Fourier transformed (D) and the free induction decay is nulled (E), before cropping (F). The final step of the FAST algorithm involves 2D cross-correlation with another cardiac phase in order to estimate the LV rotation.

Statistical Analysis

Intra- and inter-observer analysis was performed for the canine studies, wherein the left ventricular epicardium and endocardium at end systole were each contoured twice by two investigators. Each trial consisted of contouring basal and apical slices for each of the six canine studies. For each trial, the mean and standard deviation of peak systolic twist were calculated and compared. The intra-observer coefficient of variation, CV_{INTRA} , was calculated for each investigator as the standard deviation of the peak systolic twist from both trials times 100 divided by its mean. The inter-observer coefficient of variation, CV_{INTER} , was calculated for each trial as the standard deviation of the mean difference between observers

in peak systolic twist times 100 divided by its mean. Linear regression analysis of twist values (six canine studies, each comprised of 40 analyzable cardiac phases) from the two investigators against the FindTags results was performed by calculation of Pearson's correlation coefficient (R). Peak systolic twist for all canine trial combinations (e.g. Observer #1-Trial #1 vs. Observer #2-Trial #2) was compared using the Wilcoxon signed-rank test for paired non-parametric samples. The paired t-test was used to compare the canine twist values from each trial with the FindTags twist values of each cardiac phase. P-values less than 0.05 were considered significant. Bland-Altman analysis is used to compare two measurement techniques (44). A Bland-Altman analysis for the first two-thirds of the cardiac cycle (before tag rotation becomes undetectable by either method) was performed to compare all of the canine FAST twist data collected by both investigators to that of the FindTags data.

Additionally, linear regression analysis of healthy subject twist (n=8) for the first 500 ms of the cardiac cycle (before tag rotation becomes undetectable by either method) derived from the FAST method and FindTags was performed by calculation of Pearson's correlation coefficient (R). Peak systolic twist for healthy subjects was compared using the Wilcoxon signed-rank test for paired non-parametric samples. The paired t-test was used to compare healthy subject (n=8) twist values for the first 500ms of the cardiac cycle from the FAST method with the FindTags twist values of each cardiac phase. A Bland-Altman analysis for the first 500ms of the cardiac cycle was performed to compare healthy subject (n=8) FAST twist data collected to FindTags data.

RESULTS

Validation in Canines

The mean peak systolic twist for Investigator 1 was 10.3°±2.2° and 10.1°±2.5° (Trial #1 and #2 respectively). The mean peak systolic twist for Investigator 2 was 10.4°±2.6° and

10.2°±2.5° (Trial #1 and #2 respectively). Mean peak twist derived using FindTags was 11.4°±2.7°. CV_{INTRA} for peak systolic twist for Investigator 1 and 2 were 2.9% and 2.6% respectively. CV_{INTER} for peak systolic twist for Trial #1 and #2 were 4.3% and 4.2% respectively. The mean difference in peak systolic twist for Trial #1 and Trial #2 were -0.15°±0.4°and -0.13°±0.4° respectively. Linear regression analysis of FAST twist values from the two investigators (960 data points) and the FindTags results yielded a Pearson's correlation coefficient of R=0.95 and the equation FAST=0.9FindTags+0.8 (Figure 3B). Linear regression analysis of Investigator 1 and Investigator 2 yielded a Pearson's correlation coefficient of R=0.99 and the equation y=1.0x-0.05. The Wilcoxon signed-rank test did not reveal any significant differences between the peak systolic twist for any combination of trials. No significant differences were detected by the paired t-test for FAST twist values from each trial compared to the FindTags twist values in each cardiac phase. Figure 2, compares the FAST twist and FindTags results (mean±SD) for six canine studies and demonstrates good agreement between the two methods.

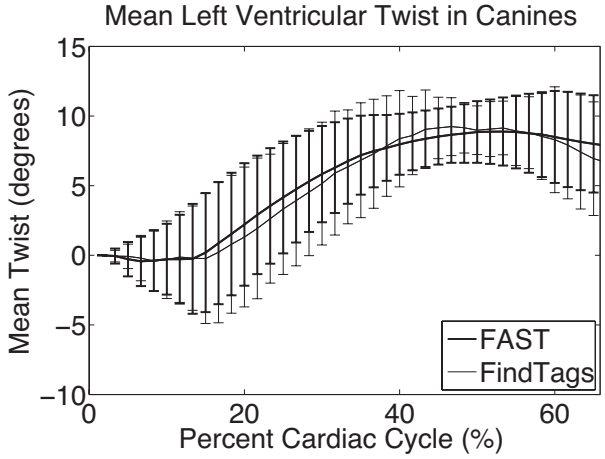
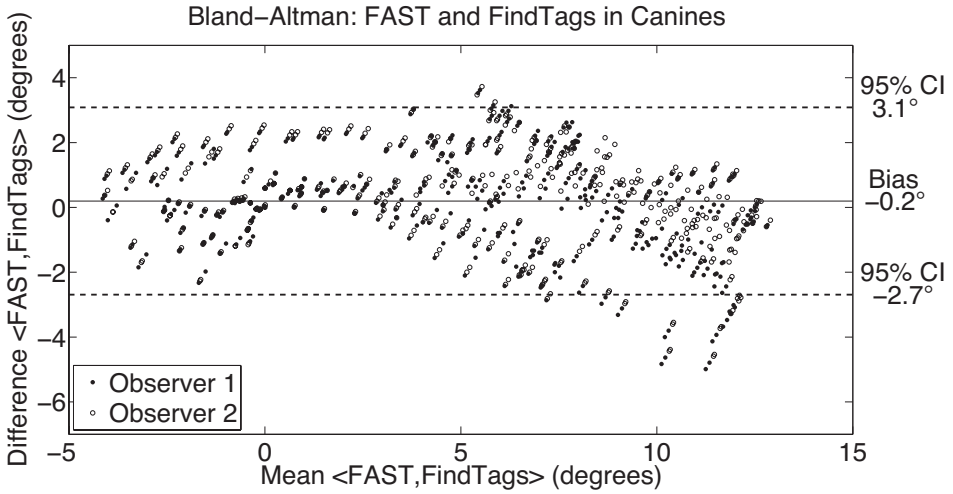


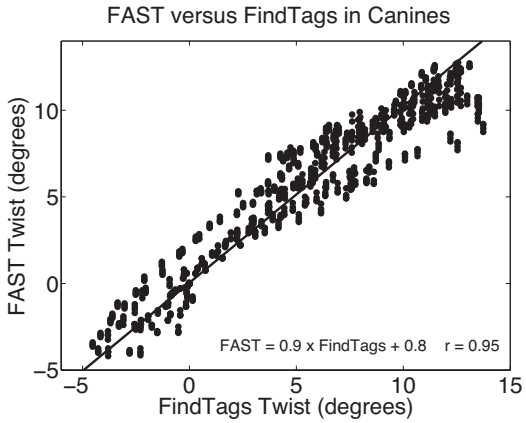
Figure 2: The mean LV twist from 6 different canines is plotted as a function of percent cardiac cycle for both FindTags ("gold standard") and the FAST method. Error bars indicate

±1 standard deviation. No statistically significant differences between the techniques were observed, which indicates FAST is a suitable alternative to FindTags analysis.

Bland-Altman analysis for the first two-thirds of the cardiac cycle compares all of the FAST twist data collected by both investigators to the FindTags data (Figure 3). There is excellent agreement between FAST and FindTags for calculating LV twist with a bias (FAST-FindTags) of 0.2° and 95% confidence intervals of (-2.7°,3.1°). Intra-observer Bland-Altman analysis for the first two thirds of the cardiac cycle for Investigator 1 and 2 yields a bias of 0.1° and 0.1°and a 95% confidence interval of (-0.3°,0.5°) and (-0.3°,0.5°) respectively. Inter-observer Bland-Altman analysis for the first two thirds of the cardiac cycle for Investigator 1 and 2, Trial 1 compared to Trial 1 and Trial 2 compared to Trial 2, yields a bias of 0.1° and a 95% confidence interval of (-0.5°,0.4°).



A.



B.

Figure 3: (A) Bland-Altman analysis of canine LV twist for each investigator using the FAST method is compared to the FindTags ("gold standard") results indicates excellent agreement between the two methods with a bias of 0.2° and a variance of (-2.7°, 3.1°). (B) Linear Regression analysis of canine LV twist for both investigators using the FAST method is compared to FindTags and results in the equation FAST=0.9FindTags+0.8 (R=0.95).

The average user interaction time for the FAST method was 2.6±0.3 minutes; this time includes study selection and contouring of the epicardium and endocardium for the basal and apical slices for both horizontal and vertical tags. Since the tags deform in both the horizontal and vertical directions both sets of tags are needed to properly quantify LV twist. User interaction times for the FindTags data were not available, but typically average 30-60 seconds per image. The average computational time for the FAST algorithm was a total of 37 minutes for the horizontal and vertical tags at the basal and apical slice level (4 separate sets of images containing 40 frames each with a matrix size of 256x64).

Validation in Healthy Subjects

Linear regression analysis in healthy subjects (n=8) for the first 500 ms of the cardiac cycle with FAST twist values and FindTags results yielded a Pearson's correlation

coefficient of R=0.91 and the equation FAST=0.9FindTags, (Figure 5B). The Wilcoxon signed-rank test of the same data did not reveal any significant differences between the peak systolic twist for any combination of trials. No significant differences were detected by the paired t-test for FAST twist values compared to the FindTags twist values in each cardiac phase. Figure 4, compares the FAST twist and FindTags results (mean±SD) for eight healthy subjects and demonstrates good agreement between the two methods. Peak systolic twist and early diastolic untwisting are clearly visible in all cases (Figure 4). Figure 4 shows incomplete untwisting because the tags have faded too much for quantitative analysis. Bland-Altman analysis for the first 500 ms of the cardiac cycle compares the FAST twist data to the FindTags data (Figure 5). There is excellent agreement between FAST and FindTags for calculating LV twist with a bias (FAST-FindTags) of -0.5° and 95% confidence intervals of (-4.3°, 3.4°). Mean peak twist derived from the FAST method (n=8) was 11.5°±2.3° and 12.6°±1.6° using FindTags. The mean peak LV twist from all of the healthy volunteers (n=20) using FAST was 10.5±1.9° with an average user interaction time of 2.7±0.4 minutes and an average post processing time of approximately 21 minutes.

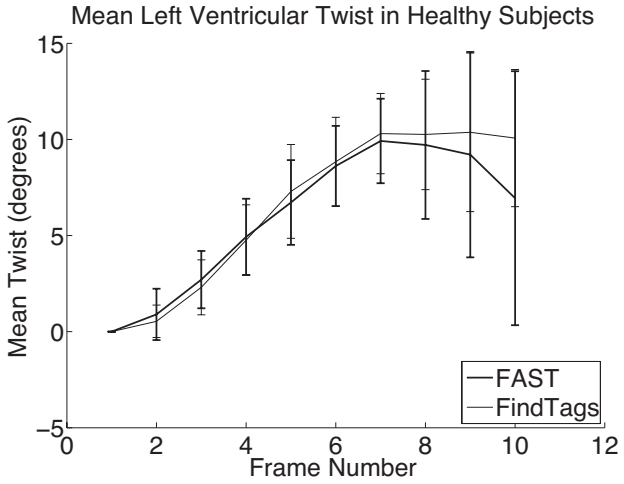
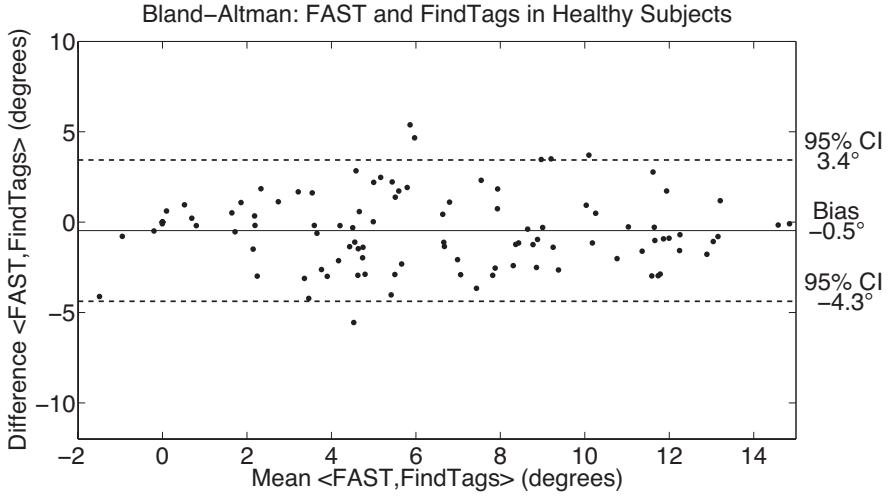
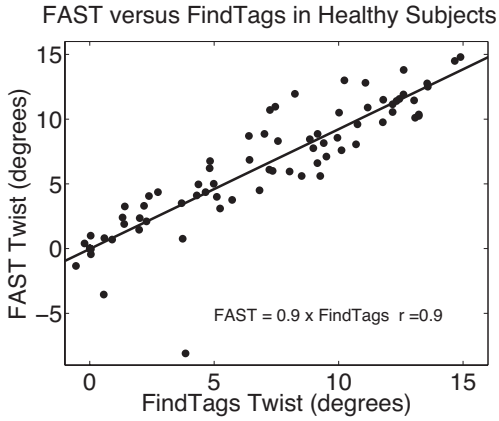


Figure 4: LV twist in 8 healthy subjects is plotted above as a function of frame number for the first 500 ms of the cardiac cycle for both the FAST method and FindTags the “gold

standard". Error bars indicate ±1 standard deviation. Systolic twisting and early diastolic untwisting are both evident. The peak twist observed in these subjects is in good agreement with previously published results, indicating that the FAST method produces expected results with limited user interaction.



A.



B.

Figure 5: (A) Bland-Altman analysis of healthy subject LV twist using the FAST method is compared to FindTags ("gold standard") results indicating excellent agreement between the two methods with a bias of -0.5° and a variance of (-4.3°, 3.4°). (B) Linear regression analysis of healthy subject LV twist using the FAST method is compared to FindTags and results in the equation FAST=0.9FindTags (R=0.91).

DISCUSSION

In the present study, we evaluated the performance of the FAST method as compared with FindTags for the quantification of LV twist. The FAST algorithm for quantifying LV twist is a fast, reliable, and reproducible method. Furthermore, the quantitative results from FAST LV twist analysis compare very favorably (no statistical differences, negligible bias) with the FindTags ("gold standard") results and the user analysis times were short (<3 minutes per study). Inter- and intra-observer agreement of the FAST method for measuring LV twist was very good.

The FAST method incorporates four important techniques: a 2D Butterworth mask, FID suppression, matrix cropping, and 2D cross-correlation. The primary function of the 2D Butterworth mask is to isolate the rotating myocardial tissue and suppress stationary tissue. Without the use of this mask, the FAST method would return twist values based on the entire tagged cardiac MR image including the chest wall. The currently implemented FAST algorithm is relatively insensitive to the precise 2D Butterworth filter used, so long as the stationary tissues are sufficiently suppressed.

The Butterworth filter is used in the spatial domain to reduce ringing artifacts after transformation to the Fourier domain. Subsequently a circular mask is applied directly in Fourier space to null the FID. This array is not transformed back to the spatial domain, therefore ringing is not an issue and the difference between using a circular filter and a Butterworth filter with a few pixel roll-off are likely negligible.

FID suppression was used to minimize the effects of the highest intensity low spatial frequencies, which can interfere with estimates of object rotation. Bland-Altman analysis of the FAST method without FID suppression and FindTags for one trial had a bias of 0.13° and a CI (-2.7,3.0), which indicates that FID suppression may not be necessary. An alternative strategy for minimizing the FID is CSPAMM (6) which effectively nulls the FID

due subtraction of the two complementary tagging patterns. Lastly, the Fourier space matrix is cropped to the central 64-lines in the phase-encode direction after FID suppression in order to reduce image processing time (14.8 times faster than processing times using original size images of 256x256). Cropping along this dimension reduces the spatial frequency content along the tag's length and has a negligible effect on the quantitative results. Bland-Altman analysis of FAST without cropping and FindTags for one trial had a bias of 0.22° and a CI(-2.6,3.1). This bias is better than that of the cropped FAST method, but not significantly different. Nevertheless, the time savings gained from cropping the matrix makes up for it.

Strong correlation and agreement of twist measurements between FAST and FindTags were found in the present study. Compared to FindTags, for which the user interaction time requires many tens of minutes, the FAST processing significantly reduces both user interaction time and the analysis time and produces comparable results. The computational processing time of the FAST method, despite running automatically after initial contour selection, is a current limitation. Methods that will reduce the processing times include using a faster computer, a better optimization algorithm, a measure of image similarity between each rotated frame that is faster to compute than cross-correlation, and a transform to polar coordinates for direct rotation estimates.

The FAST method yields robust measurements of LV twist, with strong inter- and intra-observer agreement. The mean LV peak systolic twist for each investigator and each trial were not significantly different indicating excellent user agreement and highly reproducible analysis. The mean peak systolic twist values from the healthy human subjects were in good agreement with previously reported value of 10.4° ± 2.6° (45), which apical and basal slice selection criteria similar to the criteria used in this study. However, there is a range of literature values reported for LV twist in healthy human subjects (46). Differences in the value between the mean peak LV twist value reported in this study and that reported across

the range of studies in the literature may result from the slice selection criteria and differences in the subject population. In addition to having good agreement with mean peak twist literature values, the measurements from both investigators matched well with the FindTags ("gold standard") values.

With regards to the variability within each measure, we note that the selected slices are 5-6mm thick with approximately 10cm between the apical and basal slices. The slice position may be different between volunteers by approximately half a slice (2.5-3.0mm) from the desired anatomic slice locations as described in the Methods section, which may account for a ~0.5° degree of rotation, or 5% of the variability. Reproducibility studies or simulations are needed to appropriately address the other sources of variability in the peak twist measurement. Importantly, FAST and FindTags do not appear to have significantly different variability, which leads us to conclude that intra-subject variability may be the largest component of the variability.

The FAST method performs well with 5mm slices, which also helps reduce intra-slice shear effects. For thick slices, a within slice shear may reduce the sensitivity for measuring rotations with the FAST method, effectively smearing the stimulated echo and stimulated anti-echo and reducing the rotation measurement. If the short-axis prescription is tilted relative to the LV long-axis, then errors may be introduced in the twist measurements. The incorrect short axis prescription may result in an inter-slice heterogeneity in rotation as a consequence of the projection of LV rotation onto a plane whose normal is skew to the axis of LV rotation. The FAST method may have a more difficult time detecting rotation as the stimulated echo and stimulated anti-echo will be smeared. This may be an inherent limitation of the FAST method when compared to FindTags. FindTags should not be limited in detecting tag intersections despite the skewed axis and as a result should accurately estimate the rotation of the imperfect short-axis slice.

The healthy human data was acquired using 1-1 SPAMM tagging. The primary reason for the use of 1-1 SPAMM tagging over the product provided sequence (1-3-5-3-1 SPAMM) was due to the image intensity and distribution of the dominant Fourier space features (stimulated echoes and free-induction decay, FID) in the Fourier transformed tagged image. The stimulated echoes arise as a consequence of tag generation. In the case of 1-1 SPAMM tagging the majority of the image intensity is distributed between two stimulated echoes and the FID, whereas in the product sequence the image intensity is distributed across six stimulated echoes and the FID. As the tags fade later in the cardiac cycle, the Fourier transformed images suffer a loss of contrast to noise ratio as a direct result of the lack of tag detectability. Thus, 2D cross correlation is less effective later in the cardiac cycle. The use of 1-1 SPAMM tagging allows the stimulated echo intensities to remain higher than that of background noise for a longer duration of the cardiac cycle compared to the product provided sequence and may improve quantitative estimates of LV twist. Future improvements in the tagging sequence (33, 47, 48) may improve quantification of LV untwisting during diastole, thereby further extending the utility of the FAST method.

The FAST method for calculating LV rotation is based on a comparison of temporally adjacent frames and the total rotation arises from the summation of inter-frame rotations, but inter-frame errors can also arise from this process. One alternative to determining angle of rotation would be to compare only the first frame with each subsequent frame. One problem with this approach is the significant change in tag orientation and contrast from the first frame to last frame. In this case error may arise due to the large changes between images. Furthermore, a different search algorithm would need to account for a wider range of possible rotations. It is also important to note that the current implementation of the FAST method is designed to calculate global LV twist, unlike HARP, FindTags, or DENSE (49), which can compute regional differences in twist and strain. For cardiac diseases with

significant within slice rotational heterogeneity, the stimulated echo and stimulated anti-echo may smear enough to make accurate estimates of global rotation difficult.

The optimal imaging strategy for efficiently acquiring MRI data amenable to the fast and accurate analysis of LV twist remain the subject of ongoing investigation. The optimal strategy will likely reflect a balance of Fourier peak amplitudes relative to the noise levels in Fourier space, breath hold limitations, FID nulling strategies (filters versus CSPAMM), line tags versus grid tags and parallel imaging. The FAST method for quantifying LV twist produces quantitative results that are equivalent to the current “gold standard” in a fraction of the user interaction time and has demonstrated applicability in human subjects. While user interaction time is under 3 minutes, full automation of this technique is a necessity for clinical acceptance.

CHAPTER 4

Quantitative Assessment of Systolic and Diastolic Left Ventricular Twist Using Fourier Analysis of STimulated Echoes (FAST) and CSPAMM[2]

INTRODUCTION

Left ventricular (LV) twist is a quantitative measure of the rotation of the apex relative to the base of the heart. Alterations in LV twist are important in many diseases including aortic stenosis(27, 28, 50), diastolic dysfunction(39) and aging(51). Peak twist has been shown to decrease in patients with systolic heart failure, mitral regurgitation(30), transmural infarction, dilated cardiomyopathy and constrictive pericarditis and increase in patients with aortic stenosis(27, 28, 50), increased age(51), diastolic heart failure, hypertrophic cardiomyopathy, and restrictive cardiomyopathy(21). Diastolic dysfunction is reported to precede systolic heart failure(52) and may be a useful measure for the early diagnosis of heart failure. Therefore, a fast, efficient, and quantitative method for diagnosing and longitudinally evaluating diastolic dysfunction is clinically important(27, 51, 53-55). Sengupta et al proposed an algorithm for evaluating twist from MRI and echo images in daily clinical practice and have suggested that LV twist may provide better 'insight into the mechanism of heart failure' compared with traditional concepts, which focus on the hemodynamic consequences of LV dysfunction (21). Hence, the evaluation of systolic and diastolic LV twist has increasing clinical relevance.

Fourier Analysis of STimulated echoes (FAST) (56) has been recently validated in conjunction with SPatial Modulation of Magnetization (SPAMM)(5) as a method to quantify LV twist based on measuring LV rotation directly in Fourier space. The tag contrast generated by the SPAMM pulse sequence fades quickly during the cardiac cycle and typically limits estimates of ventricular motion using, for example, FAST+SPAMM to systolic

[2] This work has been previously published in the Journal of Magnetic Resonance Imaging.

events at 1.5T. Complementary spatial modulation of magnetization (CSPAMM) (6) is an alternate tagging pulse sequence, which improves tag contrast late in the cardiac cycle thereby enabling the quantitative evaluation of both systolic and diastolic function.

Herein, systolic and diastolic LV twist and torsion parameters have been estimated in thirteen (n=13) healthy volunteers using FAST+CSPAMM (6) and compared to the results from FAST+SPAMM. FAST analysis typically requires 2-3 minutes of user interaction time, after which the process is completely automated. In addition, a new measurement for quantification of late diastolic untwisting has been proposed – the ratio of rapid untwist to peak twist. This measure provides insight into the contribution of atrial systolic untwisting to the completion of the twist cycle. The FAST method has also been updated to estimate rotation in the first cardiac frame and to null coherent tags in the blood pool during the first few cardiac frames, which can erroneously contribute to measures of LV rotation and twist.

MATERIALS AND METHODS

Healthy Subjects MRI Protocol

The local institutional review board approved this study and all subjects provided written informed consent. Thirteen (3 female, mean age of 32.5±11.2 years, weight 70.5±12.7 kg, height 1.7±0.1 m, heart rate 54.8±9.2 beats/min) healthy human subjects with no history of cardiovascular or respiratory disease were studied.

A Siemens Avanto 1.5T scanner (Siemens Healthcare, Erlangen, Germany) and a six element body matrix coil in combination with a six element spine matrix coil were used for imaging while the subjects rested in a head first supine position. All images were acquired with ECG triggering while the volunteer held his or her breath at end-expiration. Scout images were obtained in the axial, coronal, and sagittal orientations, which were then used to plan the study. A balanced steady-state free precession cine sequence was acquired using a 6 mm slice thickness and a 66% gap between slices, in parallel left ventricular short-

axis planes and used to select basal and apical slices for acquisition of tagged images and subsequent image processing. The most apical slice containing the presence of the blood pool throughout the entire cardiac cycle and the most basal slice in which the LV myocardium maintained a continuous annular shape during the entire cardiac cycle were used to prescribe the two slices for tagging.

Both a cardiac gated spoiled gradient echo sequence was modified to support both 1-1 binomially weighted SPAMM line tags and 1-1 binomially weighted CSPAMM line tags (both with total tagging flip angle of 180°). These sequences were used to acquire short-axis images at the base and apex of the LV with the following parameters: 360-300x300-280mm field-of-view, 5-6mm slice thickness, 192x144 acquisition matrix, 501 Hz/pixel receiver bandwidth, TE/TR = 3.5-3.7/4.7-6.5 ms, 7-8 views (k_y-lines) per segment, and 14-16 cardiac phases. To facilitate an unbiased comparison between the CSPAMM tagged data and SPAMM tagged data the breath hold duration for each sequence were 21 and 22 heart beats respectively (19.6 ± 4.1 seconds depending upon heart rate), with one and two discarded heartbeat per acquisition respectively. The SPAMM data was acquired using two averages to maintain comparable SNR. The CSPAMM data was acquired without averaging, but required acquisition of two image sets with 180° RF phase cycling of the second tagging RF pulse. Additionally, a 15° imaging flip angle was used to acquire SPAMM images, while a non-linearly ramped flip angle (final 22°) was used to acquire CSPAMM images(7). Cine tagged images were acquired using both horizontal and vertical tagging in separate breath holds with 10mm tag spacing. Figure 1 demonstrates the difference in tag contrast and signal to noise for SPAMM and CSPAMM images with respect to time.

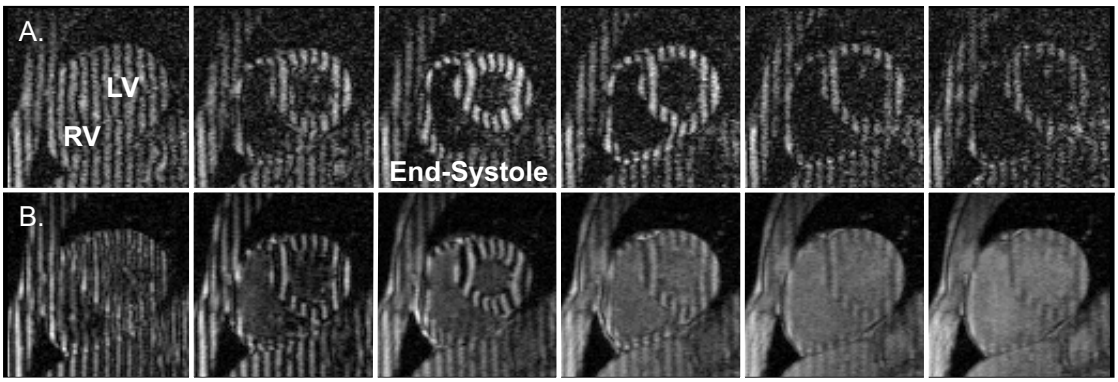


Figure 1: LV short axis images presented as a function of time (ms) demonstrate the higher apparent tag contrast in (A) CSPAMM compared to (B) SPAMM tagged images.

Fourier Analysis of STimulated echoes (FAST)

The only user interaction required for FAST(56) LV analysis was contouring of the LV epicardium in an end-systolic frame and endocardium in an early systolic frame at the basal and apical slice level. The FAST method utilizes the fact that a rotation in image space corresponds to rotation in Fourier space. Each contour was used for least squares fitting of an ellipse to the respective LV boundary. The long and short axes of the ellipse were used to define the location of 90% attenuation for a 2D fourth-order Butterworth mask and the orientation of the fit ellipse was used to rotate the 2D Butterworth mask. The original FAST method was updated to use a Butterworth filter derived from the endocardial contour and applied to the first three cardiac frames to suppress coherent tags in the blood pool, which can contribute to the apparent rotation if not attenuated. The tags in the blood pool dissipate in later frames making the endocardial filter unnecessary. The epicardial contour was used to isolate the LV myocardium in all cardiac frames. The segmented image was then Fourier transformed after which the free induction decay was nulled with a circular mask, which can improve estimates of rotation when the FID undergoes no apparent

rotation, but the LV image does. The next step crops the *k*-space matrix to the central 64 lines. The final step of the FAST algorithm involves 2D cross-correlation in Fourier space with another cardiac phase in order to estimate the inter-frame rotation. Inter-frame rotations are calculated for all cardiac frames, from which values of LV twist were derived. Figure 2 illustrates the different processing steps for the FAST method.

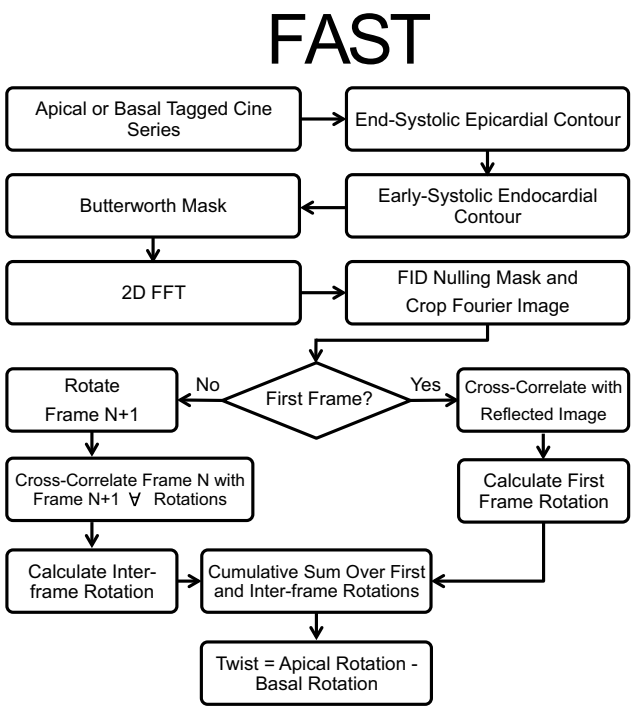


Figure 2: Flowchart of the updated FAST processing method.

Importantly, the FAST method has been updated to approximate the rotation of the first cardiac frame. It is possible for the first frame to have a non-zero rotation due to delays between the ECG signal and the time stamp for the image due to MRI tagging preparation and the temporal resolution of the MRI scan. To determine this rotation, the first frame was segmented using the Butterworth masks described above and subsequently Fourier transformed. The first frame was then reflected about the axis perpendicular to the tagging lines, the FID was nulled, and the reflected image was cropped as described above. Finally,

the reflected version of the first cardiac frame was 2D cross-correlated with the original segmented, nulled, and cropped first cardiac frame to estimate the first frame's rotation.

Left ventricular twist was calculated as the difference in the angle of rotation between the apical and basal slices for matching temporal frames with units of degrees (deg). Positive twist was defined as a counter-clockwise rotation when viewed from apex-to-base. Peak twist was defined as the maximum twist value for each subject. LV torsion was calculated as LV twist divided by the distance between the apical and basal slices with units of deg/cm. Peak torsion was defined as the maximum torsion value for each subject. Twist rate was calculated as the discrete derivative of twist with respect to time with units of deg/s. Peak twist rate was defined as the maximum twist rate. Peak diastolic untwist rate was defined as the minimum twist rate. Normalized peak untwist rate was defined as the minimum twist rate divided by the maximum twist angle with units of s^{-1}. All values were fully automated calculations made independent of user interaction subsequent to epicardial and endocardial contouring.

Data Processing

The FAST+CSPAMM and FAST+SPAMM estimates of rotation were used to calculate peak twist, torsion, twist rate, and untwist rate, mean peak values and timings for the apical and basal slices, and time of peak twist. The duration of untwisting was automatically estimated from data interpolated with a cubic smoothing spline. This smoothing was done to reduce noise and better detect the end of untwisting, which was determined automatically by finding the maximum of the second derivative of the twist data after peak systolic twist. The cardiac frame corresponding to the end of untwisting was used to estimate the ratio of rapid untwist to peak twist. The LV twists during systole until it reaches a peak value and then rapidly untwists during early diastole. Rapid, early diastolic untwisting, however, does not account for complete untwisting in healthy hearts. Atrial systole completes the process of untwisting. A similar phenomenon is apparent in LV strain curves(33). The ratio of rapid

untwist to peak twist, provides insight into the contribution of atrial systole to the completion of the untwisting process.

Figure 3 depicts the systolic and diastolic measures of twist calculated with FAST+CSPAMM and FAST+SPAMM. Peak systolic twist, systolic twist rates, and early diastolic untwisting are clearly visible for both FAST+CSPAMM and FAST+SPAMM results (Figure 3). FAST+CSPAMM results, however, also show the end of diastolic untwisting and continue into mid-diastasis. Figure 3 shows incomplete diastolic untwisting in the case of SPAMM because the tags have faded too much for quantitative analysis.

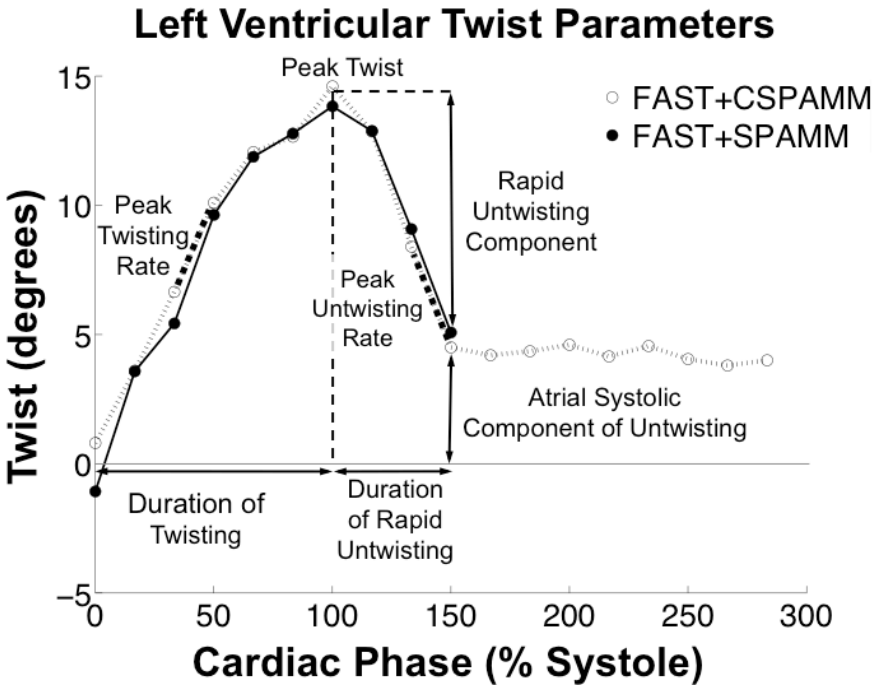


Figure 3: LV twist data from a single volunteer illustrates peak twist, twisting rate, untwisting rate, the component of rapid untwisting, duration of twisting, and the duration of rapid untwisting for FAST+CSPAMM and FAST+SPAMM. The ratio of rapid untwist to peak twist was used as a measure of late diastolic function. Note that the FAST+SPAMM curve was truncated to the first 500 ms of the cardiac cycle due to tag fading.

Statistical Analysis

Linear regression analysis with a forced zero intercept and calculation of Pearson's correlation coefficient (r) were performed to compare FAST+CSPAMM to FAST+SPAMM for healthy subject twist, torsion, and twist rate for the first 500ms of the cardiac cycle (before SPAMM tag motion becomes undetectable due to tag fading). Peak systolic twist and torsion, and peak twisting and untwisting rates were compared using the Wilcoxon signed-rank test for paired non-parametric samples as well as with a paired t-test with Bonferroni post-hoc correction for multiple comparisons. A $p<0.01$ was considered statistically significant after the post-hoc correction. Additionally, a paired t-test was used to compare FAST+CSPAMM and FAST+SPAMM twist, torsion, and twist rate values for first 500ms of the cardiac cycle and data de-correlation using a decimation interval equivalent to the first zero crossing of the autocorrelation (autocorrelation length of 3.7±0.6 cardiac phases) of the respective curves. A Bland-Altman analysis for the first 500ms of the cardiac cycle was performed to compare twist and torsion values measured using FAST+CSPAMM and FAST+SPAMM. The 95% confidence intervals were determined by ranking the biases (FAST+CSPAMM-FAST+SPAMM) from smallest to largest and finding the data points located greater than or equal to 2.5% and less than or equal to 97.5% of the total data. Peak data values are reported as mean ± one standard deviation with the inter-subject range of values in parenthesis when applicable.

RESULTS

There was no significant difference for measures of peak twist derived from FAST+CSPAMM and FAST+SPAMM (13.5±2.7° [6.3° to 17.4°] vs. 11.9±4.0° [4.6° to 16.1°], P=0.03). Mean peak torsion derived from FAST+CSPAMM and FAST+SPAMM was 3.4±0.8°/cm [2.1°/cm to 4.9°/cm] vs. 2.9±1.0°/cm [1.5°/cm to 4.7°/cm] P=0.02. Mean peak twist rates (Figure 2) derived from FAST+CSPAMM and FAST+SPAMM were 76.8±22.2°/s

[32.4°/s to 118.7°/s] and 68.2±23.4°/s [24.6°/s to 99.8°/s], P=0.3. Mean peak untwist rate (Figure 2) from FAST+CSPAMM and FAST+SPAMM was -102.7±24.6°/s [-60.9°/s to -147.5°/s] vs. -106.6±32.4°/s [-55.7°/s to -171.2°/s], P=0.6. Mean peak normalized untwist rate derived from FAST+CSPAMM and FAST+SPAMM was -7.9±2.2/s [-4.7/s to -12.1/s] vs. -9.9±4.4/s [-5.1/s to -22.4/s], P=0.04. The Wilcoxon signed rank test did not reveal any significant differences for the peak values stated above, all P>0.01. The mean time to peak twist was 279±23ms and 293±25ms for FAST+CSPAMM and FAST+SPAMM respectively. The mean duration of untwisting was 148±21ms measured with FAST+CSPAMM. The mean ratio of rapid untwist to peak twist was 0.8±0.3 measured with FAST+CSPAMM. Both the duration of untwisting and rapid untwist could not be accurately measured with FAST+SPAMM due to tag fading. Rapid untwist is one of the components of the ratio of rapid untwist to peak twist, thus this ratio cannot be measured with FAST+SPAMM either. The average of the peak values and timings for the basal and apical slice locations are summarized in Table 1.

	FAST+CSPAMM	**FAST+SPAMM**	**P-value**
Peak systolic rotation (base) [deg]	-3.0±3.0	-2.9±3.1	0.8
Time of peak [ms]	357.6±34.5	393.4±96.6	0.1
Peak diastolic rotation rate (base) [deg]	62.5±34.3	55.5±39.9	0.5
Time of peak [ms]	470.3 ±68.7	474.6 ±84.8	0.8
Peak systolic rotation (apex) [deg]	11.2±3.9	9.3±2.8	0.02
Time of peak [ms]	291.9±59.3	301.7±78.3	0.2
Peak diastolic rotation rate (apex) [deg/s]	-74.2±29.5	-69.0±34.4	0.4
Time of peak [ms]	417.1±33.7	417.7±76.6	0.98

Table 1. Summary of mean peak values and timings for the basal and apical slices.

Bland-Altman analysis for the first 500ms of the cardiac cycle compares FAST+CSPAMM twist and torsion data to the FAST+SPAMM data (Figure 4). There is good agreement between CSPAMM and SPAMM for calculating LV twist and torsion with a bias of 1.1° and 95% confidence intervals of [-3.3°, 5.2°] and a bias of 0.3°/cm and 95% confidence intervals of [-0.9°/cm, 1.4°/cm] respectively. Bland-Altman analysis for twist rate provided a bias of -0.7°/s and a 95% confidence intervals of [-55.4°/s, 57.5°/s].

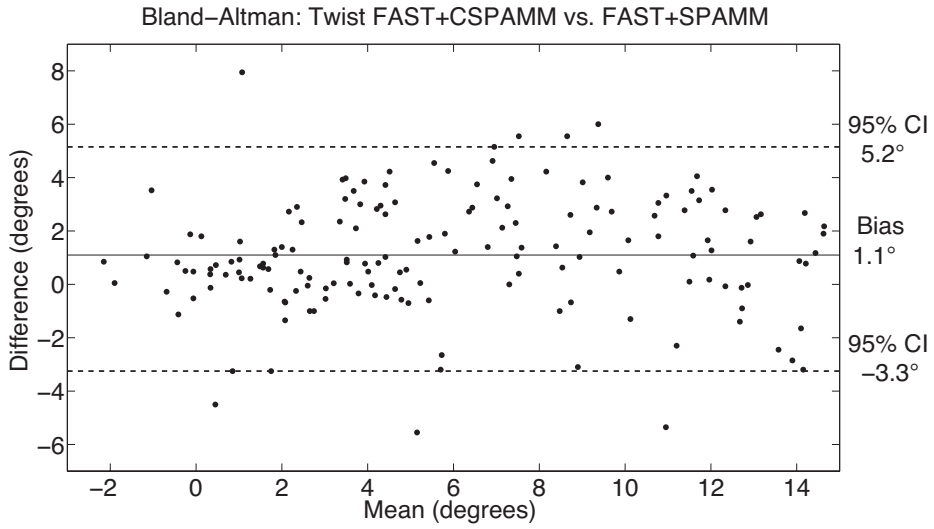


Figure 4: Bland-Altman analysis of LV twist estimates from FAST+CSPAMM compared to FAST+SPAMM indicates good agreement. The comparison of LV twist measures has a bias of 1.1° and a variance of (-3.3°, 5.2°).

Linear regression analysis for the first 500ms of the cardiac cycle using the FAST+CSPAMM and FAST+SPAMM data yielded a Pearson's correlation coefficients of r=0.88 and the equation CSPAMM=1.1*SPAMM for the twist results and r=0.88 and the equation CSPAMM=1.1*SPAMM for the torsion results, respectively. Linear regression

analysis of twist rate, which includes twisting and untwisting, provided r=0.85 and the equation CSPAMM= 0.9*SPAMM. The paired t-test of all of the decimated data for the twist, torsion, and twist rate did not reveal any significant differences between FAST+CSPAMM and FAST+SPAMM, P>0.01. However, comparison of the decimated data for twist and torsion from FAST+CSPAMM (with the updates of blood pool nulling and estimates of the first frame rotation) to FAST+SPAMM (without these updates) revealed significant differences, P<0.002. Twist rate derived from the decimated data from FAST+CSPAMM with updates and FAST+SPAMM without updates did not reveal any significant differences, P>0.01.

The average user interaction time for the FAST method was 2.6±0.3 minutes. This time includes study selection and contouring of the epicardium and endocardium for the basal and apical slices for both horizontal and vertical tags. The average post processing computational time of four series of tagged images was approximately 21 minutes performed on a MacBook Pro with a 2.4 GHz Intel Core 2 Duo processor.

DISCUSSION

FAST+CSPAMM is a semi-automated method that provides a quick and quantitative assessment of LV systolic and diastolic twist and torsion. From the LV twist curve calculation of torsion, twisting rate, untwisting rate, normalized untwisting rate, and time to peak twist is automatic. In Fourier space, where FAST image processing occurs, CSPAMM provides more easily detectable peaks (stimulated echoes and stimulated anti-echoes) later into the cardiac cycle. Therefore, FAST+CSPAMM provides a means for calculating additional diastolic functional parameters compared to FAST+SPAMM. For example, complete early diastolic untwisting can be observed, which allows the calculation of the duration of untwisting and the ratio of rapid untwist to peak twist, which may be important quantitative metrics of diastolic dysfunction.

Accurate measurement of early systolic twist is of particular importance to FAST processing because inter-frame rotation is calculated cumulatively and errors can propagate from the first frame to every subsequent frame. For this reason, blood pool nulling in the first three frames and estimating the first frame rotation had a significant impact on FAST measurements of twist, as demonstrated by paired t-test results. Nulling the blood pool in the first three frames removes the impact of coherent tags in the blood pool on twist measurements. The previous FAST method assumed that the first acquired image frame did not rotate, however, this did not account for possible delays between the ECG signal and the MRI tagging preparation being played or the low temporal resolution of the MRI scan. Incorporating these two updates to the FAST image processing makes the technique more accurate at measuring systolic and diastolic twist.

Bland-Altman results show a good agreement between FAST+CSPAMM and FAST+SPAMM and there were no statistical differences between the two methods for the first 500 ms of the cardiac cycle. These results indicate that for systole and early diastole FAST+CSPAMM and FAST+SPAMM yield equivalent results as expected. The values of peak twist, peak torsion, peak twisting rate and peak untwisting rate matched well with literature values of 12.7±1.7°(57), 1.9±0.3°/cm(57), 85.9±28.6°/s (58),-114.6±40.1°/s (58), respectively. However, peak twist values demonstrate a range in the literature, which may arise from differences in the selection of the apical and basal slice location(59), age(26), and level of physical activity (60). When comparing to literature values, one potential limitation of this study was the range of age and physical activity within the volunteer population. It has been shown that LV twist is dependent on age(26, 51), stress at the time of the exam(58) and amount of daily exercise(60). The age of study population varied from 23 to 64 years old, which may lead to variation associated with mean peak twist, torsion, and diastolic untwisting rate when compared with literature values. Some of the volunteers have highly active lifestyles while others were significantly less active.

Additionally, exercise performed during twist measurement has been shown to increase twist and untwisting velocity significantly(58, 61). The multiple ~20 second breath holds performed during this study may have transiently altered cardiac function for some volunteers, which may be associated with some of the variability between the SPAMM and CSPAMM comparisons.

The continued tag contrast during diastole that FAST+CSPAMM provides, enables quantification of diastolic untwisting information that FAST+SPAMM does not. However, the additional contrast derived from the subtraction of two complementary tagged sets of cine images (CSPAMM) results in approximately double the breath-hold duration of one SPAMM tagged set of cine images. Alternatively, FAST+SPAMM performed at 3.0T could also enable quantification of diastolic untwisting information. Since, breath-hold durations are often a clinically limiting factor, FAST+SPAMM at 3.0T would provide diastolic coverage at approximately half the breath-hold duration of FAST+CSPAMM at 1.5T.

FAST+CSPAMM requires a short exam time and provides a quick and quantitative assessment of systolic and diastolic left ventricular twist, torsion, twisting rates, time to peak twist, duration of untwisting, and the ratio of rapid untwist to peak twist. When FAST is used in conjunction with CSPAMM diastolic ventricular function can be quickly quantified, thereby providing further insight into left ventricular diastolic dysfunction within an acceptable breath hold time.

CHAPTER 5

Off-Resonance Insensitive Complementary SPAtial Modulation of Magnetization (ORI-CSPAMM) for Quantification of Left Ventricular Twist[3]

INTRODUCTION

In general, off-resonance due to field inhomogeneity, susceptibility and chemical shift leads to unwanted signal characteristics. In quantitative motion encoding sequences and measurements derived from them such as SPAMM tagging(5), DENSE(49), HARP(35), FAST(56), and phase contrast(62), off-resonance can lead to perturbations of the tagging pattern or inaccuracies in the signal phase estimates. Left ventricular (LV) twist can been measured from rotating tagging patterns, but can suffer inaccuracies as a consequence of off-resonance derived perturbations of the tagging pattern. Minimizing the effects of off-resonance is important to eliminating systematic and quantitative measurement errors.

Fahmy et al. (63) used the off-resonance of fat and a uniquely modified Complimentary SPatial Modulation of Magnetization (CSPAMM) encoding method to cancel the fat signal in each cardiac phase. The modifications to the CSPAMM sequence included: 1) an inversion of the tagging gradient used during the second SPAMM measurement, which reverses the position of the stimulated echo and stimulated anti-echo in k-space; and 2) prolonging the tag encoding duration so that the phase of chemically shifted fat is 90° relative to on-resonance water, which results in cancellation of the fat signal after image subtraction. The combination of these modifications leads to suppression of the fat signal in each CPSAMM tagged image. The second modification, however, only works precisely for a single isochromat (3.5ppm shift in their case). In addition, at higher field strengths the duration of the motion encoding gradient needed to cancel the fat signal may be too short to allow the tagging gradient to be played, especially for closely spaced tags.

[3] This work has been submitted for publication to the Journal of Magnetic Resonance Imaging.

Herein, we propose an alternative modification to the CSPAMM sequence that compensates for all forms of off-resonance and requires no a priori knowledge of the chemically shifted isochromat to be corrected. Hence the proposed solution is independent of the frequency spectrum of off-resonant moieties and of main-field strength.

The improved tagging contrast generated by CSPAMM(6) compared with SPAMM is the result of RF phase cycling the second tagging pulse by 180° and subtracting the phase cycled images from each other, which effectively cancels the relaxed component of the magnetization from the tagging information. Off-resonance phase accumulation occurs during both motion encoding (tagging gradients and RF pulses) and during imaging. Off-Resonant Insensitive- CSPAMM (ORI-CSPAMM) is a tagging pulse sequence that corrects off-resonance accrued during tagging preparation and readout and visibly removes chemical shift from the tagging pattern, which confers greater robustness to the derived quantitative measures.

In this study we seek to evaluate ORI-CSPAMM and Fourier Analysis of STimulated echoes (FAST) for the quantification of LV systolic and diastolic function and compare it to the previously validated FAST+SPAMM technique. In order to evaluate the quantitative ability of FAST+ORI-CSPAMM a comparison between a known and validated standard (FAST+SPAMM in normal subjects) is demonstrated.

Theory

Off-Resonance During Motion Encoding

Figure 1A shows the pulse sequence timing diagram for the two conventional 1-1 SPAMM experiments used to generate CSPAMM(6) tagging contrast. If the initially available longitudinal magnetization is denoted by M_z^0, then the state of the magnetization immediately after the first 90° RF-pulse is:

$$\vec{M} = \begin{bmatrix} M_z^0 \sin(\theta) \\ M_z^0 \cos(\theta) \\ 0 \end{bmatrix} = \begin{bmatrix} 0 \\ M_z^0 \\ 0 \end{bmatrix} \quad [1]$$

Where, θ in general, denotes the phase of the RF pulse (0° RF phase indicates rotation about the +x-axis and 90° is phased about the +y-axis) and θ=0°, in particular.

In general, the phase ξ accumulated by an isochromat in the rotating coordinate frame at position $\vec{r}$ in the presence of both a magnetic field gradient $\vec{G}$ and an off-resonant field B_{Off} is:

$$\xi(\vec{r}) = \gamma\left(\int_0^{\delta} (\vec{G}(t)\cdot \vec{r} + B_{Off}(\vec{r}))dt\right) \quad [2]$$

Where γ is the gyromagnetic ratio for hydrogen nuclei and δ is the duration of the gradient. If the spins are stationary during the time of integration δ and the off-resonance field is stable in time, then

$$\xi(\vec{r}) = \gamma\left(\vec{M}_0\cdot \vec{r} + B_{Off}(\vec{r})\cdot \delta\right) \quad [3]$$

This equation indicates that the phase of the isochromats will be spatially dependent (first term of Eqn. 3) with a spatial shift (second term of Eqn. 3) that depends on the magnitude of the off-resonance field at position $\vec{r}$. Therefore, the magnetization after the motion encoding gradient can be described as:

$$\vec{M} = \begin{bmatrix} -M_z^0 \sin(\xi(\vec{r})) \\ M_z^0 \cos(\xi(\vec{r})) \\ 0 \end{bmatrix} \quad [4]$$

Consequently, in the presence of off-resonance the tagging pattern induced by the applied gradient will be spatially shifted within off-resonant tissues such as fat relative to on-

resonance water. Herein, we ignore wavelength changes as a consequence of the chemical shift frequency offset.

Despite the short motion encoding intervals that are achievable with the best available gradient hardware the off-resonance term can produce noticeable spatial shifts of the tags. For example, a triangular tagging gradient using a duration of 1 ms and a maximum gradient amplitude of 4.8 mT/m, which produces a tag spacing of 10mm, will have tags in fat shifted by ~2mm relative to tissue tags, if fat is 3.3ppm off-resonant from water at 1.5T. The shift is ~2x larger at 3T.

The off-resonance effects during motion encoding can be refocused by splitting the motion encoding gradient in half, inserting a hard refocusing pulse, and inverting the second-half of the motion encoding gradient (Fig. 1B). The accumulated signal phase immediately before the refocusing pulse is:

$$\xi_1(\vec{r}) = \gamma\left(\frac{\vec{M}_0}{2}\cdot \vec{r} + B_{Off}(\vec{r})\cdot \delta\right) \qquad [5]$$

After the application of the refocusing pulse the sign of Equation 5 changes. The phase accumulated during the interval after the refocusing pulse is:

$$\xi_2(\vec{r}) = \gamma\left(-\frac{\vec{M}_0}{2}\cdot \vec{r} + B_{Off}(\vec{r})\cdot \delta\right) \qquad [6]$$

Therefore, the cumulative phase after the spilt refocused motion encoding gradient is insensitive to off-resonance:

$$\xi(\vec{r}) = \xi_1(\vec{r}) + \xi_2(\vec{r}) = -\gamma(\vec{M}_0\cdot \vec{r}) \qquad [7]$$

Therefore, the magnetization after the tagging preparation can be described as:

$$\vec{M} = \begin{bmatrix} -M_z^0 \sin(\xi_1(\vec{r}) + \xi_2(\vec{r})) \\ M_z^0 \cos(\xi_1(\vec{r}) + \xi_2(\vec{r})) \\ 0 \end{bmatrix} = \begin{bmatrix} M_z^0 \sin(\gamma(\vec{M}_0\cdot \vec{r})) \\ M_z^0 \cos(\gamma(\vec{M}_0\cdot \vec{r})) \\ 0 \end{bmatrix} \qquad [8]$$

Hence, the off-resonance effects during the interval of motion encoding are fully compensated.

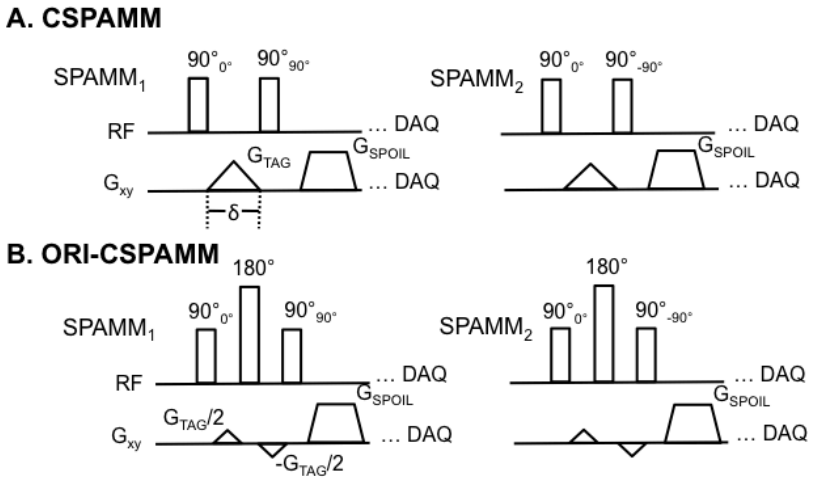


Figure 1. The conventional CSPAMM pulse sequence diagram (A) illustrates the phase-cycling used to create the complementary tagging pattern. The Off-Resonance Insensitive CSPAMM (ORI-CSPAMM) pulse sequence diagram (B) depicts the two phase-cycling loops ($SPAMM_1$ and $SPAMM_2$) and the tagging gradient, which has been divided and the 180° refocusing RF pulse, which has been added in order to correct for off-resonance effects that accrue during motion encoding.

Off-Resonance During Imaging

Signal phase accumulates during the interval of the readout gradient as a consequence of both the applied gradient and off-resonance. The off-resonance shift in the tagging pattern due to the phase accumulated during the readout gradient interval can be written as

$$\Delta\varphi_{RO} = \frac{\Delta f}{BW} \qquad [9]$$

where Δf is the frequency shift [Hz] between fat and water and BW is the readout gradient bandwidth [Hz/pixel].

During the first motion encoding experiment ($M_{SPAMM,1}$) the phase of the second RF pulse is incremented (θ=90°) and, subsequent to spoiling, the magnetization can be written in terms of the sinusoidal tagging pattern and the off-resonance shift during the readout gradient as,

$$M_{SPAMM,1} = M_z^0 \sin(\gamma(\vec{M}_0 \cdot \vec{r}) + \Delta\varphi_{RO}) \sin(\alpha) \quad [10]$$

where α is the RF imaging flip angle. During the second motion encoding experiment ($M_{SPAMM,2}$) the phase of the second RF is cycled to θ=-90° and the magnetization after the second phase-cycling step can be written as

$$M_{SPAMM,2} = M_z^0 \sin(-\gamma(\vec{M}_0 \cdot \vec{r}) + \Delta\varphi_{RO}) \sin(\alpha) \quad [11]$$

The CSPAMM tagging pattern is generated by the difference between the two phase-cycling loops, where the off-resonance term can be isolated from the spatially dependent tagging pattern term:

$$M_{ORI-CSPAMM} = M_{SPAMM,2} - M_{SPAMM,1}$$

$$= [M_z^0 \sin(-\gamma(\vec{M}_0 \cdot \vec{r}) + \Delta\varphi_{RO}) - M_z^0 \sin(\gamma(\vec{M}_0 \cdot \vec{r}) + \Delta\varphi_{RO})] \cdot \sin(\alpha) \quad [12]$$

After applying the product-to-sum trigonometric identities for sine and cosine, equation 12 can be simplified to:

$$M_{ORI-CSPAMM} = -2M_z^0 \sin(\gamma(\vec{M}_0 \cdot \vec{r})) \cos(\Delta\varphi_{RO}) \sin(\alpha) \quad [13]$$

Thus, the phase of the tagging pattern is unaffected by off-resonance. However, the intensity of the tagged image will be diminished by the readout off-resonance term ($\cos\Delta\varphi_{RO}$).

MATERIALS AND METHODS

Healthy Subjects MRI Protocol

Healthy human subjects (n=13) with no history of cardiovascular or respiratory disease were studied (3 female, mean age of 32.5±11.2 years, weight 70.5±12.7 kg, height 1.7±0.1

m, heart rate 54.8±9.2 beats/min). The local institutional review board approved this study and all subjects provided written informed consent.

ECG triggered images were acquired at end-expiration with subjects placed in the head-first supine position. All images were acquired with a Siemens Avanto 1.5T scanner (Siemens Healthcare, Erlangen, Germany) and a six element body matrix coil in combination with a six element spine matrix. Axial, coronal, and sagittal orientation scout images were used to plan the study. Balanced steady-state free precession cine images were acquired using a 6 mm slice thickness and a 66% gap between slices, in parallel left ventricular (LV) short-axis planes and used to select basal and apical slices for acquisition of tagged images. The most apical slice containing the presence of the blood pool throughout the entire cardiac cycle and the most basal slice in which the LV myocardium maintained a continuous annular shape during the entire cardiac cycle were used to prescribe the two slices for tagging and subsequent image processing.

A cardiac gated spoiled gradient echo sequence was modified to support both 1-1 binomially weighted SPAMM line tags and 1-1 binomially weighted ORI-CSPAMM line tags (both with a total tagging flip angle of 180°). These sequences were used to acquire short-axis images at the base and apex of the LV with the following parameters: 360-300x300-280mm field-of-view, 5-6mm slice thickness, 192x144 acquisition matrix, 501 Hz/pixel receiver bandwidth, TE/TR = 3.5-3.7/4.7-6.5 ms, 7-8 VPS, 10 mm tag spacing, and 14-16 cardiac phases. The breath hold duration for each sequence were 21 and 22 heart beats respectively (19.6 ± 4.1 seconds depending upon heart rate), for SPAMM and ORI-CSPAMM respectively. The SPAMM data was acquired using two averages to maintain comparable SNR. The ORI-CSPAMM data was acquired without averaging, but required acquisition of two image sets with 180° RF phase cycling of the second tagging RF pulse. Additionally, a 15° imaging flip angle was used to acquire SPAMM images, while a non-linearly ramped flip angle (final 22°) was used to acquire ORI-CSPAMM images(7). Cine

tagged images were acquired using both horizontal and vertical tagging in separate breath holds.

Fourier Analysis of STimulated echoes (FAST)

Manual contouring of the LV epicardium at an end-systolic frame and the endocardium in an early systolic frame was performed for both the apical and basal slices. The FAST(56)method utilizes the fact that rotation in image space corresponds to rotation in Fourier space. Subsequent to manual contouring, the FAST method performed least squares fitting of an ellipse to the respective LV boundary. The long and short axes of the ellipses were used to define a 2D Butterworth mask that isolates the region of interest (LV) in all cardiac frames and suppressed the blood pool in the first three cardiac frames. Later in the cardiac cycle tags in the blood pool dissipate making the endocardial filter unnecessary. The segmented image was then Fourier transformed after which the free induction decay was nulled with a circular mask and the Fourier image was cropped to the central 64 lines in k-space, leaving only the stimulated echo and anti-echo, which rotate in Fourier space. The final step of the FAST algorithm involved 2D cross-correlation in Fourier space with the subsequent cardiac frame in order to estimate the inter-frame rotation. Inter-frame rotations are calculated for all cardiac frames, from which values of LV twist were derived.

To determine rotation in the first cardiac frame the image is processed twice. First, the frame is processed identically to the method described above. Second, a copy of the first frame is made, segmented with the above-described Butterworth mask, and subsequently Fourier transformed. The copied first frame was then reflected about the axis perpendicular to the tagging lines, the FID was nulled, and the reflected image was cropped as described above. Finally, the reflected version of the first cardiac frame was 2D cross-correlated with

the original segmented, nulled, and cropped first cardiac frame to estimate the first frame's rotation.

LV twist was calculated as the difference between the apical angle of rotation and basal angle of rotation for matching temporal frames with units of degrees (deg). Peak twist was identified as the maximum twist value for each subject. LV torsion was defined as LV twist divided by the distance between the apical and basal slices with units of deg/cm. Peak torsion was identified as the maximum torsion value for each subject. The circumferential-longitudinal shear-angle (CL-shear angle) was defined as(64):

$$CL - Shear = \frac{\phi_{apex}\rho_{apex} - \phi_{base}\rho_{base}}{D}$$

where ϕ is rotation of the apex or base in degrees, ρ is the epicardial radius of the apex or base in mm, and D is the distance between the apex and base in mm. Peak CL-shear angle was identified as the maximum CL-shear angle for each subject. Twist rate was calculated as the temporal discrete derivative of twist with units of deg/s. Peak twist rate was identified as the maximum twist rate, while peak diastolic untwist rate was identified as the minimum twist rate. Normalized peak untwist rate was calculated as the minimum twist rate divided by the maximum twist angle with units of s^{-1}.

Data Processing

The FAST+ORI-CSPAMM and FAST+SPAMM estimates of rotation were used for statistical analysis of peak twist, torsion, twist rate, and untwist rate, mean peak values and timings for the apical and basal slices, and time of peak twist. The duration of untwisting was determined from twist data interpolated with a cubic smoothing spline to 1% increments of the cardiac cycle. This smoothing reduced noise and allowed for better detection of the end of untwisting, the maximum of the second derivative of the twist after peak systolic twist. The end of rapid untwisting was used to estimate the ratio of rapid untwisting to peak twist.

Atrial systole completes the process of untwisting in healthy hearts. The ratio of rapid untwisting to peak twist provides insight into the contribution of atrial systole to the completion of the untwisting process. Additionally, tag motion becomes undetectable due to tag fading in SPAMM images, as a result all SPAMM data was truncated to the first 500 ms of the cardiac cycle.

Figure 2 depicts the systolic and diastolic measures of twist calculated with FAST+ORI-CSPAMM and FAST+SPAMM. Peak systolic twist, systolic twist rates, and early diastolic untwisting are clearly visible for both FAST+ORI-CSPAMM and FAST+SPAMM results (Figure 2). FAST+ORI-CSPAMM results, however, also clearly show the end of diastolic untwisting and continue into mid-diastasis. Figure 2 shows incomplete diastolic untwisting in the case of SPAMM because the tags have faded too much for quantitative analysis.

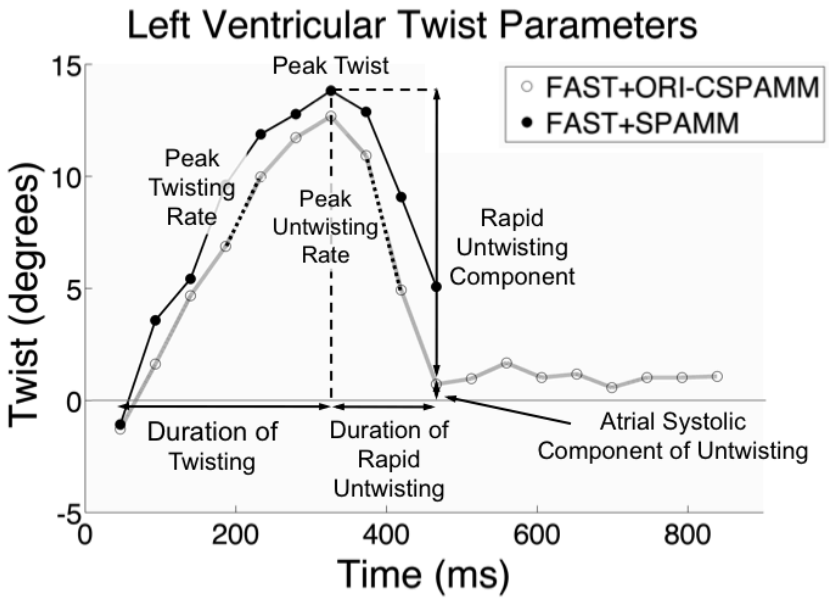


Figure 2. LV twist parameters that are enabled by FAST+SPAMM and FAST+ORI-CSPAMM include peak twist, peak twisting rate, peak untwisting rate, duration of twisting, duration of rapid untwisting, and the ratio of rapid untwisting to peak twist, which gives

insight into the atrial systolic component of untwisting. Note that the FAST+SPAMM curve was truncated to the first 500 ms of the cardiac cycle due to tag fading.

Statistical Analysis

Comparisons between FAST+ORI-CSPAMM and FAST+SPAMM were only performed for the first 500ms of the cardiac cycle due to tag fading in the SPAMM images. Linear regression analysis with a forced zero intercept and calculation of Pearson's correlation coefficient (r) were performed to compare FAST+ORI-CSPAMM to FAST+SPAMM for healthy subject twist, torsion, and twist rate. The Wilcoxon signed-rank test for paired non-parametric samples, as well as, paired t-test with Bonferroni post-hoc correction for multiple comparisons were used to compare peak systolic twist, torsion, and CL-shear angle, as well as, peak twisting and untwisting rates. A $p<0.01$ was considered statistically significant after the post-hoc correction. Additionally, a paired t-test was used to compare FAST+ORI-CSPAMM and FAST+SPAMM twist, torsion, and twist rate values for first 500ms of the cardiac cycle after data de-correlation using a decimation interval equivalent to the first zero crossing of the autocorrelation (autocorrelation length of 3.4±0.4 cardiac phases) of the respective curves. A Bland-Altman analysis was performed to compare peak twist and torsion values measured using FAST+ORI-CSPAMM and FAST+SPAMM. Due to small sample size, the 95% confidence intervals were determined by bootstrapping, sampling with replacement, the median of the biases (FAST+ORI-CSPAMM minus FAST+SPAMM) 10000 times. The Bland-Altman bias is reported as the median of the biases. Peak data values were reported as mean ± one standard deviation with the inter-subject range of values in parenthesis when applicable.

RESULTS

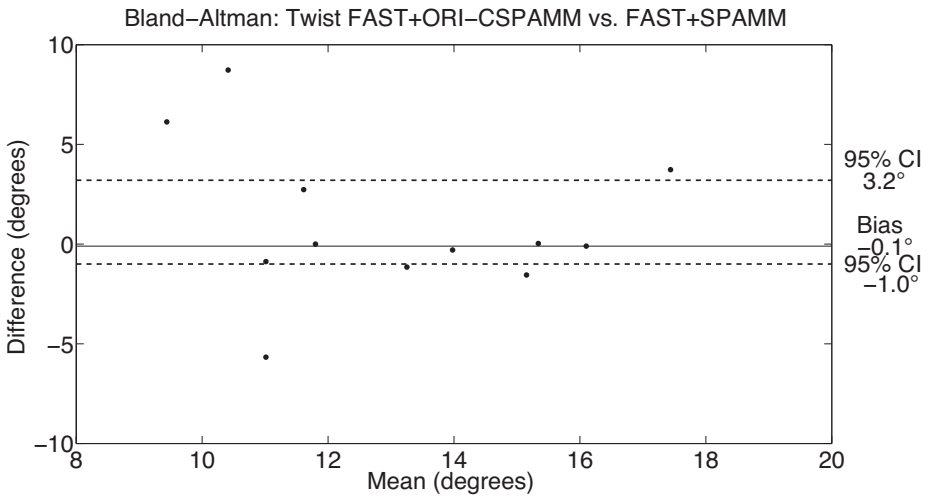
There was no significant difference for measures of peak twist derived from FAST+ORI-CSPAMM and FAST+SPAMM in normal subjects (12.9±2.7° vs. 11.9±4.0°, P=0.4). Mean peak torsion derived from FAST+ORI-CSPAMM and FAST+SPAMM were not significantly different (3.3±0.9°/cm vs. 2.9±1.0°/cm, P=0.3). Mean peak CL-shear angle derived from FAST+ORI-CSPAMM and FAST+SPAMM were not significantly different (9.1±3.0° vs. 8.2±3.4°, P=0.3). Mean peak twist rates derived from FAST+ORI-CSPAMM and FAST+SPAMM were 79.6±20.2°/s and 68.2±23.4°/s (P=0.1). Mean peak untwist rate from FAST+ORI-CSPAMM and FAST+SPAMM was -117.5±31.4°/s vs. -106.6±32.4°/s (P=0.3). Mean peak normalized untwist rate derived from FAST+ORI-CSPAMM and FAST+SPAMM was -9.3±2.0/s vs. -9.9±4.4/s (P=0.7). The Wilcoxon signed rank test did not reveal any significant differences for the peak values stated above (all P>0.01). The mean time to peak twist was 281±18ms and 293±25ms for FAST+ORI-CSPAMM and FAST+SPAMM respectively. The mean duration of untwisting was 148±21ms measured with FAST+ORI-CSPAMM. The mean ratio of rapid untwisting to peak twist ratio was 0.9±0.3 measured with FAST+ORI-CSPAMM. Both the duration of untwisting and the ratio of rapid untwisting to peak twist could not be accurately measured with FAST+SPAMM due to tag fading.

Bland-Altman analysis for peak FAST+ORI-CSPAMM twist and torsion data to the FAST+SPAMM data (Figure 3). There is good agreement between ORI-CSPAMM and SPAMM for calculating LV twist (bias of -0.1° and 95% confidence intervals of [-1.0°, 3.2°]) and torsion (bias of -0.01°/cm and 95% confidence intervals of [-0.3°/cm, 0.8°/cm]), respectively. Bland-Altman analysis for peak CL-shear angle had a bias of -0.3° and a 95% confidence interval of [-1.1°,2.3°]. Bland-Altman analysis for peak systolic twist rate and diastolic untwisting rate provided a bias of 18.8°/s and -24.51°/s a 95% confidence intervals of [-6.1°/s, 24.4°/s] and [-36.1°/s, 9.9°/s], respectively.

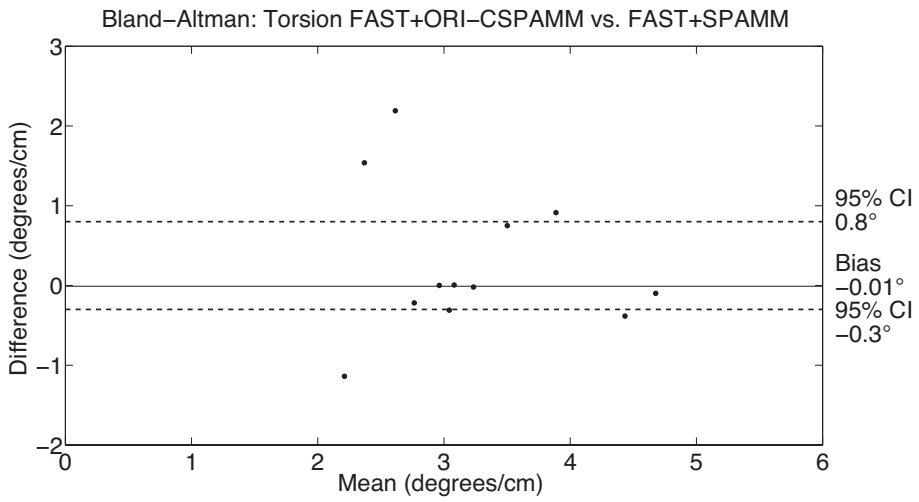
Linear regression analysis for the first 500ms of the cardiac cycle using the FAST+ORI-CSPAMM and FAST+SPAMM data yielded a Pearson's correlation coefficients of r=0.88

and the equation ORI-CSPAMM=1.1*SPAMM for the twist results and r=0.88 and the equation ORI-CSPAMM=1.1*SPAMM for the torsion results, respectively. Linear regression analysis of twist rate, which includes twisting and untwisting, provided r=0.85 and the equation ORI-CSPAMM= 0.9*SPAMM. The paired t-test of the decimated data for the twist, torsion, and twist rate curves did not reveal any significant differences between FAST+ORI-CSPAMM and FAST+SPAMM, P>0.8.

The average user interaction time for the FAST method was 2.6±0.3 minutes. This time includes study selection and contouring of the epicardium and endocardium for the basal and apical slices for both horizontal and vertical tags. The average post-processing computational time of four series of tagged images was approximately 21 minutes performed on a MacBook Pro with a 2.4 GHz Intel Core 2 Duo processor.



A.



B.

Figure 3. Bland-Altman analysis of LV twist estimates (A) from FAST+ORI-CSPAMM compared to FAST+SPAMM for the peak values indicates good agreement. The comparison of LV twist measures has a bias of -0.1° and a variance of (-1.0°, 3.2°). Bland-Altman analysis of LV torsion estimates (B) from FAST+ORI-CSPAMM compared to FAST+SPAMM for the peak values indicates good agreement. The comparison of LV torsion measures has a bias of -0.01° and a variance of (-0.3°, 0.8°).

Qualitative Image Assessment

The ORI-CSPAMM sequence removes the effects of chemical shift from the phase of the tagging pattern (Figure 4). In SPAMM (Figure 4B) the chemical shift in the tagging pattern arises as a function of the duration of the motion encoding gradient and the readout gradient. The shift in the periodicity of the tagging pattern is ~2.4 pixels between on-resonant and off-resonant tissue. ORI-CSPAMM images (Figure 4C) confirm the theory of the ORI alterations to the CSPAMM pulse sequence. Figure 4C, clearly illustrates that the chemical shift in the tagging pattern has been removed. This is apparent in both in the chest wall between subcutaneous fat and muscle and in the heart at the myocardial-epicardial fat boundary).

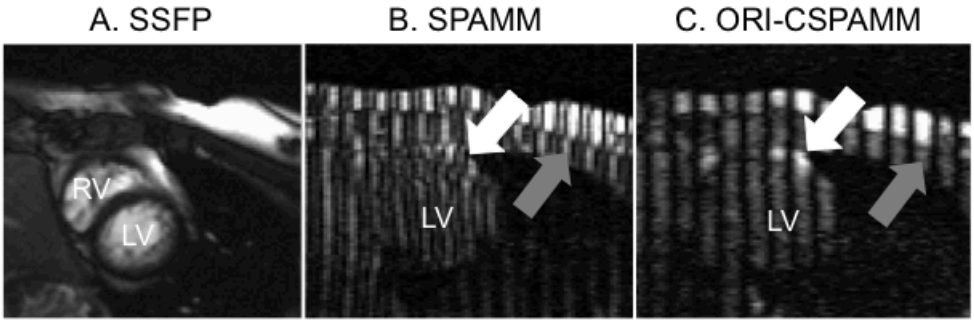


Figure 4. (A) SSFP reference image illustrating the LV an RV anatomy. (B) *In vivo* chemical shift is apparent between epicardial fat and myocardium (white arrow) and between chest wall fat and muscle (gray arrow) when using conventional 1-1 SPAMM tagging preparation. (C) *In vivo* ORI-CSPAMM tag preparation, where chemical shift induced tagging pattern displacement is no longer visible due to the additional refocusing RF pulse.

DISCUSSION

FAST+ORI-CSPAMM provide an automated method for the quantitative assessment of LV systolic and diastolic twist, torsion, twisting rate, untwisting rate, normalized untwisting rate, and time to peak twist subsequent that is insensitive to off-resonance. Unlike the fat suppression CSPAMM sequence proposed by Fahmy et al (63), ORI-CSPAMM corrects for all forms of off-resonance not just for fat. In Fourier space, where FAST image processing occurs, ORI-CSPAMM provides more easily detectable peaks (stimulated echoes and stimulated anti-echoes) later into the cardiac cycle than FAST+SPAMM, which allows reliable access to complete early diastolic untwisting.

In the healthy heart, epicardial fat is a primary source of off-resonant tissue. It should, however, lie outside the region of interest used for FAST twist calculations. Thus, no significant differences between FAST twist measurements made with the ORI-CSPAMM and SPAMM were detected in this work. Nevertheless, there is a trend to higher reported

systolic twist related parameters when using ORI-CSPAMM, which is consistent with the expectation from theory. For example, when contouring inadvertently includes epicardial fat in the analysis, then rotation estimates will be underestimated unless ORI-CSPAMM is being used. Similarly, in patient populations with fatty infiltration of the LV(65, 66), FAST+ORI-CSPAMM maybe particularly useful in providing accurate twist measurements.

Bland-Altman results show a good agreement between FAST+ORI-CSPAMM and FAST+SPAMM and there were no statistical differences between the two methods for the first 500 ms of the cardiac cycle. These results indicate that for systole and early diastole FAST+ORI-CSPAMM and FAST+SPAMM yield nearly equivalent results as expected. The values of peak twist, peak torsion, peak twisting rate and peak untwisting rate matched well with literature values of 12.7±1.7°(57), 1.9±0.3°/cm(57), 85.9±28.6°/s (58),-114.6±40.1°/s (58), respectively. However, the value of peak CL-shear angle differed slightly from previously reported values 7.7±1.2°(67). The difference between the value reported in this study and that of the literature may be due to the selection of a more basal apical slice in this study. This selection of apical slice location leads to a larger apical epicardial radius and a smaller distance between the slice, which both contribute to the larger CL-shear angle value reported in this study. Shear-angle has been reported to be a more robust measure of rotational mechanics than twist or torsion, however, this may not be the case as demonstrated by the difference reported in this study compared with a typical literature value.

There are two important limitations to this study. First, clinical patients were not included in this study. To better understand how fatty infiltration affects twist measurements made from tagged MR images, a clinical study should be performed. Second, phase-cycling used to generate CSPAMM images leads to longer breath-hold durations when compared with SPAMM, making ORI-CSPAMM acquisitions challenging for patients with limited breath-hold capabilities. These, longer breath-holds may also contribute to changes in twist/torsion

between acquisitions, due to changes in loading conditions of the heart. Improvements in acquisition efficiency may be overcome with higher parallel imaging acceleration rates or the incorporation of prospective compressed sensing.

FAST+ORI-CSPAMM quickly and quantitatively calculates systolic and diastolic LV twist, torsion, CL-shear angle, twisting rates, time to peak twist, duration of untwisting, and the ratio of rapid untwisting to peak twist. ORI-CSPAMM corrects off-resonance accrued during tagging preparation and readout and visibly removes chemical shift from the tagging pattern, which confers greater robustness to the derived quantitative measures.

CHAPTER 6

Intra- and Inter-scan Reproducibility using Fourier Analysis of STimulated Echoes (FAST) for the Rapid and Robust Quantification of Left Ventricular Twist[4]

INTRODUCTION

Assessing the reproducibility of new magnetic resonance imaging (MRI) biomarkers is an important part of validation. LV twist is the preferred nomenclature of the measurement defined as the difference in the rotation of the apex of relative to that of the base of the heart(68). Twist, according to this nomenclature, has been shown to increase in patients with aortic stenosis(27) and hypertrophic cardiomyopathy(32), and decrease in patients with transmural myocardial infarction(69) and dilated cardiomyopathy(31). As a result, LV twist has been proposed as a functional left ventricular imaging biomarker(21). When tracking changes in twist for longitudinal assessment of disease progression, the reproducibility of the measurement is an important consideration. High reproducibility (low variability) leads to greater confidence in the observed changes and to the requirement for smaller subject sample sizes in clinical trials. However, no intra- or inter-scan reproducibility studies of LV twist derived from tagged MRI have been performed.

Fourier Analysis of STimulated Echoes (FAST) is a new MRI tissue tagging method that has recently been shown to compare favorably to conventional estimates of left ventricular (LV) twist from cardiac tagged images, but with significantly reduced user interaction time(56). The purpose of this study was to assess the intra- and inter-scan reproducibility of LV twist as measured by FAST. Additionally, the reproducibility of CL-shear angle was investigated(64).

[4] This work has been submitted for publication to the Journal of Cardiovascular Magnetic Resonance Imaging.

MATERIALS AND METHODS

ORI-SPAMM Sequence

Off-resonance due to field inhomogeneity and chemical shift leads to unwanted signal characteristics, which can lead to inaccuracies in quantitative measures such as LV strain measured by DENSE(49) and rotation or the velocity of flowing blood measured by phase contrast(62). Off-Resonance Insensitive- SPAMM (ORI-SPAMM) was developed to negate the effects of off-resonance accrued during motion encoding. The original SPAMM(70) tagging preparation, Figure 1 A, is used to generate a sinusoidal tagging pattern that can be used to quantify rotation of the LV. The ORI-SPAMM prep, modifies the original SPAMM tagging prep to include a 180° refocusing pulse and a split motion encoding gradient, Figure 1B.

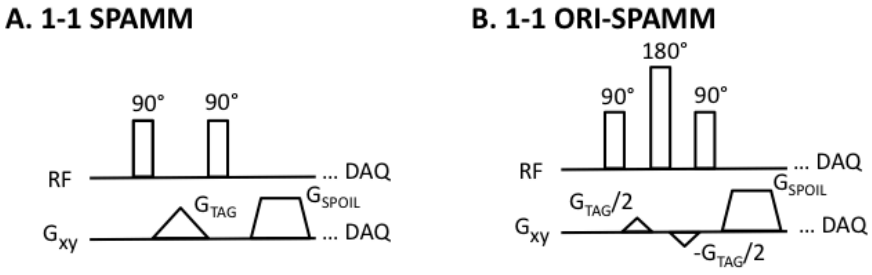


Figure 1. (A) A traditional binomially weighted 1-1 SPAMM tagging preparation is depicted for comparison with updated ORI-SPAMM tagging prep. (B) 1-1 ORI-SPAMM is depicted by the addition of a 180° refocusing RF pulse to the traditional 1-1 SPAMM tagging preparation, in order to correct for off-resonance effects that accrue during motion encoding. In addition, the tagging gradient has been split to minimize the duration of the tag preparation.

The theory behind these pulse sequence alterations has been previously presented as part of ORI-CSPAMM sequence(71). Recall, CSPAMM is related to SPAMM by phase-

cycling the second RF pulse during the tagging preparation by 180°, which leads to improved tagging contrast when the phase-cycled images are subtracted from each other(6). The Off-Resonance Insensitive augmentation of the sequence is comprised of a 180° refocusing pulse and a split motion encoding gradient, which effectively remove any off-resonance accrued during motion encoding. The primary difference between the ORI-CSPAMM and ORI-SPAMM sequences is that off-resonance accrued during readout is effectively removed from the CSPAMM tagging pattern when subtraction of the phase-cycled CSPAMM acquisitions occurs. This off-resonance is not removed from the ORI-SPAMM tagging pattern. However, the CSPAMM phase-cycling leads to long breath-hold times challenging the breath-hold capabilities of both pediatric and adult patients. ORI-SPAMM was developed as a short breath-hold sequence. When ORI-SPAMM is performed at 3.0T, rather than at 1.5T it offers better tag contrast through mid-diastole.

Healthy Subjects MRI Protocol

The local institutional review board approved this study and all subjects provided written informed consent. Eleven healthy human subjects with no history of cardiovascular or respiratory disease were included in the study. One subject was excluded due to sickness on the second day of scanning. The remaining 10 subjects were scanned twice (1 female, mean age of 27.9±4.1 years, weight 71.4±10.6 kg, height 1.8±0.1 m, heart rate 55.1±8.6 beats/min).

End expiration breath-held ECG triggered images were acquired for head-first supine subjects, scanned with a Siemens Trio 3.0T scanner (Siemens Healthcare, Erlangen, Germany) and a six element body matrix coil in combination with a six element spine matrix. Axial, coronal, and sagittal orientation scout images were used to plan the study. Balanced steady-state free precession (bSSFP) cine images were acquired using a 6 mm slice thickness and a 66% gap between slices, in parallel left ventricular (LV) short-axis planes

and used to select basal and apical slices for acquisition of tagged images. The criteria for selecting short axis slices from which twist measurements were derived was defined as follows: most apical slice containing the presence of the blood pool throughout the entire cardiac cycle and the most basal slice in which the LV myocardium maintained a continuous annular shape during the entire cardiac cycle. These bSSFP slices were used to prescribe the two slices for tagging and subsequent image processing.

A cardiac gated spoiled gradient echo sequence was modified to support 1-1 binomially weighted ORI-SPAMM line tags (both with a total tagging flip angle of 180°). This sequence was used to acquire short-axis images at the base and apex of the LV with the following parameters: 280-330x280-330mm field-of-view, 6mm slice thickness, 192x192 acquisition matrix, 395 Hz/pixel receiver bandwidth, TE/TR =2.33-2.39/4.71-4.83 ms, 8 VPS, 12° imaging flip angle, 8 mm tag spacing, i-pat acceleration factor 2 with 24 central lines, and 14-27 cardiac phases. The breath hold duration was 15 heart beats (12.5 ± 1.9 seconds) depending upon heart rate. Cine tagged images were acquired using both horizontal and vertical tagging in separate breath holds. Scans were performed at 3.0T to ensure tag contrast through mid-diastole.

Each subject was scanned twice with eight days between the scans. On Day-1 two measurements of LV twist were collected for intra-scan comparisons. On Day-8 one measurement of LV twist was collected for inter-scan comparisons. The acquisition order of the apex and base horizontally and vertically tagged slices was randomized to minimize ordering bias arising from heart rate changes due to multiple breath-holds from influencing twist measurements. The distance between apical and basal slices was kept constant between both days of scanning.

Fourier Analysis of STimulated echoes (FAST)

FAST(56) is a semi-automated image processing method designed to quantify LV rotation from tagged MR images. The only user interaction necessary is contouring of the epicardium and endocardium in an end-systolic cardiac frame and in an early systolic cardiac frame, respectively. The main principle of the FAST method is that rotation in image space has a one to one correspondence with rotation in Fourier space, but in Fourier space the tagging information is focused into stimulated echoes, which are easy to track. The user-defined contours are used to isolate the region of interest in the images (LV myocardium), then the images are Fourier transformed. The central peak in Fourier space is nulled and the image is subsequently cropped. Two-dimensional cross-correlation is used to determine rotation between cardiac frames, from which a cumulative rotation of the ventricle with respect to time is determined. This process is applied to images collected at both the apex and base of the heart, and the difference between the two rotations is defined as twist. The FAST method has been described in more detail and previously validated using both SPAMM and CSPAMM images in healthy volunteers(56, 72). Peak twist was defined as the maximum difference in rotation between the apex and the base.

The circumferential-longitudinal shear-angle (CL-shear angle) was defined as (64):

$$CL - Shear = \frac{\phi_{apex}\rho_{apex} - \phi_{base}\rho_{base}}{D}$$

where ϕ is rotation of the apex or base in degrees, ρ is the epicardial radius of the apex or base in mm, and D is the distance between the apex and base in mm. Peak CL-shear angle has been suggested to be a better measure of LV function compared to twist, due to its normalization for heart size and purported relative independence of the selection of imaging planes(68). Twist rate was defined as the discrete derivative of twist with respect to time with units of deg/s. Peak twist rate was defined as the maximum twist rate. Peak diastolic untwist rate was defined as the minimum twist rate.

Statistical Analysis

For each volunteer, the intra- and inter-scan reproducibilities of peak twist were assessed according to the following method. First, a paired t-test was used to test for the difference in peak twist between Day-1, Scan-1 and Day-1, Scan-2 (intra-scan) as well as between Day-1, Scan-1 and Day-8 (inter-scan). A $p<0.05$ was considered statistically significant.

Next, the concordance correlation coefficient (CCC), a measure which evaluates how close the data are to the line of identity, was used to determine agreement for the intra- and inter-scan peak twist. Lastly, Bland-Altman analysis(44) was used to compute the repeatability coefficient (RC), the range of the 95% confidence interval, for peak twist, which gives an indication of the variability of the measurement of peak twist. Bootstrapping, sampling with replacement (1000 times), was utilized to determine the RC and 95% confidence interval for the median of the difference of peak twist due to the limited sample size and non-Gaussian distribution. Bland-Altman bias is reported as the median of the difference in peak twist. Peak data values were reported as mean ± one standard deviation.

RESULTS

Image Quality

All of the data from all subjects over multiple days of scanning were qualitatively acceptable and routinely analyzable by FAST without issue. Figure 2 depicts an example of basal tagged images from a single normal subject acquired on Day-1 and Day-8. There is a good match between the basal slice levels from Day-1 to Day-8. Additionally, there is a noticeable loss of tissue to tag contrast in the diastolic images. However, since this scan was performed at 3T the tags are visible through mid-diastole.

Intra-scan Comparisons of LV Twist

Figure 3 illustrates the differences observed in mean twist as a function of frame number for the three separate scans. Mean twist from Day-8 deviates from the other scans starting at end-systole and maintains this deviation through diastole. Note that peak twist observed in these averaged curves is not the same as the average of the individual peaks (Table 1).

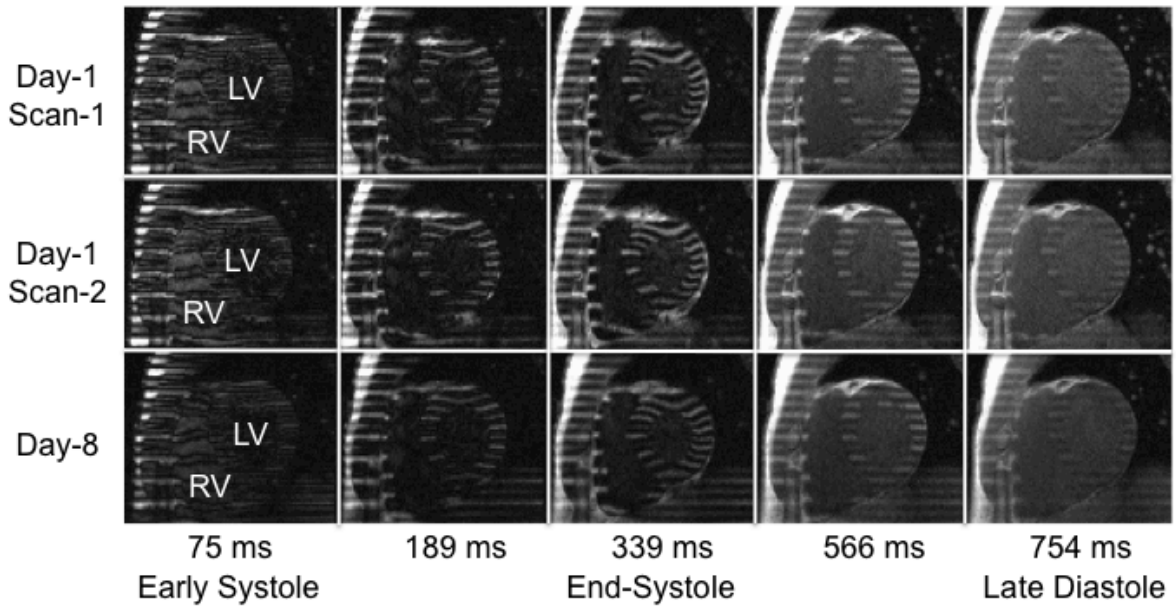


Figure 2. This figure represents a typical basal tagged slice acquired on Day-1 Scan -1, Day-2 Scan-2, and Day-8. The tissue to tag contrast fades with time, however, the tags are detectable at end-systole (339ms) through mid-diastole.

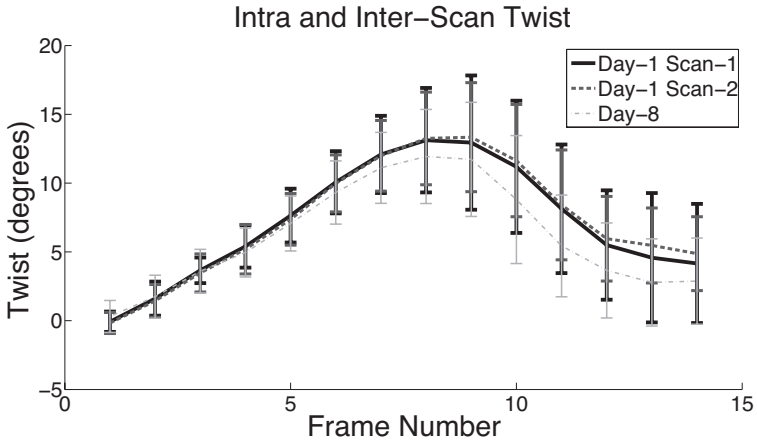


Figure 3. This figure demonstrates the high intra-scan and inter-scan reproducibility of mean LV twist as a function of frame number for Day-1 Scan-1, Day-1 Scan-2, and Day 8. Error bars represent ± 1 standard deviation.

Table 1.

	Mean Peak Twist [deg]	Mean Peak CL-Shear Angle [deg]	Mean Peak Twist Rate [deg/s]	Mean Peak Untwisting Rate [deg/s]	Bland-Altman Peak Twist Bias (95% CI)	RC Peak Twist	CCC Peak Twist	P-Value Peak Twist
Intra-Scan	13.4±4.3, 13.6±3.7	6.8±1.3, 6.8±1.3	80.3±11.8, 81.1±12.1	-105.3±21.2, -102.2±27.4	-0.6° [-1.0°, 1.6°]	2.6°	0.9	P=0.9
Inter-Scan	13.4±4.3, 13.0±2.7	6.8±1.3, 6.4±1.2	80.3±11.8, 71.2±15.4	-105.3±21.2, -106.7±23.6	1.4° [-1.0°, 3.0°]	4.0°	0.6	P=0.1

There were no intra-scan differences (Day-1, Scan-1 versus Day-1, Scan-2). Mean peak twist measurements were 13.4±4.3° (Day-1, Scan-1) and 13.6±3.7° (Day-1, Scan-2). Results are summarized in Table 1. Paired t-tests showed no significant differences in peak LV twist for intra-scan values (p=0.90). Bland-Altman analysis resulted in an intra-scan bias and 95%-CI of -0.6° [-1.0°, 1.6°] (Figure 4A). The intra-scan Bland-Altman RC for peak LV twist was 2.6°, showing excellent reproducibility between the two different scans. The intra-scan CCC was 0.9 indicating excellent peak twist agreement.

Mean peak systolic twist rates were 80.3±11.8°/s (Day-1, Scan-1) and 81.1±12.1°/s (Day-1, Scan-2) and the mean peak diastolic untwisting rates were -105.3±21.2°/s (Day-1, Scan-1) and -102.2±27.4°/s (Day-1, Scan-2), respectively. Bland-Altman analysis resulted in an intra-scan bias and 95%-CI of -1.3°/s [-5.3°/s, 3.9°/s] for systolic twist rate and 3.3°/s [-17.3°/s, 10.5°/s] for diastolic untwisting rate.

Inter-scan Comparisons of LV Twist

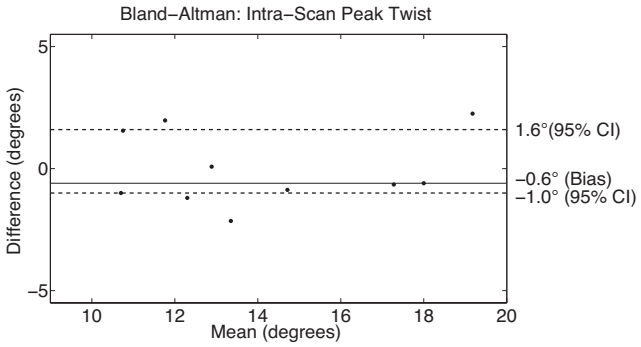
There was a trend indicating no inter-scan statistical differences (Day-1, Scan-1 versus Day-8). Mean peak twist measurements were 13.4±4.3° (Day-1, Scan-1) and 13.0±2.7° (Day-8). Paired t-tests showed no significant differences in peak LV twist for inter-scan values (p=0.11). Inter-scan Bland-Altman analysis resulted in a bias and 95% CI of 1.4° [-1.0°, 3.0°] (Figure 4B). The Bland-Altman RC derived from the inter-scan peak LV twist was 4.0°, indicating good reproducibility between the scans performed on different days. The inter-scan CCC was 0.6 for peak LV twist, which indicates moderate agreement.

Mean peak systolic twist rate and diastolic untwisting rate were 80.3±11.8°/s and 71.2±15.4°/s (Day-1, Scan-1 and Day 8) and -105.3±21.2°/s and -106.7±23.6°/s, respectively. Bland-Altman analysis resulted in an inter-scan bias and 95%-CI of 4.8°/s [-4.5°/s, 20.1°/s] and 2.0°/s [-25.2°/s, 18.1°/s] for systolic twist rate and diastolic untwisting rate, respectively.

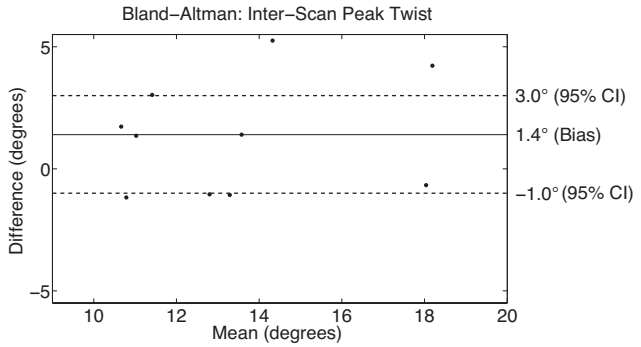
CL-shear angle Comparison

Mean peak CL-shear angles were 6.8±1.3° (Day-1, Scan-1), 6.8±1.3° (Day-1, Scan-2), and 6.4±1.2° (Day-8). Bland-Altman analysis resulted in intra- and inter-scan bias and 95%-CI of 0.0° [-0.7°, 0.9°] and 0.0° [-0.5°, 1.1°], respectively. Paired t-tests showed no significant differences in peak CL-shear angle for intra- and inter-scan values (p=0.91 and p=0.36 respectively). The Bland-Altman RCs for peak CL-shear angle were 1.6° and 1.6°

for intra- and inter-scan respectively, demonstrating good repeatability. The CCCs were 0.8 and 0.6 for peak CL-shear angle for intra- and inter-scan respectively, indicating good and moderate agreement respectively.



A.



B.

Figure 4. (A) Intra-scan Bland-Altman analysis of LV twist estimates indicates excellent agreement. The intra-scan comparison of LV twist measures has a bias of -0.6° and a 95% confidence interval of (-1.0°, 1.6°). (B) Inter-scan Bland-Altman analysis of LV twist estimates indicate good agreement. The inter-scan comparison of LV twist measures has a bias of -1.4° and a 95% confidence interval of (-1.0°, 3.0°).

DISCUSSION

This study demonstrates that peak LV twist is a reproducible quantitative measure of left ventricular function. The intra- and inter-scan RC values were under 4° suggesting the changes in an individuals twist greater than 4° would indicate significant change. If a 4° limit in the absolute difference of the measurements is used to calculate the specificity of LV twist, the specificity would be 80%. Since all volunteers were healthy subjects it is not possible to determine sensitivity.

However, several LV twist studies have reported changes in twist ranging from 3.5° to 7.6° with respect to different cardiovascular diseases. Cheung et al reported a mean peak twist decrease of 3.5° for subjects who underwent Teratology Of Fallot (TOF) repair relative to normal control subjects(73). Lindqvist et al demonstrated a mean peak twist decrease of 4.4° in patients with severe aortic stenosis post aortic valve repair(74). Kanzaki et al demonstrated a decrease in mean peak twist of 7.5° in patients with dilated cardiomyopathy relative to normal control subjects(31). Young et al showed an increase of 5.3° in mean peak twist in patients with hypertrophic cardiomyopathy compared with normal control subjects(32). Shudo et al reported a mean peak twist increase of 7.6° in patients with mitral regurgitation post mitral annuloplasty(75). In all, but one of these studies (TOF repair) FAST would be sensitive enough to detect the change in LV twist.

Peak CL-shear angle also proved to be a highly reproducible measure. The intra- and inter-scan RC values were equal suggesting scanning over multiple visits may be equivalently reproducible. Peak CL-shear angle may prove to be more reproducible over multiple visits than peak twist as the RC represents a smaller percentage of the mean peak CL-shear angle (24%) compared with the RC of peak twist (30%). The intra- and inter-scan RC values were 1.6° suggesting the changes in an individuals peak CL-shear angle greater than 1.6° would indicate significant change. If a 1.6° limit in the absolute difference of the measurements is used to calculate the specificity of peak CL-shear angle, the specificity would also be 80%.

Intra- and inter-scan reproducibility is an important factor for determining the ability of a technique to perform serial follow-up examinations, in particular, to detect changes in LV twist both in patients during the longitudinal assessment of disease progression and in a clinical trial seeking to evaluate new therapeutics. Our study has demonstrated good reproducibility of FAST derived measurements of LV twist and CL-shear angle. Better reproducibility may be achieved with optimized scanning protocols and may reduce subject sample size necessary to detecting significant changes in LV twist.

This study had several limitations: small normal subject sample size, apical and basal slice selection on different days and physiological differences arising from multiple breath-holds. This study was performed for a small subject sample size (n=10) of healthy subjects. Twist measurements are highly dependent on the choice of apical and basal slices(59). Measures such as torsion and CL-shear angle are often suggested to alleviate the dependence of twist on slice selection. Guaranteeing the same slice is selected on scans performed on the same volunteer on different days is challenging, as patient positioning, land marking, and localization each vary. In this study we sought to minimize the slice selection problem by having one MRI operator perform all the scans and by selecting slices with the same separation between scans. Nevertheless, it is hard to guarantee that exactly the same slice level is chosen for the apex and base each day.

Based on the anatomical landmarks that were systematically used for this study, it is possible that the apical and basal slices selected on Day-8 may have both been more apical or basal by up to ~3 mm (half the slice thickness) compared to Day-1. This influence may have contributed to differences seen in inter-scan peak twist, but twist is not expected to vary strongly as a function of apical-basal location hence this error is likely quite small. The decision to keep the distance between slices the same may contribute to less variability in peak CL-shear angle in this study. The fact that inter-exam RC is approximately 24% of the

mean peak CL-shear angle suggests that peak CL-shear angle has better reproducibility than peak twist (30%).

Physiological variability arising from multiple breath-holds likely contributes to the differences seen in intra-scan and inter-scan peak twist and would be expected in patient studies as well. It has been shown that increased preload increases peak twist and increased afterload can decreases peak twist(25). Inconsistent intra- and inter-exam breath-hold technique may lead to subtle changes in inter-thoracic pressure, which in turn can lead to changes in ventricular preload and afterload, thereby contributing to observed reproducibility of intra- and inter-scan peak twist. Furthermore, the need for repeated breath-holds can have a chronotropic and ionotropic effect which impacts ventricular function. The precise hemodynamic status of the subjects was not controlled for and was not known.

FAST is a semi-automated method that provides quick and quantitative assessment of LV systolic and diastolic twist that demonstrates both high intra- and inter-observer reproducibility(56) and now high intra-scan and moderate inter-scan reproducibility. The study has also demonstrated the CL-shear angle is similarly reproducible. FAST estimates of LV twist and CL-shear may serve as a useful quantitative imaging biomarker of LV dysfunction in longitudinal studies.

CHAPTER 7

Quantification of Left Ventricular Twist during Free-breathing with Spatial Modulation of Magnetization (SPAMM) and Fourier Analysis of STimulated Echoes (FAST)[5]

INTRODUCTION

Breath held MRI is challenging for patients with limited breath-holding capacity and breath holding cannot be used for patients requiring sedation. When breath held imaging is not feasible, free-breathing techniques, such as navigator gating (76), respiratory bellows gating (77), and multiple signal averages (78) are often used to minimize respiratory motion artifacts. Breath holding, however, can impart subtle shifts in hemodynamic loading of the heart, which consequently may impact quantitative measures of global and regional LV function. Free-breathing is a better estimate of normal, ambulatory physiology, whereas breath holding may cause subtle Valsalva(79) or Mueller(80) maneuvering, which will alter cardiac function.

Several free-breathing approaches have been used to evaluate regional cardiac function. Quantitative measures like radial, circumferential, and longitudinal strain derived from navigator-gated 3D DENSE have been shown to be in good agreement with breath-held strain values(76). Additionally, HARP strain maps derived from free-breathing and breath-held imaging also showed good agreement between the two breathing methods(81). The respiratory bellows gating device can be used to gate image acquisition with respect to the respiratory cycle(77) and has recently been re-evaluated for cardiac MRI studies. The bellows, however, has not been used in conjunction with the measurement of LV rotational mechanics before. However, in a recent study performed by Santelli et al, respiratory bellows gating was compared to navigator gating for coronary MRI and demonstrated a strong correlation in gating windows between the two free breathing techniques as well as a

[5] This work has been submitted for publication to the Journal of Cardiovascular Magnetic Resonance.

strong correlation between navigator and bellows for superior-inferior heart displacement (77).

Yet another approach for respiratory motion compensation is averaging with free-breathing, which produces images that are averaged over multiple cardiac and respiratory cycles and produces images with reduced motion artifacts, but noticeable blurring. Quantitative measures like blood flow derived from phase-contrast measurements have been shown to have good agreement between free-breathing with averaging and breath-held derived values(78). This is often an attractive option in pediatric MRI as it does not require any pulse sequence programming changes and is easily implemented.

Fourier Analysis of STimulated Echoes (FAST) is a novel MRI tagging method for the quantification of left ventricular (LV) twist(56). It has been shown to compare favorably to conventional estimates of LV twist from cardiac tagged images, but with significantly reduced user interaction time during post-processing(56). In this study, FAST derived measurements of LV twist from images acquired during free-breathing with averaging (AVG) and free-breathing with respiratory bellows (BEL) gating were compared with 'gold-standard' breath held (BH) values. We hypothesized that BH peak twist measures would not be significantly different from free-breathing derived images (AVG or BEL). Additionally, it was hypothesized that changes to peak circumferential longitudinal shear angle (CL-shear angle) would not be significantly different between BH and free-breathing (AVG or BEL) derived images.

METHODS

ORI-SPAMM

Off-resonance due to field inhomogeneity and chemical shift can lead to errors in quantitative measures such as LV strain measured by DENSE(49) and rotation or the velocity of flowing blood measured by phase contrast(62). Off-Resonance Insensitive

SPAMM (ORI-SPAMM) *(71)* was developed to eliminate the effects of off-resonance accrued during motion encoding. The original SPAMM(70) tagging preparation is used to generate a periodic tagging pattern that can be used to quantify rotation of the LV. Conventional SPAMM, however, results in a chemical shift induced tagging pattern shift of ~4 pixels at 3T. An additional off-resonant shift of ~1.1 pixel in the tagging pattern also arises during readout when using a bandwidth of ~400Hz/pixel, which produces a net shift of ~5.1 pixels.

The ORI-SPAMM preparation, modifies the original SPAMM tagging prep to include a 180° refocusing pulse and a split motion encoding gradient. This 180° pulse refocuses off-resonance accrued during the tagging preparation. Therefore, at 3T when the ORI modification is combined with a readout bandwidth of ~400 Hz/pixel, the total off-resonant shift of the tagging pattern is only ~1.1 pixels from readout.

Healthy Subjects MRI Protocol

The local institutional review board approved this study and all subjects provided written informed consent. Healthy human subjects (n=10) with no history of cardiovascular or respiratory disease were scanned twice (1 female, mean age of 29±4.3 years, weight 72.1±10.6 kg, height 1.8±0.1 m, and heart rate 56.1±8.9 beats/min). Volunteer demographics are summarized in Table 1. Data from this same cohort was used for an intra- and inter-exam reproducibility study.

Table 1. Healthy Volunteer Demographics

Age [yrs]	29±4.3
Weight [kg]	72.1±10.6
Height [m]	1.8±0.1
Gender [Male/Female]	9/1
Heart Rate [bpm]	56.1±8.9

ECG triggered images were acquired for head-first supine subjects during an end expiratory breath hold, on a Siemens Trio 3.0T scanner (Siemens Healthcare, Erlangen, Germany) and a six element body matrix coil in combination with a six element spine matrix. Axial, coronal, and sagittal orientation survey images were used for planning. Balanced steady-state free precession (bSSFP) cine images were collected using a 6 mm slice thickness and a 66% gap between slices, in parallel left ventricular (LV) short-axis planes and used to select basal and apical slices for collection of tagged images. The following criteria for selecting short axis slices from which twist measurements were derived was utilized: the most apical slice containing the presence of the blood pool throughout the entire cardiac cycle and the most basal slice in which the LV myocardium maintained a continuous annular shape during the entire cardiac cycle were selected.

A cardiac gated spoiled gradient echo sequence was modified to support 1-1 binomially weighted ORI-SPAMM line tags (with a total tagging flip angle of 134°). This sequence was used to acquire short-axis images at the base and apex of the LV with the following parameters: 280-330x280-330mm field-of-view, 6mm slice thickness, 192x192 acquisition matrix, 395 Hz/pixel receiver bandwidth, TE/TR =2.33-2.39/4.71-4.83 ms, 8 VPS, 12° imaging flip angle, 8 mm tag spacing, GRAPPA(82) based parallel imaging acceleration factor 2 with 24 central lines, and 14-27 cardiac phases. Cine tagged images were acquired using both horizontal and vertical tagging in separate breath holds. Scans were performed at 3.0T to ensure tag contrast through mid-diastole.

Tagged images from which LV twist was derived were acquired using the above protocol three times on each subject under different breath hold conditions. The first set of scans was acquired during an end expiratory breath hold (‘gold-standard’). The breath hold duration was 15 heart beats (12.5 ± 2.1 seconds) depending upon heart rate. The second set of scans was acquired during free breathing with four signal averages. The third set of

scans was acquired during free breathing and the respiratory bellows was used to for respiratory gating and set to acquire during the window of 30-35% expiration. The bellows consisted of a pressure-sensor that was affixed below the xiphoid process and secured with a Velcro belt. The scan order for horizontal and vertical tagging of the apex and base was randomized for each set of scans for each volunteer, to ensure scan ordering influences would not be introduced into the study.

Fourier Analysis of STimulated echoes (FAST)

FAST(56) is a semi-automated image processing method designed to quantify LV rotation from tagged MR images. The only user interaction necessary is contouring of the epicardium and endocardium in an end-systolic cardiac frame and in an early systolic cardiac frame, respectively. The main principle of the FAST method is that rotation in image space has a one to one correspondence with rotation in Fourier space, but in Fourier space the tagging information is focused into stimulated echoes, which are simpler to track. The user-defined contours are used to isolate the region of interest in the images (LV myocardium), then the images are Fourier transformed. The central peak in Fourier space is nulled and the image is subsequently cropped. Two-dimensional cross-correlation is used to determine rotation between cardiac frames, from which a cumulative rotation of the ventricle with respect to time is determined. This process is applied to images collected at both the apex and base of the heart, and the difference between the two rotations is defined as twist. The FAST method has been described in more detail and previously validated using both SPAMM and CSPAMM images in healthy volunteers(56). The FAST intra and inter-scan coefficient of repeatability (RC), a measure of the variability of the technique, was demonstrated using peak LV twist derived from breath-held line tagged images to be 4°. Peak twist was defined as the maximum difference in rotation between the apex and base.

The circumferential-longitudinal shear-angle (CL-shear angle) was defined as (64):

$$CL - Shear = \frac{\phi_{apex}\rho_{apex} - \phi_{base}\rho_{base}}{D},$$

where ϕ is rotation of the apex or base in degrees, ρ is the epicardial radius of the apex or base in mm, and D is the distance between the apex and base in mm. Estimates of apical and basal epicardial radii were made from averaging semi-major with the semi-minor axii of the ellipses derived from the FAST user-defined epicardial contours. Peak CL-shear angle has been suggested to be a better measure of LV function compared to twist, due to its normalization for heart size and selection of imaging planes(68).

Statistical Analysis

For each volunteer, peak twist derived from free-breathing with averaging (AVG), free-breathing with bellows gating (BEL) and breath-held (BH) were assessed according to the following method. First, a paired t-test with a Bonferroni post-hoc correction was used to test for the difference in peak twist between BH and AVG, AVG and BEL, and BH and BEL. A $p<0.0167$ after the post-hoc correction was considered statistically significant. Peak data values were reported as mean ± one standard deviation.

Next, linear regression with a forced zero intercept and Pearson's correlation coefficient (r) were used to determine agreement between BH and AVG, AVG and BEL, and BH and BEL for peak twist. Lastly, Bland-Altman analysis was used to compute the bias and 95% confidence intervals for peak twist. Bootstrapping with sampling and replacement was performed 1000 times on the median of the difference and used to determine the 95% confidence interval due to the limited sample size and non-Gaussian distribution. Bland-Altman bias is reported as the median of the difference in peak twist.

RESULTS

Image Quality

All of the data from all the volunteers during BH, AVG, and BEL were qualitatively acceptable and routinely analyzable by FAST without issue. Figure 1 depicts an example of BH (Fig. 1A), AVG (Fig. 1B), and BEL (Fig. 1C) images from a single normal subject. There is a noticeable loss of tissue-tag contrast in diastolic free-breathing images due to blurring which arises from uncompensated respiratory motion. As a result of the blurring effect, tag contrast is nearly lost late in the cardiac cycle, but is sufficient for systolic and early diastolic analysis. The loss of contrast in the bellows derived images later into the cardiac cycle is not as significant as that seen in averaging derived images. Figure 2 depicts the population mean LV twist during the cardiac cycle for BH, AVG, and BEL. Error bars are standard error of the mean for clarity. Figure 2 demonstrates, that despite the loss of contrast relatively good agreement exists between the BH, AVG, and BEL derived twist values. However, the twist curves start to deviate at end-systole and this deviation continues through diastole.

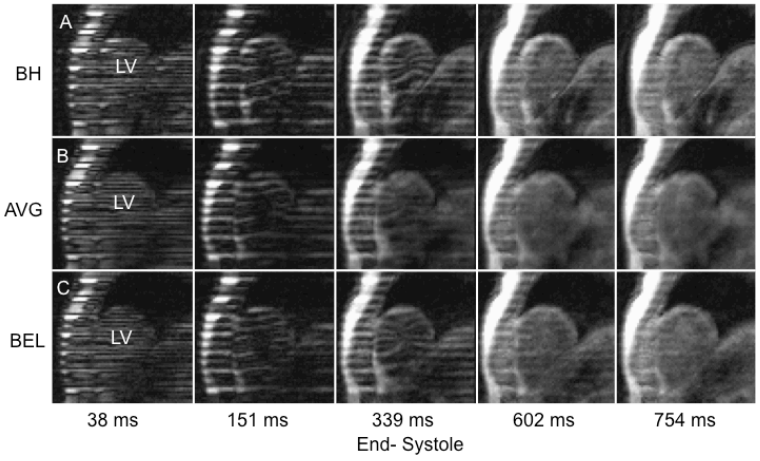


Figure 1. One set of short-axis line tagged images from a subject using (A) breath-held (BH), (B) free-breathing with averaging (AVG), and (C) free-breathing with bellows (BEL).

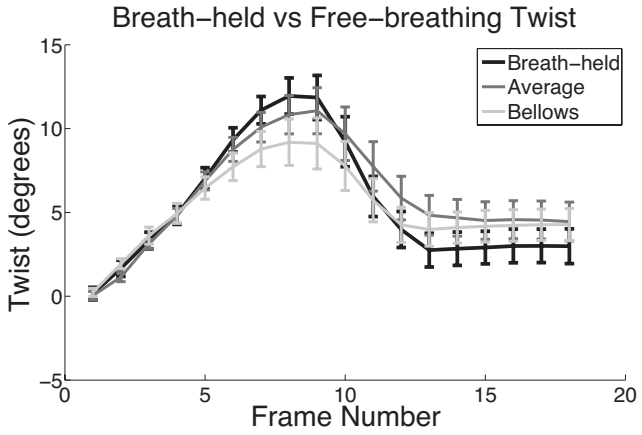


Figure 2 depicts the population mean LV twist during the cardiac cycle for BH, AVG, and BEL. Error bars are standard error of the mean for clarity. The breath-held (BH, black), free-breathing with averaging (AVG, dark gray) and bellows gated (BEL, light gray) demonstrates results similar to those shown in Table 2.

Table 2. Healthy Volunteer Rotational Mechanics Measurements

	BH	AVG	BEL
Mean Peak LV Twist [deg]	12.9±2.8	11.8±3.2	10.0±3.8*
Mean Peak CL-Shear Angle [deg]	6.5±1.3	6.1±1.0	5.2±1.3
Mean Peak Apical Rotation [deg]	9.0±3.1	8.2±3.1	7.3±4.0*
Mean Peak Basal Rotation [deg]	-4.3±1.7	-3.9±2.3	-3.2±1.7
LV Apical Epicardial Radius [mm]	23.6±2.3	24.9±3.2	25.8±3.6*
LV Basal Epicardial Radius [mm]	32.0±2.0	32.7±2.3	33.0±2.1*
Distance between Apex and Base [cm]		5.1±0.7	

LV Twist

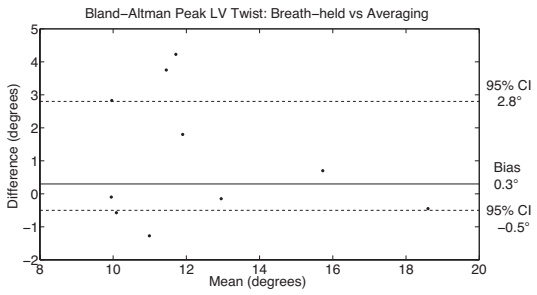
LV rotational and geometric measures used to estimate LV twist and CL-shear are summarized in Table 2. Mean peak twist measurements were 12.9±2.8° (BH), 11.8±3.2° (AVG), and 10.0±3.8° (BEL). Bland-Altman analysis of BH versus AVG, Figure 3A, resulted

in a bias with 95% CI of 0.3° [-0.5°, 2.8°] indicating a negligible bias between the two methods. Bland-Altman analysis of BH versus BEL, Figure 3B, resulted in a bias and of 2.2° and [1.0°, 4.3°] indicating moderate agreement between the two methods and worse agreement than was observed for BH compared to AVG. Bland-Altman analysis of AVG versus BEL, Figure 3C, resulted in a bias and 95% CI of 1.5° and [0.7°, 3.2°] indicating moderate agreement between the two methods and worse agreement than was observed for BH compared to AVG. Additionally, nearly all differences between BH and BEL or AVG peak twist were positive, indicating a positive biasing trend, that BH peak twist is greater than AVG and BEL gated values.

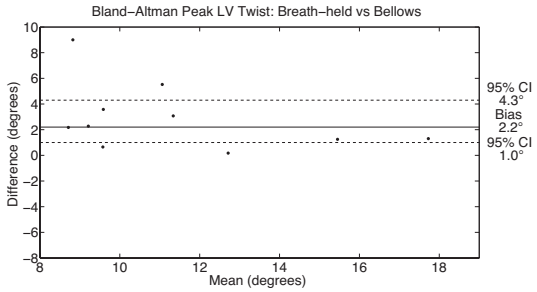
Paired t-tests with Bonferroni post-hoc correction showed significant differences for peak twist for BH vs. BEL ($p=0.007$) and AVG vs. BEL ($p=0.0153$), but no significant differences between BH to AVG ($p=0.1$). Linear regression analysis yielded BEL=0.8*BH with $r=0.7$, BEL=0.9*AVG with $r=0.8$, and AVG=0.9*BH with $r=0.8$. Scatter plots of the peak twist data and linear regression fit lines are presented in Figure 4.

The mean peak apical rotation was 9.0±3.1° (BH), 8.2±3.1° (AVG), and 7.3±4.0° (BEL). The mean peak basal rotation was -4.3±1.7 (BH), -3.9±2.3 (AVG), and -3.2±1.7 (BEL). The only significant difference observed in the apical and basal rotation data was between the BH and BEL apical rotation ($p=0.0153$); all other comparisons resulted in $p>0.16$.

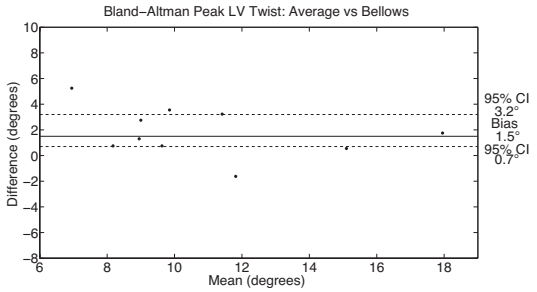
The mean apical epicardial radii measured in an end-systolic cardiac frame were: 23.6±2.3mm (BH), 24.9±3.2mm (AVG), 25.8±3.6mm (BEL). The basal epicardial radii were: 32.0±2.0mm (BH), 32.7±2.3mm (AVG), 33.0±2.1mm (BEL). The only significant differences observed in the radius data were between the BH and BEL apical epicardial radius ($p=0.012$) and the BH and BEL basal epicardial radius ($p=0.011$); all other comparisons resulted in $p>.05$.



A.

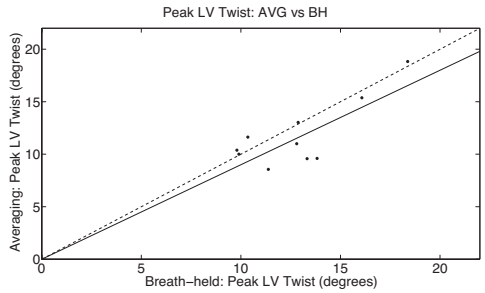


B.

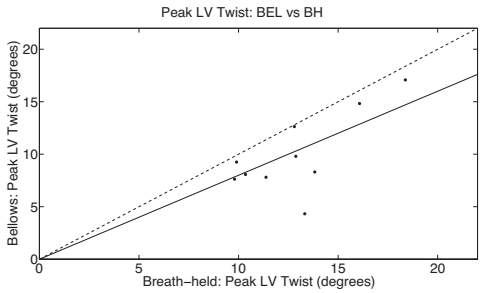


C.

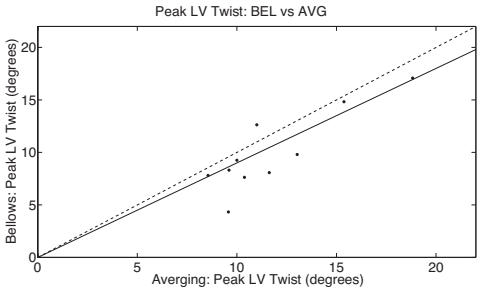
Figure 3. (A) Bland-Altman analysis of LV twist derived from breath held (BH) versus free-breathing with averaging (AVG) indicates excellent agreement, with a bias of 0.3° and a 95% confidence interval of [-0.5°, 2.8°]. (B) Bland-Altman analysis of LV twist derived from BH versus bellows-gating (BEL) indicates moderate agreement, with a bias of 2.2° and a 95% confidence interval of [1.0°, 4.3°]. (C) Bland-Altman analysis of LV twist derived from AVG versus BEL indicates moderate agreement, with a bias of 1.5° and a 95% confidence interval of [0.7°, 3.2°].



A.



B.



C.

Figure 4. (A) Linear regression analysis of LV twist derived from free-breathing with averaging (AVG) versus breath held (BH), where AVG=0.9*BH. (B) Linear regression analysis of LV twist derived from free-breathing with bellows-gating (BEL) versus breath held (BH), where BEL=0.8*BH. (C) Linear regression analysis of LV twist derived from free-breathing with bellows-gating (BEL) versus averaging (AVG), where BEL=0.9*AVG. Dashed lines represent the line of unity where as solid lines represent the linear regression fit equation.

CL-Shear Angle

Mean peak CL-shear angle measurements were 6.5±1.3° (BH), 6.1±1.0° (AVG), and 5.2±1.3° (BEL). Bland-Altman analysis of BH versus AVG resulted in a bias with 95% CI of

0.04° and [-0.3°, 1.5°]. Bland-Altman analysis of BH versus BEL resulted in a bias and 95% CI of 0.7° and [0.3°, 2.0°]. Bland-Altman analysis of AVG versus BEL resulted in a bias and 95% CI of 0.5° and [0.1°, 1.5°]. These results indicate good agreement between the two free breathing methods and breath-holding. Paired t-tests with Bonferroni post-hoc correction showed no significant differences for peak CL-shear angle for BH vs. BEL (p=0.02), AVG vs. BEL (p=0.03), and BH to AVG (p=0.19).

DISCUSSION

Breath-holding alters cardiovascular physiological conditions compared to free-breathing due to subtle changes in intrathoracic pressure. Cardiac MRI performed during free-breathing conditions will produce measurements that are less prone to measurement bias as a consequence of inadvertent, irreproducible, and subtle Valsalva(79) or Mueller(80) maneuvers. This study demonstrated that BEL estimates of peak twist were significantly smaller than BH estimates , however AVG peak twist estimates were only slightly lower than BH peak twist. This trend is evident in the mean peak twist values (Table 2).

BH peak twist was greater then BEL peak twist for every subject. This trend was not observed AVG (5 of 10 were greater). Zhong *et al*. also observed a decrease in the magnitude of strain when comparing navigator gated 3D cine DENSE data with breath-held 2D cine DENSE data(76) – a difference that likely arises from the different loading conditions. Note that linear regression of peak twist for BEL against BH produced the lowest slope.

The peak twist data derived from AVG fell in between the BH and BEL derived values. This may be due to averaging of the tagged images over different phases of the respiratory cycle. Averaged images collected during free-breathing represent a combination of all respiratory phases. This may also account for the significant peak twist differences observed between the two free-breathing methods, as bellows gating performs imaging only

during expiration. Additionally, changes in intrathoracic pressure due to free-breathing could lead to changes in LV volume and may account for some of the differences observed between breath-held and free-breathing twist measurements.

AVG was easily implemented and images did not display significant respiratory motion artifact, but were blurrier than BH. Furthermore, loss of contrast between the tags and tissue was evident during early diastole. Changes in LV diastolic physiology, heart rate variability, and through-plane or in-plane motion from average to average; and motion of the heart relative to the applied tagging planes likely accounts for the loss of contrast. There were no reconstruction errors associated with averaging and scan duration was known from the onset of the scan, making the averaging technique robust in clinical settings.

There were no significant differences in the peak CL-shear angle data. This indicates that CL-shear angle varies less than peak twist between free-breathing and breath-held MRI. The consistency of CL-shear angle data can be accounted for in the measured data used to compute CL-shear. There was a decrease in peak apical rotation observed between BH and BEL derived measurements. Additionally, there were significant differences noted between apical and basal epicardial radii under the breath-held and free-breathing conditions (Table 2). The decrease in rotation combined with the increase in end-systolic radii largely accounts for the lack of difference between the peak CL-shear angle measurements. Therefore, CL-shear angle may provide a better measure LV rotational mechanics as it depends less upon the LV size and may be better for inter-modality comparison, such as breath held MRI to free-breathing ultrasound. Nevertheless, there was a trend toward reduced CL-shear values with BEL compared to BH.

The radii measurements indicate that the end-systolic volume during free-breathing is greater than breath-held volume. This implies that afterload was increased, which is known to decrease peak twist(25). This implication is further corroborated by the significant decrease in peak apical rotation observed between BH and BEL gated derived values. The

altered loading conditions between breath-holding and free-breathing likely induce the differences seen in peak twist.

Limitations

Free-breathing with bellows gating, however, has significant limitations. First, image reconstruction is not always possible when using ECG gating and respiratory gating with the bellows. If the two gating windows do not align frequently, the scan time can become prohibitively long. Additionally, scan time can be prospectively estimated based on how frequently the ECG gating window and the bellows gating window align, however, the exact scan duration is unknown until the end of the acquisition, which may present a problem when the exam duration is constrained.

No patients were scanned in this study. Patients with limited breath-hold capacities may have non-uniform breathing patterns and may exert themselves more during breath holding. This may lead to poor inter-exam comparisons of breath held peak twist or CL-shear values. However, to produce diagnostic quality images with free-breathing, the subject's breathing pattern should be relatively consistent. Sporadic breathing patterns can lead to significant motion artifacts, which may lead to inaccuracies in peak twist and CL-shear measurements. Navigator gating is an increasingly popular respiratory motion compensation strategy, but it was not available for this study. Navigator gating may improve both the acquisition efficiency and image quality compared to BEL.

FAST is a semi-automated method that provides a quick and quantitative assessment of LV peak twist and CL-shear. Breath holding increases estimates of peak LV twist relative to bellows-gated free breathing, probably as a consequence of subtly altered hemodynamic loading conditions. Measurements of CL-shear angle derived from breath-held and free-breathing images did not significantly differ from each other, which may be explained by concomitant changes in LV volume. FAST estimates of LV twist under free-breathing

conditions may serve as a useful biomarker of LV dysfunction in patient populations with limited breath-hold capabilities.

CHAPTER 8

Left Ventricular Twist and Shear-Angle in Patients with Mitral Regurgitation[6]

INTRODUCTION

Primary mitral regurgitation (MR) is a common valvular disorder that foments left ventricular (LV) dysfunction. Primary MR is characterized by an incomplete closure of the mitral valve, which permits the flow of blood across the mitral valve during systole (decreased afterload) and leads to increased end-diastolic volume (increased preload). Additionally, chronic MR is known to deleteriously impact the rotational dynamics of the LV(29, 30, 38, 75, 83, 84). The twisting motion of the heart arises from transmural differences in the local myofiber orientation, which is thought minimize transmural stress gradients(85). Hence, alterations in the twisting mechanics may be indicative of incipient worsening disease. Several measures of rotational mechanics are suggested as imaging biomarkers for LV dysfunction(21, 68), including twist, torsion, twist-per-volume, and shear angle, but the latter two have not been evaluated in patients with MR with MRI.

LV twist is the preferred nomenclature for the measurement defined as the difference in the rotation of the apex relative to that of the base of the heart(68). A decrease in LV twist during the progression of MR has previously been evaluated with ultrasound(38, 75, 83, 84) in human subjects and implanted radiopaque markers in animal studies(29, 30), but CL-shear has not been reported. CL-shear is a measure of rotational mechanics that accounts for changes in LV ventricular diameter, which is known to increase with MR(86). CL-shear is also reported to be less sensitive to the precise selection of the short-axis imaging planes(68).

Ennis *et al*. studied chronic 'pure' MR in sheep using implanted radiopaque markers and demonstrated a significant decrease in both LV twist and in twist-per-volume slope(30).

[6] This work has been submitted for publication to Circulation: Cardiovascular Imaging.

Additionally, Tibayan *et al*. studied the evolution from acute to chronic MR in dogs using videofluroscopy and radiopaque markers and also observed a decrease in twist after three months of chronic MR(29). Borg *et al*. used speckle tracking echocardiography in patients with chronic primary MR to illustrate that the onset of LV untwist was delayed and untwisting rate was reduced in patients with MR. They did not observe significant differences in LV twist when compared to normal subjects and instead proposed the use of a twist-per-volume slope between peak twist and mitral valve opening, which showed a significant decrease in patients with MR(38). The expected decrease in peak twist paired with the increase in LV volume seen in patients with MR could make the twist-per-volume slope particularly insightful for evaluating the severity of dysfunction.

The clinical evaluation of LV rotational mechanics is a potentially valuable imaging biomarker of LV dysfunction, but most techniques require laborious post-processing, which significantly limits their clinical adoption. Fourier Analysis of STimulated Echoes (FAST) is a new MRI tissue tagging method that has recently been shown to compare favorably to conventional estimates of left ventricular (LV) twist from cardiac tagged images, but with significantly reduced user interaction time (2-3 minutes primarily for study selection)(56). FAST was applied to grid tag images acquired from patients with moderate and severe degenerative isolated MR to evaluate LV twist, CL-shear angle, and systolic twist-per-volume slope. We hypothesized that LV twist, CL-shear angle, and systolic twist-per-volume slope would decrease with increasing severity of MR.

METHODS

The local institutional review board approved this study and all subjects provided written informed consent. Moderate MR patients (n=29) and severe MR patients (n=54) with degenerative isolated MR were studied with MRI. Patients had moderate or severe MR

documented by color flow Doppler, LV EF of more than 55%, LV end-systolic dimension of 40 mm, and echocardiographic thickening of the mitral valve leaflets and prolapse.

Healthy normal subjects (n=54) with no history of cardiovascular disease were studied as age matched controls for the MR patients. MR severity was diagnosed qualitatively with echocardiogram/ Doppler studies and quantitatively with cine MRI. Subject demographics are summarized in Table 1. Note that height and gender information was missing for eight and five of the 29 moderate MR patients, respectively. Additionally, patients from the normal subject and severe MR subject groups have been presented in a previous study(86).

Breath-held ECG triggered images were acquired for all subjects on a 1.5T scanner (Signa, GE Healthcare, Milwaukee, WI). Prospectively triggered balanced steady-state free precession (bSSFP) cine images were collected in parallel left ventricular (LV) short-axis planes using the following typical parameters: 40x40 cm field of view, 256x128 matrix size, 8mm slice thickness, 45° flip angle, 1.6/3.8 ms echo/repetition times, 977 Hz/pixel receiver bandwidth, and 20 cardiac phases.

A prospectively triggered spoiled gradient echo sequence was used to acquire short-axis tagged images of the LV with the following typical parameters: 40x40cm field-of-view, 256x128 acquisition matrix, 8mm slice thickness, 10° imaging flip angle, 4.2/8.0ms echo/repetition times, 244Hz/pixel receiver bandwidth, 20.4 to 51.1 ms temporal resolution, and 20 cardiac phases. Grid tags were oriented 45° relative to the frequency encoding axis with 7 mm tag spacing.

The following criteria for selecting short axis slices from which twist measurements were derived was utilized: 1) the most apical slice containing the presence of the blood pool throughout the entire cardiac cycle; and 2) the most basal slice in which the LV myocardium maintained a continuous annular shape during the entire cardiac cycle were selected.

Fourier Analysis of STimulated echoes (FAST)

FAST(56) is a semi-automated image processing method that only requires 2-3 minutes of user interaction time (mostly for study selection) to quantify LV rotational mechanics. FAST determines rotation in Fourier space, where rotation in tagged MR images is easier to track. User defined contours of the epicardium in an end-systolic cardiac frame and endocardium in an early systolic cardiac frame were used to isolate the LV myocardium. The central (DC) frequency information in Fourier space was nulled and the Fourier image was cropped before cumulative rotation of the ventricle was determined with two-dimensional cross-correlation. This series of image processing steps was applied to both the apical and basal images of the heart, and the difference between the two rotations was defined as twist. The FAST method was previously validated using line tag images in healthy volunteers(56). Peak twist was defined as the maximum difference in rotation between the apex and the base. The circumferential-longitudinal shear-angle (CL-shear angle) was defined as (64, 68):

$$CL - Shear = \frac{\phi_{apex}\rho_{apex} - \phi_{base}\rho_{base}}{D} \qquad \text{[Equation 1]}$$

where ϕ is rotation of the apex or base in degrees, ρ is the epicardial radius of the apex or base in mm, and D is the distance between the apex and base in mm. Estimates of apical and basal epicardial radii were made from averaging the semi-major with the semi-minor axes of ellipses fit to the user-defined epicardial contours. CL-shear angle is considered to be a better measure of LV rotational mechanics compared to twist, due to its normalization for heart size and selection of imaging slices (68). Twist rate was defined as the discrete derivative of twist with respect to time with units of deg/s. Peak twist rate was defined as the maximum twist rate. Peak untwist rate was defined as the minimum twist rate. Peak normalized untwist rate was defined as the minimum twist rate divided by peak twist. The systolic twist-per-volume slope was defined as peak LV twist divided by the difference between LV end-systolic volume and end-diastolic volume. During ejection the volume of

the LV decreases, while twist increase, which leads to a negative systolic twist-per-volume slope(30).

Epicardial and endocardial contours were manually traced at end-systole and end-diastole from the bSSFP images. Papillary muscles were included in the LV volume. The contours were then propagated to the rest of the temporal frames with a dual propagation technique(87). LV volumes were computed by summing the areas defined by the endocardial contours in each short-axis slice multiplied by slice thickness(87). LV mass was computed by summing the areas between endocardial and epicardial contours multiplied by slice thickness and myocardium density (standard number here g/ml) (13).

Statistical Analysis

Summary statistics of the rotational mechanics measurements were reported by the grouping of MR by severity. ANOVA were used to test differences in peak twist, apical rotation, basal rotation, systolic twist rate, diastolic untwisting rate, systolic twist-per-volume slope, distance between apical and basal slices, and apical and basal epicardial radii between normal, moderate MR, and severe MR groups with adjusting for the covariates of age, weight, height, and gender. A similar analysis was also performed for peak CL-shear angle (due to missing information in subject height and gender during anonymization, additional an ANOVA test was performed without subject and gender as part of the sensitivity check). Additionally, a one-way ANOVA with three groups (normal, moderate MR, and severe MR) was used to assess differences in time to peak twist, peak normalized untwisting rate, endocardial radii, and the demographic values in Table 1. Multiple comparisons (Tukey's least significant difference (LSD) procedure) were applied to the measurement to determine which groups were significantly different from each other. A value of $P<0.05$ was considered statistically significant. All statistical analyses were performed with Matlab version 7.10.

RESULTS

Patient Demographics

Patient demographics are summarized in Table 1. Significant differences between the age, gender, height, end-systolic volume, end-diastolic volume, and LVED mass of the normal, moderate MR, and severe MR subjects were detected with a three group 1-way ANOVA. No significant differences were noted in weight and heart rate. Significant increases in end-systolic volume, end-diastolic volume, and LVED mass were observed and are expected with MR.

Table 1: Patient Demographics

	Normal	**Moderate MR***	**Severe MR**	**ANOVA P-Value**
Number of Subjects	54	29	54	-
Age [years]	44.9±14.4	50.2±12.2	54.4±11.7	P=0.01
Age Range [years]	20-70	21-69	25-79	-
Male/Female	23/31	3/21	38/16	P<0.001
Weight [kg]	74.9 ±18.4	74.2 ±16.6	81.3 ±14.9	P=0.08
Height [cm]	67.5±3.7	65.3±3.9	68.1±4.4	P=0.03
Heart Rate [bpm]	65.3±11.9	70.3±12.4	68.9±12.1	P=0.14
End-Systolic Volume [mL]	47.8±12.0	53.6±21.4	77.2± 24.0	P<0.001
End-Diastolic Volume [mL]	131.3±24.5	146.3±43.5	212.2±53.7	P<0.001
LVED Mass [g]	96.0±24.6	91.5±23.0	136.9±36.1	P<0.001

*** Height/Gender information is missing for 8/5 subjects**

Image Quality

All of the data from the normal, moderate MR, and severe MR subjects were qualitatively acceptable and routinely analyzable by FAST without issue. Figure 1 represents the typical

tagged image quality from normal, moderate MR, and severe MR subjects at the time of peak twist for the apex and base. The peak twist, apical rotation, and basal rotation corresponding to the images are also reported within the figure.

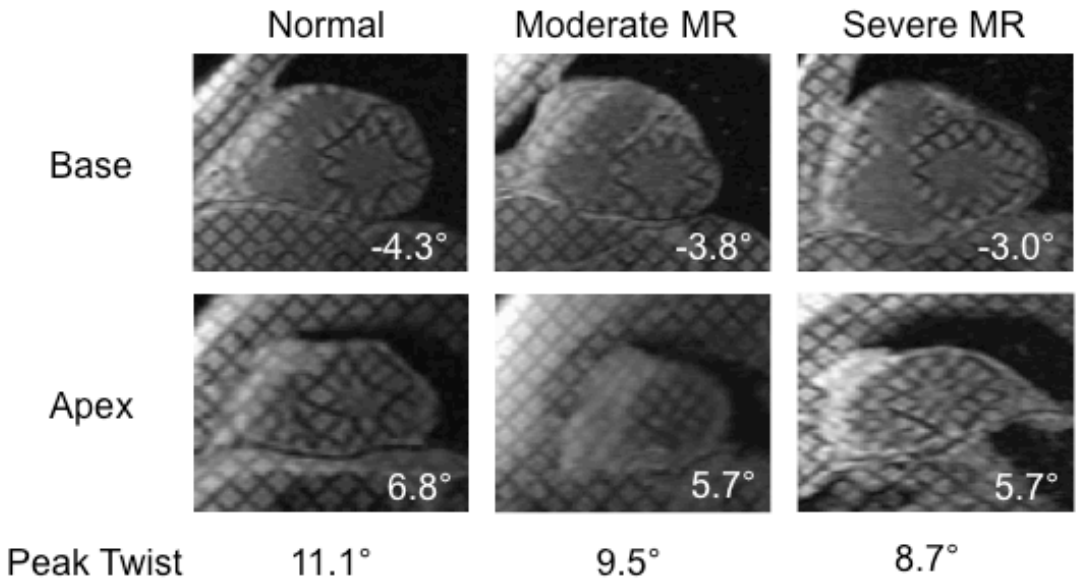


Figure 1. Representative tagged images from a normal subject and patients with moderate MR and severe MR. The basal and apical frames capture the time of peak LV twist. Individual LV rotation values are noted within the frame and peak LV twist values below the frame.

LV Rotation

LV apical and basal peak rotation measures are summarized in Table 2. Mean peak apical rotation for normal subjects, moderate MR patients, and severe MR patients were: 7.5±3.6°, 5.8±2.7°, and 6.2±2.8° respectively. The ANOVA of peak apical rotation between the groups showed differences among the groups (p=0.004) and with respect to the covariate of age (p=0.005). LSD for apical rotation showed a significant difference between

the normal subject group and the moderate MR patients and between the normal subject group and the severe MR patients.

Mean peak basal rotation values were: -3.9±1.3°, -3.4±1.4°, and -2.8±1.6°. The ANOVA of peak basal rotation between the groups showed differences among the groups (p=0.04) and with respect to age (p=0.004). LSD for basal rotation detected differences between the normal subject group and the severe MR patients and between the moderate MR patients and the severe MR patients.

LV Twist

LV apical and basal rotation, LV twist and twist rates, and LV twist-per-volume results are summarized in Table 2. Mean peak LV twist for normal subjects, moderate MR patients, and severe MR patients were: 11.5±3.2°, 9.0±3.0°, 8.8±2.6°, respectively (Table 2). The ANOVA of peak twist between the groups showed significant differences among the groups (p=0.0001). No significant differences were observed in peak LV twist due to patient demographics covariates (age, weight, height, gender). Further investigation with LSD showed significant decreases between the normal subject group and the moderate MR patients and between the normal subject group and the severe MR patients. Figure 2 demonstrates the changes in mean LV twist for normal, moderate MR, and severe MR subjects. Figure 3 is a scatter plot demonstrating the peak LV twist data from normal, moderate MR, and severe MR subjects.

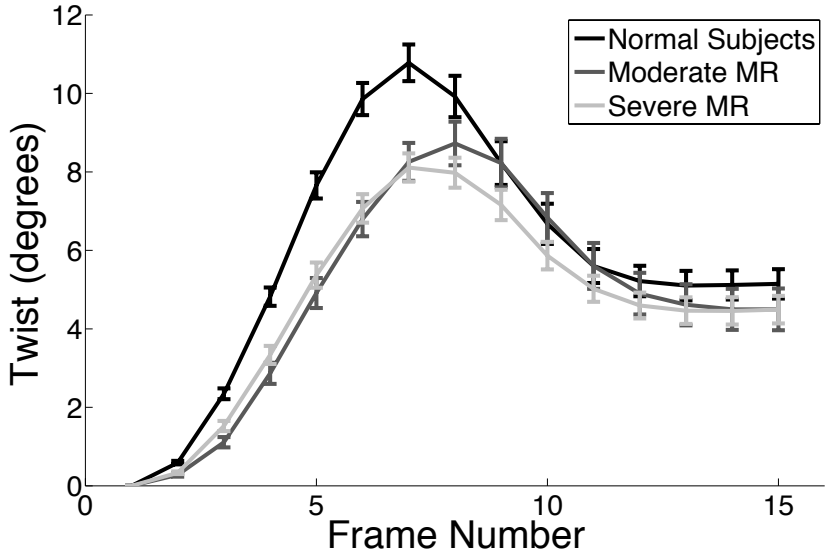


Figure 2. Population mean LV twist during the cardiac cycle for normal subjects and patients with moderate MR and severe MR. Error bars are standard error of the mean for clarity. Peak LV twist was larger in normal subjects compared to both patients with moderate and severe MR (p=0.0001).

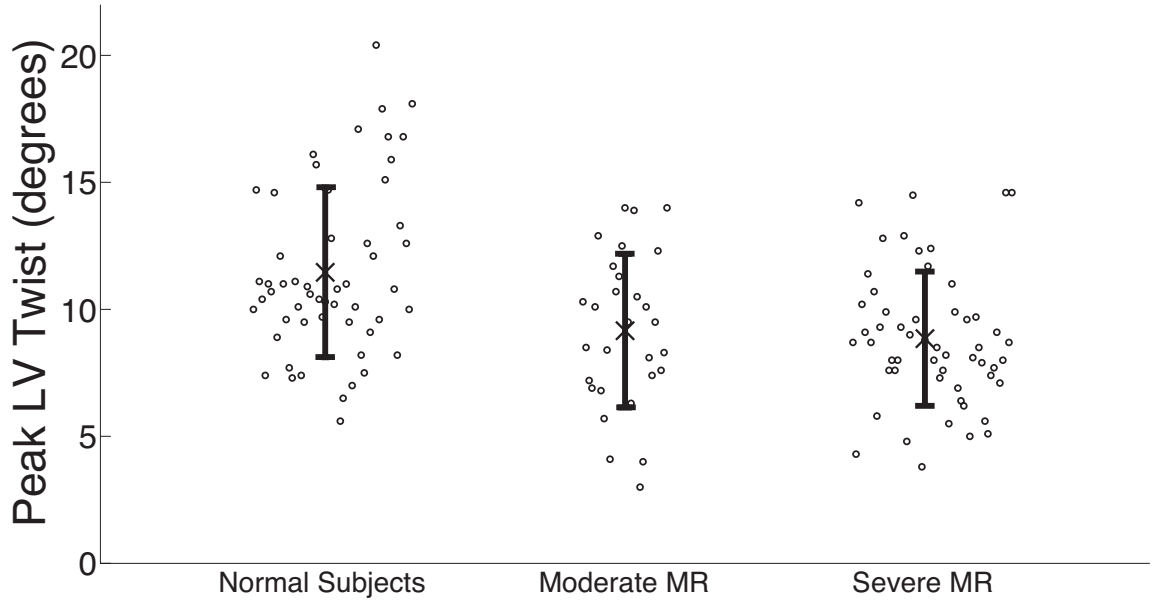


Figure 3. Peak LV twist values for normal subjects, moderate MR subjects, and severe MR subjects. The 'X' represents the mean peak LV twist and the error bars represent the standard deviation. LSD showed significant decreases between the normal subject group and the moderate MR patients and between the normal subject group and the severe MR patients.

Table 2: LV Twist Measurements

Measurement	Normal	Moderate MR	Severe MR	ANOVA P-Value
Peak Apical Rotation [deg]	7.5±3.6	5.8±2.7†	6.2±2.8†	P=0.004
Peak Basal Rotation [deg]	-3.9±1.3	-3.4±1.4	-2.8±1.6†‡	P=0.04
Peak Twist [deg]	11.5±3.3	9.2±3.0†	8.8±2.6†	P=0.0001
Peak Twist Rate [deg/s]	95.3±30.2	78.3±24.7†	71.6±23.0†	P<0.0001
Peak Untwisting Rate [deg/s]	-89.9±43.8	-62.6±32.9†	-63.0±32.0†	P=0.0007
Peak Norm Untwisting Rate [1/s]	-8.0±3.3	-7.1±3.6	-7.2 ±3.2	P=0.4
Time to Peak Twist [ms]	237.3±43.5	254.3±63.2	251.2±87.1	P=0.4
Systolic Twist-per-Volume Slope [deg/mL]	-0.14±0.05	-0.12±0.04†	-0.07±0.03†‡	P<0.0001

† LSD indicates significant difference from Normal

‡ LSD indicates significant difference from Moderate

Mean peak LV systolic twist rate for normal subjects, moderate MR patients, and severe MR patients were: 95.3±30.2°/s, 78.3±24.7°/s, and 71.6±23.0°/s, respectively. The ANOVA of peak twisting and untwisting rates between the groups showed differences among the groups ($p<0.0001$). No significant differences were observed in due to patient demographics covariates (age, weight, height, gender). Further investigation with LSD showed for peak

twisting rate showed significant decreases between the normal subject group and the moderate MR patients and between the normal subject group and the severe MR patients.

Mean diastolic untwisting rates were: -89.9±43.8°/s, -62.6±32.9°/s, and -63.0±32.0°/s, respectively. The ANOVA of peak twisting and untwisting rates between the groups showed differences among the groups (p=0.0007). No significant differences were observed due to patient demographics covariates (age, weight, height, gender). Further analysis with LSD for peak untwisting rate demonstrated significant decreases between the normal subject group and the moderate MR patients and between the normal subject group and the severe MR patients.

Mean peak normalized untwisting rates were: -8.0± 3.3s^{-1}, -7.1 ±3.6s^{-1}, -7.2 ±3.2s^{-1}. The one-way ANOVA of peak normalized untwisting rate showed no differences between the groups (p=0.4). Time to peak twist from normal subjects, moderate MR patients, and severe MR patients were: 237.3±43.5ms, 254.3±63.2ms, and 251.2±87.1ms, respectively. The one-way ANOVA did not reveal any significant differences (p=0.4).

Systolic twist-per-volume slope for normal subjects, moderate MR patients, and severe MR patients was: -0.14±0.05°/mL, -0.12±0.04°/mL, and -0.07±0.03°/mL respectively. The ANOVA of systolic twist-per-volume slope between the groups showed differences among the groups (p<0.0001) and with respect to weight (p=0.006). LSD detected significant decreases between normal subjects and moderate MR patients, normal subjects and severe MR patients, and moderate MR patients and severe MR patients. Figure 4 illustrates the twist-per-volume data for normal, moderate MR, and severe MR subjects.

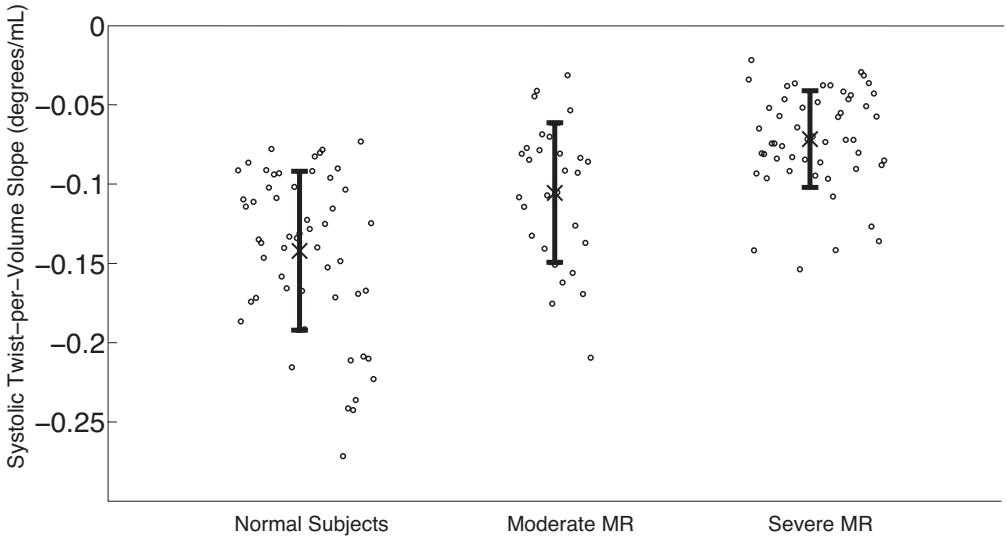


Figure 4. Systolic twist-per-volume slope derived from normal subjects, moderate MR subjects and severe MR subjects. The 'X' represents the mean systolic twist-per-volume slope and the error bars represent the standard deviation. LSD detected significant decreases in systolic twist-per-volume slope between normal subjects and moderate MR patients, normal subjects and severe MR patients, and moderate MR patients and severe MR patients.

CL-shear angle

CL-shear angle results and the measured parameters used to estimate CL-shear are summarized in Table 3 Mean peak CL-shear angle for normal subjects, moderate MR patients, and severe MR patients were: 5.0±1.4°, 4.7±1.6°, 5.0±1.3° respectively. Additionally, the ANOVA of peak CL-shear angle did not reveal any differences between the three groups (p=0.7). No significant differences were observed in peak CL-shear angle due to patient demographics covariates (age, weight, height, gender). Figure 5 demonstrates the differences in mean CL-shear angle for normal, moderate MR, and severe MR subjects.

Figure 6 illustrates the peak CL-shear data for normal, moderate MR, and severe MR subjects.

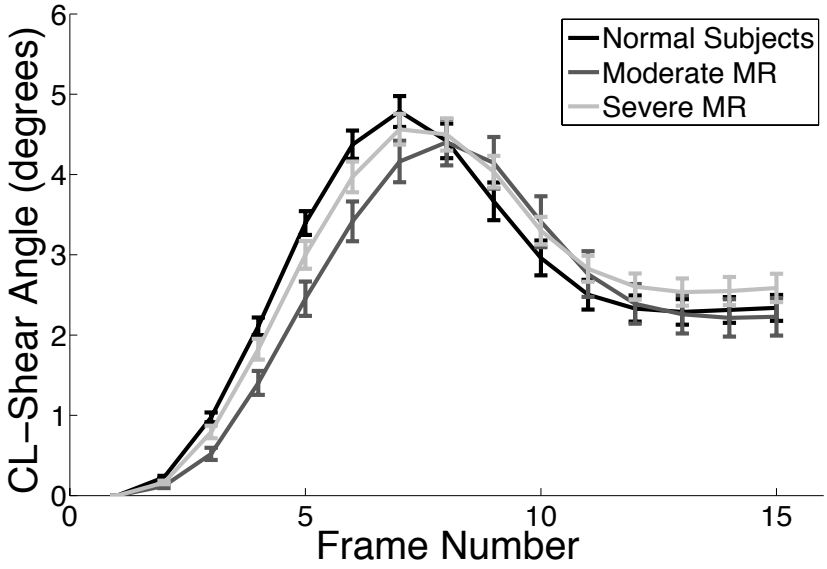


Figure 5. CL-shear angle for normal subjects and patients with moderate MR and severe MR during the cardiac cycle. Data curves represent the population mean. Standard error of the mean is used for the error bars for clarity. The magnitude of LV CL-shear angle appears to pseudo-normalize (P=0.7).

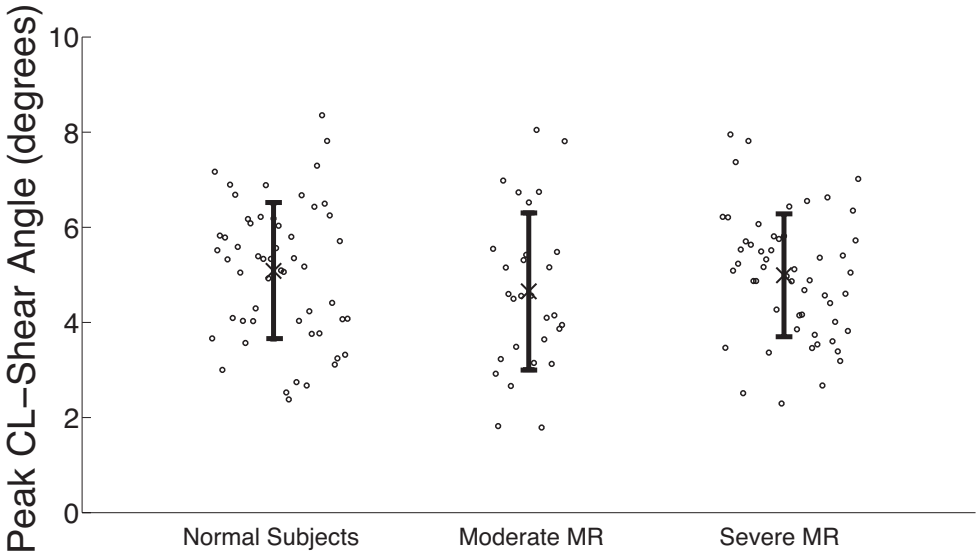


Figure 6. Peak LV CL-shear angle for normal subjects, moderate MR subjects, and severe MR subjects. The 'X' represents the mean peak CL-shear angle and the error bars represent the associated standard deviation of the mean. All pairwise comparisons of peak CL-shear angle for normal, moderate MR, and severe MR were considered not significant.

Table 3. CL-Shear Angle Measurements

Measurement	Normal	Moderate MR	Severe MR	ANOVA P-Value
Peak CL-shear angle [deg]	5.0±1.4	4.7±1.6	5.0±1.3	P=0.7
Epicardial radius Apex [mm]	20.7±3.1	19.9±3.3	24.9±3.8†‡	P<0.0001
Epicardial radius Base [mm]	30.7±3.8	30.7±2.6	35.8±3.2†‡	P<0.0001
Distance between Apex and Base [cm]	5.2±0.6	4.8±0.8	4.9±0.6	P=0.1

† LSD indicates significant difference from Normal

‡ LSD indicates significant difference from Moderate

Mean end-systolic apical epicardial radius for normal subjects, moderate MR patients, and severe MR patients were: 20.7±3.1mm, 19.9±3.3mm, and 24.9±3.8mm respectively. The ANOVA of apical radii between the groups showed differences among the groups ($p<0.0001$) and with respect to age ($p=0.01$). LSD showed significant increases between the normal subject group and the severe MR patients and between the moderate MR patients and the severe MR patients for the apical radii.

Mean end-systolic basal epicardial radius values were: 30.7±3.8mm, 30.7±2.6mm, and 35.8±3.2mm. The ANOVA of basal radii between the groups showed differences among the groups ($p<0.0001$) and with respect to weight ($p<0.004$). LSD showed significant increases

between the normal subject group and the severe MR patients and between the moderate MR patients and the severe MR patients for the basal radii.

Mean end-systolic apical endocardial radius for normal subjects, moderate MR patients, and severe MR patients were: 13.5±3.2mm, 16.3±3.4mm, and 19.5±3.6mm respectively. The one-way ANOVA of the apical radii between the groups showed significant differences among the groups ($p<0.0001$). LSD showed significant increases between all pairwise comparisons of the normal subject group, moderate MR patients and the severe MR patients for the apical radii.

Mean end-systolic basal endocardial radius values were: 23.0±3.7mm, 26.5±2.9mm, and 29.9±3.2mm. The one-way ANOVA of the basal radii between the groups showed significant differences among the groups ($p<0.0001$). LSD showed significant increases between all pairwise comparisons the normal subject group, moderate MR patients and the severe MR patients for the basal radii.

Distance between apical and basal slice levels used for rotational measurements from normal subjects, moderate MR patients, and severe MR patients were: 5.2±0.6cm, 4.8±0.8cm, and 4.9±0.6cm respectively. The ANOVA of distance between the groups showed differences among the groups ($p=0.1$) and with respect to height ($p=0.001$). However, LSD did not detected significant differences between any pair-wise comparison of normal subjects, moderate MR patients, and severe MR patients.

DISCUSSION

Decreased LV Twist

LV twist was shown to decrease significantly in patients with moderate or severe MR. In moderate MR patients this decrease was primarily due to a significant decrease in apical twist, while in patients with severe MR there was a significant reduction in both basal and apical rotations. This trend of reduction in LV twist in patients with MR is consistent with

previous reports(30, 75, 88). The decrease in apical rotation may be due to spherical remodeling of the mid-ventricular and apical LV(86). There were not, however, significant differences in peak LV twist between moderate and severe MR subjects, therefore peak LV twist may not correlate with the severity or progression of MR.

A previous study by Moustafa *et al*. used vector velocity echocardiography imaging to observe a decrease in epicardial twist in severe chronic primary MR patients, but an increase in endocardial twist in moderate MR patients compared with normal subjects(3). Their study demonstrated the gradient between epicardial and endocardial twist and the changes that occur as a function of the severity of MR and suggested that epicardial twist may not be sensitive enough to evaluate the varying degrees of MR.

Both moderate and severe MR were associated with significant decreases in the peak untwisting rate, which are consistent with previous literature(38). However, tag fading occurs around 500ms into the cardiac cycle, which makes measuring peak untwisting rate with the temporal resolution of this study challenging.

Pseudo-Normalization of CL-Shear Angle

Peak LV CL-shear angle appeared to pseudo-normalize in patients with MR. The formula for CL-shear angle depends on several factors (see Equation 1). The pseudo-normalization of CL-shear angle in moderate and severe MR can be explained by the significant increase in the apical and basal epicardial radii in conjunction with the significant decrease in apical rotation in MR patients compared with normal subjects. The severe MR patients also had a significant decrease in basal rotation, which further pseudo-normalizes CL-shear angle compared to moderate MR and normal subjects. Additionally, the pseudo-normalization did not occur just for peak CL-shear angle, but was apparent throughout the cardiac cycle (Figure 5).

CL-shear angle may not be a suitable imaging biomarker for the detection of LV dysfunction in patients with MR, since the measure pseudo-normalizes as a consequence of pathologically increased LV volumes. For patients with MR, the pseudo-normalization obscured the estimate of LV dysfunction and lead to no significant difference between the normal subjects and the MR patients.

Decreased Twist-Per-Volume

A significant decrease in the systolic twist-per-volume slope was detected for all pairwise comparisons of the subject groups (severe MR being the smallest), which is consistent with literature(30). Importantly, twist-per-volume was the only measure of rotational mechanics that distinguished all three groups. The changes indicate that LV stroke volume increases with respect to MR severity, while twist decreases. This may indicate an energetically unfavorable ejection pattern and lead to exacerbation of the underlying disease(85).

Limitations – Patients and healthy subjects showed some differences in demographics, hence we cannot rule out that this influenced the observed changes in LV rotational mechanics. All studies were performed at 1.5T, therefore diastolic rotational information was limited due to tag fading. Performing imaging at 3T or using a complementary tagging pattern(6) could improve diastolic estimates. In future studies, the temporal resolution should be improved, if accurate estimates of twist rates and rotational times are to be improved, but this can be difficult to achieve in patients with limited breath hold capacity. Better diastolic coverage and temporal resolution would improve insight into diastolic rotational mechanics. Additionally, the LV tapers considerable at the apex, implying small changes in slice location may have an impact on epicardial radius measurements.

The results of this study have shown that peak LV twist decreases similarly in patients with either moderate or severe MR compared with normal subjects. Notably, systolic twist-

per-volume slope was significantly decreased for moderate MR subjects and further decreased for severe MR subjects. Therefore, both peak LV twist and peak systolic twist-per-volume slope may serve as sensitive imaging biomarkers for LV dysfunction in patients with MR.

CHAPTER 9

Conclusion

Left ventricular twist is still in its infancy as an imaging biomarker of ventricular dysfunction. It has been studied in great detail for the past 20 years, but has not yet gained recognition in the clinic. In part this lack of recognition is due to the measurement's dependence on loading conditions and the need for well validated rapid quantification techniques for measurement. Left ventricular twist is still in its infancy as an imaging biomarker of left ventricular dysfunction. It has been studied in great detail for the past 20 years, but has not yet gained wide acceptance in the clinic. This lack of recognition is due, in part, to the need for well-validated rapid quantification techniques for measurement and the measurement's dependence on loading conditions. The development and validation of FAST herein may lead to increased acceptance in the clinic. Moving forward, the load-dependence of measures like CL-shear and twist-per-volume slope needs to be evaluated. These measures may be less load-dependent due to their normalization for ventricular size.

FAST+CSPAMM

We have evaluated Fourier Analysis of Stimulated echoes (FAST) and CSPAMM for the quantification of left ventricular (LV) systolic and diastolic function and compare it to the previously validated FAST+SPAMM technique. LV short-axis tagged images were acquired with CSPAMM and SPAMM in healthy volunteers (n=13). The FAST method was used to automatically estimate LV systolic and diastolic twist parameters from rotation of the stimulated echo and stimulated anti-echo about the middle of *k*-space subsequent to ~3 minutes of user interaction. There was no significant difference between measures obtained for FAST+CSPAMM and FAST+SPAMM for mean peak twist [13.5±2.7°vs.11.9±4.0°], torsion [3.4±0.8°/cm vs. 2.9±1.0°/cm], twisting rate [76.8±22.2°/s vs. 68.2±23.4°/s],

untwisting rate [-102.7±24.6°/s vs. -106.6±32.4°/s], normalized untwisting rate [-7.9±2.2/s vs. -9.9±4.4/s], and time of peak twist [279±23ms vs. 293±25ms] (all P>0.01). FAST+CSPAMM also provided measures of duration of untwisting (148±21ms) and the ratio of rapid untwist to peak twist (0.8±0.3). Bland-Altman analysis of FAST+CSPAMM and FAST+SPAMM twist data demonstrates excellent agreement with a bias of 1.1° and 95% confidence intervals of [-3.3°, 5.2°]. FAST+CSPAMM is a semi-automated method that provides a quick and quantitative assessment of LV systolic and diastolic twist and torsion that corresponds well to FAST+SPAMM measurements, but allows access to more diastolic rotational mechanics measures.

FAST+ORI-CSPAMM

We evaluated Off Resonance Insensitive Complementary SPAtial Modulation of magnetization (ORI-CSPAMM) and Fourier Analysis of STimulated echoes (FAST) for the quantification of left ventricular (LV) systolic and diastolic function and compare it to the previously validated FAST+SPAMM technique. ORI-CSPAMM corrects off-resonance accrued during tagging preparation and readout and visibly removes chemical shift from the tagging pattern, which confers greater robustness to the derived quantitative measures. LV short-axis tagged images were acquired with ORI-CSPAMM and SPAMM in healthy volunteers (n=13). There was no significant difference between measures obtained for FAST+ORI-CSPAMM and FAST+SPAMM for mean peak twist [12.9±3.4° vs.11.9±4.0°], torsion [3.3±0.9°/cm vs. 2.9±1.0°/cm], CL-shear angle [9.1±3.0° vs. 8.2±3.4°], twisting rate [79.6±20.2°/s vs. 68.2±23.4°/s], untwisting rate [-117.5±31.4°/s vs. -106.6±32.4°/s], normalized untwisting rate [-9.3±2.0/s vs. -9.9±4.4/s], and time of peak twist [281±18ms vs. 293±25ms] (all P≥0.1). FAST+ORI-CSPAMM also provided measures of duration of untwisting (148±21ms) and the ratio of rapid untwisting to peak twist (0.9±0.3). Bland-Altman analysis of FAST+ORI-CSPAMM and FAST+SPAMM twist data demonstrates excellent

agreement with a bias of -0.1° and 95% confidence intervals of [-1.0°, 3.2°]. FAST+ORI-CSPAMM provided well correlated results with respect to systolic twist and torsion compared to FAST+SPAMM, in addition to providing diastolic measures of twist and torsion.

FAST + Reproducibility

Assessing the reproducibility of new magnetic resonance imaging (MRI) biomarkers is an important part of validation. Fourier Analysis of STimulated Echoes (FAST) is a new MRI tissue tagging method that has recently been shown to compare favorably to conventional estimates of left ventricular (LV) twist from cardiac tagged images, but with significantly reduced user interaction time. The purpose of this study was to assess the intra- and inter-scan reproducibility of LV twist using FAST. Healthy volunteers (N=10) were scanned twice using FAST over one week. On Day-1 two measurements of LV twist were collected for intra-scan comparisons. Measurements for LV twist were again collected on Day-8 for inter-scan assessment. LV short-axis tagged images were acquired on a 3T scanner in order to ensure detectability of tags during early and mid-diastole. Reproducibility was assessed using the concordance correlation coefficient (CCC) and the repeatability coefficient (RC) (95%-CI range). Mean peak twist measurements were 13.4±4.3° (Day-1, Scan-1), 13.6±3.7° (Day-1, Scan-2), and 13.0±2.7° (Day-8). Bland-Altman analysis resulted in intra- and inter-scan bias and 95%-CI of -0.6° [-1.0°, 1.6°] and 1.4° [-1.0°, 3.0°], respectively. The Bland-Altman RC for peak LV twist was 2.6° and 4.0° for intra- and inter-scan respectively. The CCC was 0.9 and 0.6 for peak LV twist for intra- and inter-scan respectively. FAST is a semi-automated method that provides a quick and quantitative assessment of LV systolic and diastolic twist that demonstrates high intra-scan and moderate inter-scan reproducibility in preliminary studies.

FAST + Free-breathing

We investigated the effect of free-breathing on LV twist derived from tagged cardiovascular magnetic images. The purpose of this study was to determine if significant differences exist in left ventricular (LV) twist measurements derived using Fourier Analysis of STimulated echoes (FAST) applied to images acquired during breath-holding (BH), free-breathing with averaging (AVG), and respiratory bellows gated free-breathing (BEL).

LV twist measurements were acquired in healthy volunteers (N=10) during BH, AVG, and BEL conditions. LV short-axis tagged images were acquired on a 3T scanner in order to ensure the detection of tags from systole through mid-diastole. FAST was used to automatically estimate LV systolic and diastolic twist parameters subsequent to ~3 minutes of user interaction. Peak LV twist is reported as mean±SD. Breath-held images were considered the 'gold-standard'.

Mean peak twist measurements were 12.9±2.8° (BH), 11.8±3.2° (AVG), and 10.0±3.8° (BEL). Bland-Altman analysis of BH versus AVG resulted in a bias with 95% confidence intervals (CI) of 0.3° [-0.5°, 2.8°], 2.2° [1.0°, 4.3°] for BH versus BEL, and 1.5° [0.7°, 3.2°] for AVG versus BEL. A paired t-test with Bonferroni post-hoc correction showed a significant difference for peak LV twist for BH vs. BEL ($p=0.007$) and AVG vs. BEL ($p=0.0153$), but no significant differences in peak LV twist for BH to AVG ($p>0.1$). Linear regression analysis yielded AVG=0.9*BH ($r=0.8$), BEL=0.8*BH ($r=0.7$), and BEL=0.9*AVG ($r=0.8$).

FAST is a semi-automated method that provides a quick and quantitative assessment of LV systolic and diastolic twist and demonstrates good agreement between BH and AVG. BEL estimates of LV twist, however, are significantly lower than BH, which likely reflects the different hemodynamic loading conditions during the acquisitions. Because BH depth and consistency can be variable during clinical studies, BEL estimates may be a more consistent and accurate estimate of resting LV twist and may be a better biomarker of LV dysfunction in patient populations with limited breath-hold capabilities.

FAST + Mitral Regurgitation

Primary mitral regurgitation (MR) is a common valvular disorder that foments left ventricular (LV) dysfunction. LV twist is a quantitative imaging biomarker for LV dysfunction and is known to decrease in subjects with MR. LV systolic twist-per-volume slope has been proposed as a better measure of LV dysfunction because it accounts for changes in both rotational mechanics and ejection, but it has not been evaluated in patients with MR with MRI. It was hypothesized that LV twist and systolic twist-per-volume slope decrease with increasing severity of MR.

Normal subjects (n=54), moderate MR patients (n=29), and severe MR patients (n=54) were studied. MRI was performed on a 1.5T scanner and grid tagged LV images were collect at the base and apex. LV twist and systolic twist-per-volume slope measurements were derived from tagged images using Fourier Analysis of STimulated echoes (FAST). Compared to normal subjects (11.5°±3.2°) peak LV twist was decreased in both moderate (9.0°±3.0) and severe MR (8.8°±2.6°) ($p=0.001$). Peak systolic twist-per-volume slope was significantly different for all pairwise comparisons ($p<0.0001$) and was decreased in moderate MR (-0.12±0.04°/mL) and further decreased in severe MR (-0.07±0.03°/mL) compared to normal subjects (-0.14±0.05°/mL). Peak LV twist and peak systolic twist-per-volume slope significantly decrease with increasing severity of MR and may serve as sensitive imaging biomarkers for LV dysfunction in patients with MR.

Future Work

There are many changes that can be made to advance the FAST method. One change would be to decrease the computational processing time. The core of the FAST algorithm is 2D cross-correlation, a relatively expensive computer process. Currently, it takes about 20 minutes to process four sets of line tagged images that are 192x192 in size with a 2.4 GHz Intel Core 2 Duo processor. Replacing the full 2D cross-correlation algorithm with a

truncated version of cross-correlation may decrease the computational time of the algorithm. However, changes to the core 'matching' algorithm, 2D cross-correlation, would necessitate revalidation of the whole FAST technique.

Another area of advancement would be to automate a method to detect the limit of accurate rotational estimations. As myocardial tags fade in MR images, detection of rotation is impaired. Currently, a hard 500 ms cut off is used to determine when tag fading becomes significant enough to impair rotational estimates. A more detailed study of tissue-tag contrast and the rotational accuracy of FAST may be warranted. Additionally, implementing a method to automatically detect the type of tags used would further decrease user interaction. A peak detection algorithm in k-space that could identify tag orientation (horizontal versus vertical) or tag configuration (line, radial, or grid) could be used to accomplish this goal. An additional change to advance FAST would be to implement a method to segment the LV, perhaps with the use of radial tagging; these segments could then be used to perform regional rotational measurements. Currently, FAST can only produce global estimates of LV twist; unlike, HARP, FindTags, and DENSE, which can compute regional differences in twist and strain.

User-interaction is currently required to produce an accurate measure of LV twist. Manual epicardial and endocardial contouring is required to select the region of interest in the images. Full automation of FAST would be ideal for clinical applications and may be possible with the use of complimentary radial tagging, which requires the LV to be at the in the exact center of image. Importantly, the FAST method has been validated and applied to clinical patients. Future work, should involve the application of FAST to patient populations in which limited twist data exists such as pediatric patients with Duchenne and Becker Muscular Dystrophy or patients with congenital heart diseases.

Finally, the reproducibility study performed as part of this dissertation showed that FAST measurements of peak LV twist were reproducible within 2.6° and 4° determined from intra-

and inter-scan studies respectively. The low intra-scan and moderate inter-scan reproducibility using peak twist likely necessitate the need for a truly load independent measure of LV rotational mechanics. Systolic twist-per-volume slope takes into account the change in stroke volume and may therefore be less load dependent than peak LV twist. Further investigation into the reproducibility of systolic twist-per-volume slope is needed. More studies of the dependence of rotation on the slice position may help to determine how important slice positioning is to producing reproducible measurements of LV twist, torsion, and CL-shear. These measures may similarly benefit from normalization by ejected volume too. Studying changes in breath-holding conditions (expiration versus inspiration or long versus short breath-holding durations) may shed further light on the variability observed in the reproducibility study.

Ultimately, it may be shown that free-breathing estimates of rotational mechanics have the best intra- and inter-exam reproducibility. It may also be shown that improved temporal resolution can improve the reproducibility of FAST. The use of radial or grid tagging may further improve the reproducibility of FAST, due to the fewer number breath-holds needed to produce the measurement. The reproducibility study performed in this dissertation utilized peak twist values from 10 volunteers, however using power statistics to determine sample size, in order to properly assess the reproducibility of FAST at least 358 volunteers would be needed to have an 80% certainty in the results of the study (assuming mean values of 13.4° and 13.0° and a standard deviation of 2.7°). Thus, enrolling more volunteers (n>10) for the intra- and inter-scan reproducibility study would lend further statistical significance to the study.

CONCLUSION

Fourier Analysis of STimulated echoes is a rapid technique for quantifying left ventricular twist. FAST has been validated against the ‘gold-standard’ FindTags. The technique has

been refined and updated to produce accurate measures of twist to mid-diastole when used in conjunction with CSPAMM. FAST has been shown to provide reproducible measurements of twist during the same MR exam and between two different MR scans. Additionally, it has been utilized under free-breathing conditions to show changes in LV twist that occur as a result of breath-holding. Finally, it has been used to show a significant decrease in peak LV twist in patients with mitral regurgitation.

REFERENCES

1. Haacke EM, Brown R, Thompson M, Venkatesan R. Magnetic Resonance Imaging: Physical Principles and Sequence Design. New York: Wiley-Liss, 1999.
2. Liang ZP, Lauterbur PC. Principles of Magnetic Resonance Imaging: A Signal Processing Perspective. New York: IEEE Press, 2000.
3. Bernstein MA, King KE, Zhou XJ. Handbook of MRI Pulse Sequences. San Diego: Elsevier Academic Press, 2004.
4. Kwong RY. Cardiovascular Magnetic Resonance Imaging. Totowa: Humana Press, 2008.
5. Axel L, Dougherty L. MR imaging of motion with spatial modulation of magnetization. Radiology 1989; 171:841-845.
6. Fischer SE, McKinnon GC, Maier SE, Boesiger P. Improved myocardial tagging contrast. Magn Reson Med 1993; 30:191-200.
7. Stuber M, Spiegel MA, Fischer SE, et al. Single breath-hold slice-following CSPAMM myocardial tagging. MAGMA 1999; 9:85-91.
8. Sengupta PP, Korinek J, Belohlavek M, et al. Left ventricular structure and function: basic science for cardiac imaging. J Am Coll Cardiol 2006; 48:1988-2001.
9. Taber LA. Biomechanics of cardiovascular development. Annual Review of Biomedical Engineering 2001; 3:1-25.
10. Sedmera D, Pexieder T, Vuillemin M, Thompson RP, Anderson RH. Developmental patterning of the myocardium. Anatomical Record 2000; 258:319-337.
11. Anderson RH, Ho SY, Redmann K, Sanchez-Quintana D, Lunkenheimer PP. The anatomical arrangement of the myocardial cells making up the ventricular mass. European Journal of Cardio-Thoracic Surgery 2005; 28:517-525.

12. Vendelin M, Bovendeerd PHM, Engelbrecht J, Arts T. Optimizing ventricular fibers: uniform strain or stress, but not ATP consumption, leads to high efficiency. American Journal of Physiology-Heart and Circulatory Physiology 2002; 283:H1072-H1081.
13. Chen JJ, Liu W, Zhang HY, et al. Regional ventricular wall thickening reflects changes in cardiac fiber and sheet structure during contraction: quantification with diffusion tensor MRI. American Journal of Physiology-Heart and Circulatory Physiology 2005; 289:H1898-H1907.
14. Kung GL, Nguyen TC, Itoh A, et al. The presence of two local myocardial sheet populations confirmed by diffusion tensor MRI and histological validation. J Magn Reson Imaging; 34:1080-1091.
15. Durrer D, Vandam RT, Freud GE, Janse MJ, Meijler FL, Arzbaech.Rc. Total Excitation of Isolated Human Heart. Circulation 1970; 41:899-&.
16. Opthof T. In vivo dispersion in repolarization and arrhythmias in the human heart. American Journal of Physiology-Heart and Circulatory Physiology 2006; 290:H77-H78.
17. Sengupta PP, Khandheria BK, Korinek J, et al. Apex-to-base dispersion in regional timing of left ventricular shortening and lengthening. Journal of the American College of Cardiology 2006; 47:163-172.
18. Sengupta PP. Exploring Left Ventricular Isovolumic Shortening and Stretch Mechanics "The heart has its reasons ... ". Jacc-Cardiovascular Imaging 2009; 2:212-215.
19. Berne RM, Levy MN. Cardiovascular physiology. St. Louis: Mosby, 1997.
20. Bogaert J, Rademakers FE. Regional nonuniformity of normal adult human left ventricle. American Journal of Physiology-Heart and Circulatory Physiology 2001; 280:H610-H620.

21. Sengupta PP, Tajik AJ, Chandrasekaran K, Khandheria BK. Twist mechanics of the left ventricle: principles and application. JACC Cardiovasc Imaging 2008; 1:366-376.

22. Taber LA, Yang M, Podszus WW. Mechanics of ventricular torsion. J Biomech 1996; 29:745-752.

23. Ingels NB, Jr., Hansen DE, Daughters GT, 2nd, Stinson EB, Alderman EL, Miller DC. Relation between longitudinal, circumferential, and oblique shortening and torsional deformation in the left ventricle of the transplanted human heart. Circ Res 1989; 64:915-927.

24. Arts T, Veenstra PC, Reneman RS. Epicardial deformation and left ventricular wall mechanisms during ejection in the dog. Am J Physiol 1982; 243:H379-390.

25. Dong SJ, Hees PS, Huang WM, Buffer SA, Jr., Weiss JL, Shapiro EP. Independent effects of preload, afterload, and contractility on left ventricular torsion. Am J Physiol 1999; 277:H1053-1060.

26. Notomi Y, Srinath G, Shiota T, et al. Maturational and adaptive modulation of left ventricular torsional biomechanics: Doppler tissue imaging observation from infancy to adulthood. Circulation 2006; 113:2534-2541.

27. Nagel E, Stuber M, Burkhard B, et al. Cardiac rotation and relaxation in patients with aortic valve stenosis. Eur Heart J 2000; 21:582-589.

28. Stuber M, Scheidegger MB, Fischer SE, et al. Alterations in the local myocardial motion pattern in patients suffering from pressure overload due to aortic stenosis. Circulation 1999; 100:361-368.

29. Tibayan FA, Yun KL, Fann JI, et al. Torsion dynamics in the evolution from acute to chronic mitral regurgitation. J Heart Valve Dis 2002; 11:39-46; discussion 46.

30. Ennis DB, Nguyen TC, Itoh A, et al. Reduced systolic torsion in chronic "pure" mitral regurgitation. Circ Cardiovasc Imaging 2009; 2:85-92.

31. Kanzaki H, Nakatani S, Yamada N, Urayama S, Miyatake K, Kitakaze M. Impaired systolic torsion in dilated cardiomyopathy: reversal of apical rotation at mid-systole characterized with magnetic resonance tagging method. Basic Res Cardiol 2006; 101:465-470.

32. Young AA, Kramer CM, Ferrari VA, Axel L, Reichek N. Three-dimensional left ventricular deformation in hypertrophic cardiomyopathy. Circulation 1994; 90:854-867.

33. Ennis DB, Epstein FH, Kellman P, Fananapazir L, McVeigh ER, Arai AE. Assessment of regional systolic and diastolic dysfunction in familial hypertrophic cardiomyopathy using MR tagging. Magn Reson Med 2003; 50:638-642.

34. Guttman MA, Zerhouni EA, McVeigh ER. Analysis of Cardiac Function from MR Images. IEEE Comput Graph Appl 1997; 17:30-38.

35. Osman N, Kerwin W, McVeigh E, Prince J. Cardiac motion tracking using CINE harmonic phase (HARP) magnetic resonance imaging. Magn Reson Med 1999; 42:1048-1060.

36. Bansal M, Leano RL, Marwick TH. Clinical assessment of left ventricular systolic torsion: effects of myocardial infarction and ischemia. J Am Soc Echocardiogr 2008; 21:887-894.

37. Meluzin J, Spinarova L, Hude P, et al. Left ventricular mechanics in idiopathic dilated cardiomyopathy: systolic-diastolic coupling and torsion. J Am Soc Echocardiogr 2009; 22:486-493.

38. Borg AN, Harrison JL, Argyle RA, Ray SG. Left ventricular torsion in primary chronic mitral regurgitation. Heart 2008; 94:597-603.

39. Burns AT, La Gerche A, Prior DL, Macisaac AI. Left ventricular untwisting is an important determinant of early diastolic function. JACC Cardiovasc Imaging 2009; 2:709-716.

40. van Dalen BM, Soliman OI, Vletter WB, ten Cate FJ, Geleijnse ML. Age-related changes in the biomechanics of left ventricular twist measured by speckle tracking echocardiography. Am J Physiol Heart Circ Physiol 2008; 295:H1705-1711.

41. Doyle M, Walsh EG, Blackwell GG, Pohost GM. Block regional interpolation scheme for k-space (BRISK): a rapid cardiac imaging technique. Magn Reson Med 1995; 33:163-170.

42. Guttman MA, Zerhouni EA, McVeigh ER. Analysis and Visualization of Cardiac Function from MR Images. IEEE Comp. Graph. Appl. 1997; 17:30-38.

43. Osman NF, Kerwin WS, McVeigh ER, Prince JL. Cardiac motion tracking using CINE harmonic phase (HARP) magnetic resonance imaging. Magnetic Resonance in Medicine 1999; 42:1048-1060.

44. Bland JM, Altman DG. Statistical methods for assessing agreement between two methods of clinical measurement. Lancet 1986; 1:307-310.

45. Thompson RB, Paterson I, Chow K, et al. Characterization of the relationship between systolic shear strain and early diastolic shear strain rates: insights into torsional recoil. American Journal of Physiology-Heart and Circulatory Physiology 2010; 299:H898-H907.

46. Henson RE, Song SK, Pastorek JS, Ackerman JJH, Lorenz CH. Left ventricular torsion is equal in mice and humans. American Journal of Physiology-Heart and Circulatory Physiology 2000; 278:H1117-H1123.

47. Derbyshire JA, Sampath S, McVeigh ER. Phase-sensitive cardiac tagging--REALTAG. Magn Reson Med 2007; 58:206-210.

48. Herzka DA, Guttman MA, McVeigh ER. Myocardial tagging with SSFP. Magn Reson Med 2003; 49:329-340.

49. Aletras AH, Ding S, Balaban RS, Wen H. DENSE: displacement encoding with stimulated echoes in cardiac functional MRI. J Magn Reson 1999; 137:247-252.

50. Popescu BA, Calin A, Beladan CC, et al. Left ventricular torsional dynamics in aortic stenosis: relationship between left ventricular untwisting and filling pressures. A two-dimensional speckle tracking study. Eur J Echocardiogr 2010; 11:406-413.

51. van Dalen BM, Soliman OI, Kauer F, et al. Alterations in left ventricular untwisting with ageing. Circ J 2009; 74:101-108.

52. Brutsaert DL, Sys SU, Gillebert TC. Diastolic failure: pathophysiology and therapeutic implications. J Am Coll Cardiol 1993; 22:318-325.

53. Matter C, Nagel E, Stuber M, Boesiger P, Hess OM. Assessment of systolic and diastolic LV function by MR myocardial tagging. Basic Res Cardiol 1996; 91 Suppl 2:23-28.

54. Zile MR, Gaasch WH, Carroll JD, et al. Heart failure with a normal ejection fraction: is measurement of diastolic function necessary to make the diagnosis of diastolic heart failure? Circulation 2001; 104:779-782.

55. Yun KL, Niczyporuk MA, Daughters GT, 2nd, et al. Alterations in left ventricular diastolic twist mechanics during acute human cardiac allograft rejection. Circulation 1991; 83:962-973.

56. Reyhan M, Natsuaki Y, Ennis DB. Fourier analysis of STimulated echoes (FAST) for the quantitative analysis of left ventricular twist. J Magn Reson Imaging 2012; 35:587-593.

57. Henson RE, Song SK, Pastorek JS, Ackerman JJ, Lorenz CH. Left ventricular torsion is equal in mice and humans. Am J Physiol Heart Circ Physiol 2000; 278:H1117-1123.

58. Notomi Y, Martin-Miklovic MG, Oryszak SJ, et al. Enhanced ventricular untwisting during exercise: a mechanistic manifestation of elastic recoil described by Doppler tissue imaging. Circulation 2006; 113:2524-2533.

59. Thompson RB, Paterson I, Chow K, et al. Characterization of the relationship between systolic shear strain and early diastolic shear strain rates: insights into torsional recoil. Am J Physiol Heart Circ Physiol 2010; 299:H898-907.

60. Weiner RB, Hutter AM, Jr., Wang F, et al. The impact of endurance exercise training on left ventricular torsion. JACC Cardiovasc Imaging 2010; 3:1001-1009.

61. Stohr EJ, Gonzalez-Alonso J, Shave R. Left ventricular mechanical limitations to stroke volume in healthy humans during incremental exercise. Am J Physiol Heart Circ Physiol 2011; 301:H478-487.

62. Middione MJ, Ennis DB. Chemical shift-induced phase errors in phase-contrast MRI. Magn Reson Med 2012; doi: 10.1002/mrm.24262, [Epub ahead of print].

63. Fahmy AS, Basha TA, Osman NF. Inherent fat cancellation in complementary spatial modulation of magnetization. Magn Reson Med 2009; 61:234-238.

64. Russel IK, Tecelao SR, Kuijer JP, Heethaar RM, Marcus JT. Comparison of 2D and 3D calculation of left ventricular torsion as circumferential-longitudinal shear angle using cardiovascular magnetic resonance tagging. J Cardiovasc Magn Reson 2009; 11:8.

65. Kies P, Bootsma M, Bax J, Schalij MJ, van der Wall EE. Arrhythmogenic right ventricular dysplasia/cardiomyopathy: screening, diagnosis, and treatment. Heart Rhythm 2006; 3:225-234.

66. Nishimura T, Yanagisawa A, Sakata H, et al. Thallium-201 single photon emission computed tomography (SPECT) in patients with duchenne's progressive muscular dystrophy: a histopathologic correlation study. Jpn Circ J 2001; 65:99-105.

67. Russel IK, Brouwer WP, Germans T, et al. Increased left ventricular torsion in hypertrophic cardiomyopathy mutation carriers with normal wall thickness. J Cardiovasc Magn Reson; 13:3.

68. Young AA, Cowan BR. Evaluation of left ventricular torsion by cardiovascular magnetic resonance. J Cardiovasc Magn Reson 2012; 14:49.

69. Takeuchi M, Nishikage T, Nakai H, Kokumai M, Otani S, Lang RM. The assessment of left ventricular twist in anterior wall myocardial infarction using two-dimensional speckle tracking imaging. J Am Soc Echocardiogr 2007; 20:36-44.

70. Axel L, Dougherty L. Mr Imaging of Motion with Spatial Modulation of Magnetization. Radiology 1989; 171:841-845.

71. Reyhan M, Ennis DB. Quantification of Left Ventricular Torsion by Off-Resonance Insensitive CSPAMM (ORI-CSPAMM). Proceedings of the International Society of Magnetic Resonance in Medicine 2011; 19:3373.

72. Reyhan M, Ennis DB. Quantitative assessment of systolic and diastolic left ventricular twist using Fourier Analysis of STimulated echoes (FAST) and CSPAMM. J Cardiovasc Magn Reson 2012; 4(Suppl 1):P240.

73. Cheung YF, Wong SJ, Liang XC, Cheung EW. Torsional mechanics of the left ventricle in patients after surgical repair of tetralogy of Fallot. Circ J 2011; 75:1735-1741.

74. Lindqvist P, Zhao Y, Bajraktari G, Holmgren A, Henein MY. Aortic valve replacement normalizes left ventricular twist function. Interact Cardiovasc Thorac Surg 2011; 12:701-706.

75. Shudo Y, Nakatani S, Sakaguchi T, et al. Left ventricular mechanics following restrictive mitral annuloplasty for functional mitral regurgitation: two-dimensional speckle tracking echocardiographic study. Echocardiography 2012; 29:445-450.

76. Zhong X, Spottiswoode BS, Meyer CH, Kramer CM, Epstein FH. Imaging three-dimensional myocardial mechanics using navigator-gated volumetric spiral cine DENSE MRI. Magn Reson Med 2010; 64:1089-1097.

77. Santelli C, Nezafat R, Goddu B, et al. Respiratory bellows revisited for motion compensation: preliminary experience for cardiovascular MR. Magn Reson Med 2011; 65:1097-1102.

78. Jin N, Lewandowski RJ, Omary RA, Larson AC. Respiratory self-gating for free-breathing abdominal phase-contrast blood flow measurements. J Magn Reson Imaging 2009; 29:860-868.

79. Gorlin R, Knowles JH, Storey CF. The Valsalva maneuver as a test of cardiac function; pathologic physiology and clinical significance. Am J Med 1957; 22:197-212.

80. Condos WR, Jr., Latham RD, Hoadley SD, Pasipoularides A. Hemodynamics of the Mueller maneuver in man: right and left heart micromanometry and Doppler echocardiography. Circulation 1987; 76:1020-1028.

81. Sampath S, Derbyshire JA, Atalar E, Osman NF, Prince JL. Real-time imaging of two-dimensional cardiac strain using a harmonic phase magnetic resonance imaging (HARP-MRI) pulse sequence. Magn Reson Med 2003; 50:154-163.

82. Griswold MA, Jakob PM, Heidemann RM, et al. Generalized autocalibrating partially parallel acquisitions (GRAPPA). Magn Reson Med 2002; 47:1202-1210.

83. Moustafa SE, Kansal M, Alharthi M, Deng Y, Chandrasekaran K, Mookadam F. Prediction of incipient left ventricular dysfunction in patients with chronic primary mitral regurgitation: a velocity vector imaging study. Eur J Echocardiogr; 12:291-298.

84. Kazui T, Niinuma H, Tsuboi J, Okabayashi H. Changes in left ventricular twist after mitral valve repair. J Thorac Cardiovasc Surg; 141:716-724.

85. Bovendeerd PH, Arts T, Huyghe JM, van Campen DH, Reneman RS. Dependence of local left ventricular wall mechanics on myocardial fiber orientation: a model study. J Biomech 1992; 25:1129-1140.

86. Schiros CG, Dell'Italia LJ, Gladden JD, et al. Magnetic resonance imaging with 3-dimensional analysis of left ventricular remodeling in isolated mitral regurgitation: implications beyond dimensions. Circulation; 125:2334-2342.

87. Feng W, Nagaraj H, Gupta H, et al. A dual propagation contours technique for semi-automated assessment of systolic and diastolic cardiac function by CMR. J Cardiovasc Magn Reson 2009; 11:30.

88. Tibayan FA, Rodriguez F, Langer F, et al. Alterations in left ventricular torsion and diastolic recoil after myocardial infarction with and without chronic ischemic mitral regurgitation. Circulation 2004; 110:II109-114.